Spoof Surface Plasmon Polariton Based THz Circuitry

by

Mahdi Aghadjani

A dissertation submitted in partial fulfillment
of the requirements for the degree of
Doctor of Philosophy
(Electrical Engineering)
in The University of Michigan
2018

Doctoral Committee:

Professor Pinaki Mazumder, Chair
Professor Steven Cundiff
Associate Professor Somin E. Lee
Professor Herbert G. Winful

Mahdi Aghadjani

Mahdia@umich.edu

ORCID iD: 0000-0002-0602-6311

To my family for supporting me throughout these years of scientific research and

endeavor

ACKNOWLEDGEMENTS

I would like to express the deepest appreciation to my academic advisor and committee chair Professor Pinaki Mazumder, who has the attitude and the substance of a genius: he continually and convincingly conveyed a spirit of adventure in regard to research and scholarship and an excitement in regard to teaching. Without his guidance and persistent help, this dissertation would not have been possible.

I would like to equally thank the rest of my committee members, Professor Somin E. lee, Professor Herbert Winful, and Professor Steven Cundiff for their insightful comments and encouragement to widen my research from various perspectives.

I would also like to express my sincere gratitude to my colleague Zhao Xu, who has pioneered the exploration of plasmonic architectures. His excellent works has led me into this outstanding field of research and has offered great insight that leads to my success. I thank my fellow lab-mates for all the stimulating discussions, for the long days and sleepless nights we were working together, and for all the fun we have had in the past years.

TABLE OF CONTENTS

LIST OF FIGURES

Abstract

Terahertz, abbreviated as THz, (also called T-ray similar to X-ray and γ -ray) is defined as the frequency band spanning from 300 GHz to 10 THz, which is located between the microwave from the electronic side of the electromagnetic (EM) spectrum to mid-Infra-Red (abbreviated as mid-IR) on the photonic side of the EM spectrum. As accelerated research and innovations over the past seven decades have resulted in widespread commercialization of both electronic and photonic components, THz band has remained underdeveloped, underexploited, and mostly unallocated by the Federal Communications Commission (FCC). Though certain definitive merits of EM waves at THz have evoked interests of physicists, chemists, biologists and material scientists to deploy THz in Time-Domain Spectroscopy (TDS), bio-sensing, and classical imaging applications, the field of THz circuits (also known as THz electronics) has continued to remain in embryonic stage due to the speed (f_T <1 THz) limitations of conventional Silicon and compound semiconductor devices like Field Effect Transistors (FETs), Hetero-junction Bipolar Transistors (HBTs), and Hot Electron Mobility Transistors (HEMTs). On the other hand, conventional photonic devices cannot be readily adopted to design new THz circuits and systems. Our research vision in THz circuits and systems is to study the meta-material properties of THz

in various forms of sub-wavelength structures and exploit those unique properties to invent the designs of large THz systems like the THz switch, Analog-to-Digital Converter (ADC), etc. without requiring the use of conventional electronic transistors or photonic components. This transformative approach envisions leveraging the conventional MEMS technology to build micro-machined THz components for the next generation terahertz communications and digital signal processing.

The potential large bandwidth and high propagation speed helps photonic circuitry to be proposed against the above-mentioned challenges faced by its electronic counterpart. Optical-assisted as well as all-optical systems in various forms have been reported to realize different data-processing functionalities. For example, analog-to-digital converters (ADC) with the potential of high speed operation have been demonstrated by optical-assisted or all-optical approaches. Photonic logic has also been reported in numerous works by coding the Boolean information in the amplitude, phase or wavelength of the optical signals. Despite these efforts, however, the key element to address the fundamental deficiencies of CMOS circuit remained missing. The use of optical frequencies in these works brought about common shortcomings including dimension mismatch, lack of coherent detection, inflexibility, susceptibility to mechanical and environmental variations, and the presence of bulky optical elements (i.e., mirrors, beam splitters, lenses, etc.). More seriously, these works inherited sequential circuit designs directly from CMOS. It indicates that the cumulative delay still dominated the speed performance, which prevented further decrease of the circuit latency. In light of these problems, we foresee the implementation of THz circuitry as the next reasonable step to take in designing high-speed analog as well as digital circuits.

Spoofed Surface Plasmon Polariton (SSPP) is known as a pseudo-surface mode in THz frequencies that mimics the slow wave nature and localized E-M field distribution of the plasmon mode typically observed in optical domain. By introducing periodic

corrugations on the surfaces of a metal-dielectric-metal structure, SSPP mode is realized for propagating THz signal, and its mode dispersion is strongly dependent on the geometric dimensions as well as the material properties of the architecture. Recently propagation of THz wave utilizing Spoof surface plasmon polariton (SSPP) earned a great deal of attention due to the ability of SSPP modes to guide THz waves at very low dispersion. In this research, we exploit and investigate the SSPP modes in different periodic structure and utilizing them in different structure to introduce new THz devices, such as, polarization rotator, THz switch, ADC, etc.

CHAPTER I

Introduction

The discovery of p-n junction and the construction of the very first semiconductor transistor decades ago have revolutionized the science of electronics profoundly. Ever since, efforts have been continuously made to design and realize solid-state circuits with smaller size, less power consumption, and higher performance. To-date, very large scale integrated (VLSI) circuit has become the foundation of modern electronics. With the discovery of new materials and the development of advanced fabrication techniques, the dimensions of the VLSI are marching into the sub-10 nm domain with the speed performance achieving gigahertz (GHz) operations.

However, with the ever-growing demand for large scale data transmission and high-speed information processing, the electronics as we know of begins to face serious challenges. Conventional VLSI circuit comprises enormous number of complementary metal-on-semiconductor (CMOS) transistors connected in a preconfigured manner via metallic wires. The transportation of charged carriers in these structures is not only slow, but also power consuming. As a result, a hard speed limit is faced by the circuit designers nowadays. The cumulative path delay and state delay, as well as the temporal jitter of clock signals, contribute to such limit [1, 2].

Photonics, on the other hand, is a promising solution to the challenges as stated above. Unlike charged carriers, photons propagate in the form of electromagnetic (E-

M) waves at a much higher speed, which is close to or comparable with the speed of light. The path delay for the photonic signal to traverse the entire circuit is therefore minimal. The E-M field has instantaneous response as dictated by the bounded solutions to the Maxwells equations, which will further reduce the circuit latency due to the minimized state delay. Moreover, photonics has great bandwidth, ranging from terahertz (1 THz=10^{12} Hz) to 1014 Hz of the visible spectrum. Due to these potential advantages, photonic circuits and networks have attracted enormous research interest in the recent years. Optical-assisted as well as all-optical systems in various forms have been reported to realize different data-processing functionalities [3, 4, 5].

Despite the heated research activities in the optical frequencies, several hurdles remain before this concept can be adopted in real world applications. These hurdles include the enormous frequency difference between photons and electrons, as well as the dimension mismatch between optical and electrical components. Faced by these problems, THz is proposed to be a transitional frequency range that can potentially bridge the disparity between the two. Comparing to optics, THz features lower oscillating frequency of the E-M field, indicating much easier realization of resonant interaction of THz radiations with electrons. Unlike optical waves, the direct energy transfer from photon oscillation to free carrier dynamics in the same time scale is straightforward in THz.

From the electronics end, the THz frequencies provide bandwidth that is magnitudes larger than the GHz range achievable today. Devices that can utilize THz signals are hence promising candidates for increasing the speed of the state-of-the-art electronic components. The photon energy of THz radiation is on the order of meV. For years, it has posed difficulties for the emitter and detector designs at these frequencies. The dilemma between the positive phenomenology of THz in circuit applications and the difficulty in its generation and detection was finally solved with the discovery of resonant THz emission by using semiconductor photoconductive

2

switch, as reported by D. Grischkowsky et al. in the late 1980 [6, 7, 8].

Their pioneering works have been supplemented by the work of Dyakonov and Shur at the beginning of 1990s, where the possibility of generating and detecting THz emissions through the instability of plasmon waves in the field-effect transistor (FET) structure is proposed and demonstrated [9, 10]. To-date, a variety of different technologies have been employed to generate and detect THz radiations in both pulsed and continuous-wave (CW) mode, and THz measurement systems employing these technologies have slowly but steadily matured [11, 12, 13, 14]. With these significant achievement, and fueled by a multitude of research projects that sometimes involve collaborative participants, THz technologies progressed fast in the recent decade, beginning to demonstrate its potential in diverse domains such as astronomy, biosensing, and high-speed data processing [15, 16, 17, 18, 19].

Recent years have seen fast progress in the research field of THz electromagnetics and components, which has long been deemed as missing links between their microwave and optics counterparts. In the upcoming future of the Beyond-Moores Law era of the integrated circuit, higher operation speed of the VLSI can be realized with the integration of THz components into the state-of-the-art CMOS technologies. In CMOS circuits, various functionalities are realized by cascading a network of semiconductor transistors in sequential manners. Regardless of the circuit design and realization, electrical signal needs to propagate between stages of the circuit, where the output from the previous stage serves as the input to the next. Modern chip design requires the combination of large number of stages of various natures in order to achieve complex circuit functions including signal switching, routing, amplification, digitization and Boolean logic operations. Such serial connection and the resultant information pipelining have engendered the following fundamental limitations on the performance of the CMOS technology:

1. Cumulative delay. The circuit latency consists of the time for the electrical

signal to traverse the entire circuit network, and the time for individual transistor or group of transistors to switch their output state upon the input change, known as the path delay and the state delay, respectively. In CMOS circuit, the later stage cannot generate meaningful result unless the outputs from all of its previous stages have stabilized. This phenomenon dictates both the path delay and the state delay to be cumulative.

2. Excessive power consumption. Although the final output is in most cases the only output of significance, the serial cascading of the circuit components requires all intermediate results to be calculated, cached and propagated, producing power consumption associated with each individual step.

3. Limited bandwidth. Ultrafast movement of electrons is inhibited by the finite carrier mobility and the nonideality of common metal and semiconductor materials. The speed limitation is worsened by the parasitic resistance and capacitance of the circuit design. Such delay will scale up significantly with increasing complexity of the circuit. The potential large bandwidth and high propagation speed helps photonic circuitry to be proposed against the above-mentioned challenges faced by its electronic counterpart. For example, analog-to-digital converters (ADC) with the potential of high speed operation have been demonstrated by optical-assisted or all-optical approaches [20, 21, 22, 23]. Photonic logic has also been reported in numerous works by coding the Boolean information in the amplitude, phase or wavelength of the optical signals [24, 25, 26, 27]. Despite these efforts, however, the key element to address the fundamental deficiencies of CMOS circuit remained missing. The use of optical frequencies in these works brought about common shortcomings including dimension mismatch, lack of coherent detection, inflexibility, susceptibility to mechanical and environmental variations, and the presence of bulky optical elements (i.e., mirrors, beam splitters, lenses, etc.). More seriously, these works inherited sequential circuit designs directly from CMOS. It indicates that the cumulative delay still dominated

the speed performance, which prevented further decrease of the circuit latency.

There have been many efforts to utilize surface modes in THz region, various structures have been employed and studied. For example, K. Wang et al. first proposed the transmission of THz radiation as a radially polarized mode on metal wires [28]. Due to the small surface area of the metal wire, the loss is shown to be much smaller than any conventional waveguiding structures available at that time. The TEM-like dispersion relation also minimized the group velocity dispersion, which is critical for time-domain applications where pulsed THz radiations are typically used.

A newly developed method to overcome the group velocity dispersion of terahertz wave and weak guiding at THz frequencies is the utilization of spoof surface palasmon polariton (SSPP) waves confined to the periodically corrugated metallic structures. Such features can be holes, slits, or dimples. Although extraordinary optical transmission for light shining on such surfaces has been studied even before Pendrys work, the main contribution of this work is to conclude that the enhanced subwavelength transmission and E-M field localization can be explained by the existence of spoofed surface plasmon mode on the modified surfaces. He showed that for this kind of mode it is possible to define an effective permittivity which is a is apparently dependent on the geometric dimensions as well as the choice of materials of the modified surface. As long as the periodicity and dimensions of the resonators are much smaller than the wavelength of operation, it is possible to replace the corrugated conducting structure with a metal whose plasma frequency depends on the geometric properties of the grooves. This is the reason that the term spoof surface plasmons used for the confined surface waves propagating along the corrugated perfectly-conducting surface [29, 30]. The Importance of Pendrys work not only lies in the unified theoretical treatment of the spoof surface plasmon on corrugated surfaces, but also in the fact that such resonance can be modified by adjusting the design of the periodic surface features

toward the desired specifications.

Following Pendrys work, different metallic surfaces with periodic structures are studied in order to investigate the transmission, guiding and focusing of E-M radiations, mostly in THz frequencies. For example, C. R. Williams et al. have studied the metal surface perforated with 2-D periodic square holes both quasi-analytically and numerically [31]. They also performed experiments to characterize the mode confinement, and they have shown an increase of approximately two orders of magnitude in terms of mode confinement has been observed for the modified surface compared with the flat structure. Their work proves the Pendrys theoretical prediction, where he claimed strong mode localization within the surface of periodic structure is anticipated [30].

In the light of the aforementioned challenges, we foresee the implementation of THz circuitry as the next reasonable step to take in designing high-speed analog as well as digital circuits. As mentioned in the beginning, THz is easier to be implemented and integrated with electronics as opposed to optics. The use of this frequency domain, when combined with innovative architecture design, will address the fundamental issues that the CMOS circuits are facing at the moment. Unlike optical frequencies, the THz signals are most effectively transmitted and modulated using sub-wavelength surface-mode architectures. We plan to design THz directed logic elements by employing periodically modified metamaterial architectures. These elements can be organized into various setups to realize different circuit functionalities. This thesis is organized as follows:

In Chapter II, by inserting periodic grooves along the direction of propagation in a cylindrical waveguide, a corrugated SSPP waveguide has been constructed. This structure shows strong confinement of electromagnetic energy inside the grooves near their resonant frequency. This property makes it applicable in narrowband THz circuits such as filter or active switches or polarizer rotators. By applying special

materials into the circular SSPP waveguide, for example, anisotropic dielectric, the polarization state of the THz travelling wave, will be preferably selected at input and will evolve while propagating. If, in addition, we can control the refractive indices through external stimuli, we can accommodate the output polarization of the THz signal to our needs.

Chapter III introduces a new THz switch comprising the (cylindrical spoof surface plasmon polariton) C-SSPP structure. We demonstrate that the C-SSPP has strong mode confinement, discrete transmission bands, and high quality factor in THz domain. The proposed switch works based on waveguide-cavity-waveguide (WCW) structure. The cavity is connected to identical corrugated cylindrical waveguides in both sides. The new structure can work as an active switch or modulator. Furthermore, the high-quality factor cavity and small effective area enable the device to function at the small refractive index modulation $((\delta n_d)n_d)$ induced by applying voltage to the metal electrode connections.

Chapter IV discusses about analog to digital converter based on the spatial detection. The key mechanism behind spatial detection is the deflection of output signal at different angles with changing analog input. In order to realize this functionality, spoofed surface plasmon polariton (SSPP) architecture is employed. Such structure features SSPP mode with a slow-wave nature and strong field confinement. These properties are not only critical to the THz signal transmission over distance, but are also the key for localized modulation of the THz signals with enhanced efficiency. We have shown that the phase constant of the one dimensional SSPP (1D-SSPP) is sensitive enough to the refractive index of the material inside the grooves. Then using the plasmonic behavior of the 1D-SSPP dispersion diagram and its sensitivity to the refractive index inside the grooves, we have shown that one can reach beam steering around 42 degrees in a short length of the waveguide.

In Chapter V, we have presented an investigation of the SSPP beam splitter, one

of the key elements of many optical setups. In contrast with conventional free space implementations, in the case of the SSPP beam splitter one can no longer disregard scattering of incoming wave back into the input channels. Thus, SSPP implementations must take into consideration both the splitting ratio and the backscattering as important parameters characterizing the beam splitter. Three different designs representing different approaches to solving the problem of the relation between these parameters are investigated. The mathematical formalism to study the dispersion diagrams is proposed. The frequency dependence of splitting ratio, scattering parameters and backscattering for each beam splitter is investigated. Finally, by employing one of the proposed beam splitter a controllable filter is designed and analyzed.

In Chapter VI, the Maxwell stress tensor for the field inside a spoof surface plasmon polariton (SSPP) waveguide and the electromagnetic force distribution acting on a dielectric particle are investigated. We have shown that for particles made of material with the dielectric function slightly different from that of the medium filling the waveguide, the force distribution is fully described by the SSPP field in the absence of the particle. The spatial profile of the field strongly depends on the relation between the operating frequency and the SSPP resonance frequency. We have illustrated that varying the characteristic frequencies introduces a switching effect, when the direction of the force along the waveguide axis changes its direction (from toward the grooves to away from them). We have proposed a pumping mechanism based on force acting on a small particle inside the SSPP waveguide

Chapter VII's objectives is to offer a highly sensitive THz sensor for detection of hazardous material and biological agents. At first single and double ring resonator are placed on a single unit-cell and are investigated. A thin layer of dielectric is added on top of the metallic rings to increase field concentration near the rings and increases the THz wave matter interactions. At the end, by constructing a hybrid Fano-resonant metallic microstructure array-insulator-metal (MIM) configuration, a novel absorp-

tive metamaterial cavity sensor is proposed. The sensitivity and resolution of meta-material sensors are compared with the current state of the art metamaterial THz sensors.

In the last chapter of this thesis, we have discussed about the fabrication of some SSPP waveguide and the future plan to improve the quality of previous fabricated samples. ALso a new one-dimensional structure that can support SSPP modes with much simpler fabrication process is suggested.

CHAPTER II

THz Polarization Controller Based on Cylindrical Spoof Surface Plasmon Polariton (C-SSPP)

2.1 Introduction

Surface plasmons result from the oscillation of plasma along the interface of metal and dielectric. It happens as a result of negative dielectric of certain metal below the plasma frequency. There have been some theoretical and experimental works to utilize these modes in frequency range (0.3-10 THz) [32, 33, 34]. Besides there are efforts to utilize conventional waveguides such as metallic wires, tubes, index-guiding silicon slab waveguides or sapphire fibers, etc. unfortunately the conventional metallic tube waveguides are not suitable because of their high loss, Si waveguide are not flexible and some waveguides such as sub-wavelength metal wire has high bending loss and coupling difficulty [34, 35, 36, 37]. A newly developed method to overcome the group velocity dispersion of terahertz wave and weak guiding at THz frequencies is the utilization of spoof surface palasmon polariton (SSPP) waves confined to the periodically corrugated metallic structures [38, 28, 39, 40, 41, 42, 43, 44, 45, 46, 47, 48, 49, 50, 51, 52, 53, 54]. These SSPP modes exhibit features such as field enhancement and localization. In this technique the transverse mode of SSPP follow the same behavior of surface plasmons at interface of metal dielectric at optical frequencies.

It has been first shown by Wang, et al that it is possible to have dispersion-less propagation along metallic wire surrounded by dielectric at THz frequency [28]. Later Pendry et al. proposed a periodic structure containing grooves at metallic dielectric interface to support THz propagation [38].

As long as the periodicity and dimensions of the resonators are much smaller than the wavelength of operation, it is possible to replace the corrugated conducting structure with a metal whose plasma frequency depends on the depth of the grooves. This is the reason that the term spoof surface plasmons used for the confined surface waves propagating along the corrugated perfectly- conducting surface [55]. In [56, 57] the corrugated SSPP structures have been realized by placing rectangular resonator along the propagation path of rectangular waveguide and the parallel plate waveguide.

In our work, by inserting periodic grooves along the direction of propagation in a cylindrical waveguide, a corrugated SSPP waveguide has been constructed. This structure shows strong confinement of electromagnetic energy inside the grooves near their resonant frequency. This property makes it applicable in narrowband THz circuits such as filter or active switches or polarizer rotators. By applying special materials into the circular SSPP waveguide, for example, anisotropic dielectric, the polarization state of the THz travelling wave, will be preferably selected at input and will evolve while propagating. If, in addition, we can control the refractive indices through external stimuli, we can accommodate the output polarization of the THz signal to our needs.

2.2 Cylindrical Spoof Surface Plasmon Polariton (C-SSPP) waveguide

The structure under investigation consists of a dielectric cylindrical part covered by perfect electric conductor (PEC). As mentioned before, the proposed SSPP struc-

ture is a periodic device. In order to calculate the dispersion relationship, electromagnetic fields need to be calculated in one period. Figure 2.1 shows the overall view of SSPP waveguide and the unit cell of structure. As can be seen, one period of waveguide has been divided into two regions. Region 1 acts as a cylindrical waveguide, while Region 2 is a cylindrical resonator.
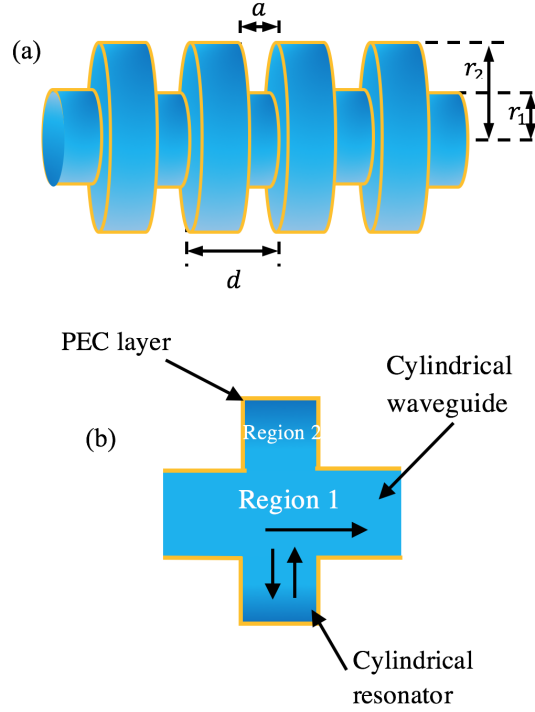
Figure 2.1: (a) Schematic view of the corrugated cylindrical waveguide. (b) The unit cell of the structure.

In our convention,d is the period of the grooves, a and R_2 represent the width and radius of the grooves, while R_1 is the radius of the smooth part of the waveguide. Moreover, the permittivity of Region 1 and grooves can be denoted by n_d. Based on Maxwells equations, mathematical expressions of the TM-polarized waves propagating in z direction along grooves are explicitly written out for both Regions 1 and 2. To this goal the magnetic and electric vector potentials in Region 1 can be assumed as $A_1 = \psi_{a1}\hat{z}$ and $F_1 = \psi_{f1}\hat{z}$. In which:

12

$$\psi_{a1} = I_N(k_\rho\rho)cos(N\phi)e^{-ik_z^m z} \tag{2.1a}$$

$$\psi_{f1} = I_N(k_\rho\rho)sin(N\phi)e^{-ik_z^m z} \tag{2.1b}$$

In Equations (2.1a) and (2.1b), $I_N(k_\rho\rho)$ is the modified Bessel function of the first kind, ρ represents radius and k_ρ is propagation constant in direction of ρ. As is common in solving Maxwell equations in periodic structures, the EM field can be best represented by a Bloch-Floquet mode expansion.k_z^m , therefore, denotes the wavevector of mth-order Bloch-Floquet mode along z-axis and is expressed by:

$$k_z^m = k_z + \frac{2m\pi}{L} \tag{2.2}$$

Similarly, the magnetic vector potential in Region 2 is assumed to be a vector along the z-axis as expressed by $A_2 = \psi_{a2}\hat{z}$ and $F_2 = \psi_{f2}\hat{z}$. In which:

$$\psi_{a2} = (A^+ H_N^2(k_{\rho_2}\rho) + A^- H_N^1(k_{\rho_2}\rho)cos(N\phi)cos(\frac{\pi}{a}z) \tag{2.3a}$$

$$\psi_{f2} = (B^+ H_N^2(k_{\rho_2}\rho) + B^- H_N^1(k_{\rho_2}\rho)sin(N\phi)sin(\frac{n\pi}{a}z) \tag{2.3b}$$

The term $cos(\frac{n\pi}{a}z)$ and $sin(\frac{n\pi}{a}z)$ is included in the expression in order to guarantee that E_ρ vanishes at z=0 inside the resonators. The fields are assumed as upward and downward waves, and $H_N^{1,2}(k_{\rho_2}\rho)$ are Hankel functions of the first and second kind, respectively:

$$H_N^2(\rho) = J_N(\rho) - iN_N(\rho) \tag{2.4a}$$

$$H_N^1(\rho) = J_N(\rho) + iN_N(\rho) \tag{2.4b}$$

Having the electric and magnetic vector potential in both regions EM field components can be calculated as follows:

$$\vec{D} = \frac{1}{i\omega}\nabla \times \nabla \times \vec{A} - [\epsilon]\nabla \times \vec{F} \tag{2.5a}$$

$$\vec{H} = \frac{1}{i\omega\mu}\nabla \times \nabla \times \vec{F} + [\epsilon]\nabla \times \vec{A} \tag{2.5b}$$

Where $[\epsilon]$ is a function refractive index of dielectric. We can write D and H fields in both regions. For the TM_z modes D and H fields are as follow:

$$\begin{bmatrix} D_\rho \\ D_\phi \\ D_z \end{bmatrix} = \sum_{m=-M}^{M} \begin{bmatrix} -A_m\frac{k_z}{\omega}k_\rho J_N'(k_\rho\rho)cos(N\phi)e^{-ik_z^m z} \\ A_m\frac{k_z}{\omega\rho}k_z J_N(k_\rho\rho)sin(N\phi)e^{-ik_z^m z} \\ \frac{A_m}{\omega}(k^2 - k_z^2)J_N(k_\rho\rho)cos(N\phi)e^{-ik_z^m z} \end{bmatrix} \tag{2.6a}$$

$$\begin{bmatrix} H_\rho \\ H_\phi \\ H_z \end{bmatrix} = \sum_{m=-M}^{M} \begin{bmatrix} A_m\frac{-N}{\rho}J_N(k_\rho\rho)csin(N\phi)e^{-ik_z^m z} \\ -A_m k_\rho J_N'(k_\rho\rho)sin(N\phi)e^{-ik_z^m z} \\ 0 \end{bmatrix} \tag{2.6b}$$

Region 2:

14

$$
\begin{bmatrix} D_\rho \\ D_\phi \\ D_z \end{bmatrix} = \sum_{m=-M}^{M} \begin{bmatrix} \frac{1}{i\omega\epsilon}\frac{n\pi}{a}k_{\rho 2}(A^+ H'_{N^2}(k_{\rho 2}\rho) + A^- H'_{N^1}(k_{\rho 2}\rho))cos(N\phi)cos(\frac{n\pi}{a}z) \\ \frac{1}{i\omega\epsilon\rho}\frac{n\pi}{a}(A^+ H^2_N(k_{\rho 2}\rho) + A^- H^1_N(k_{\rho 2}\rho))cos(N\phi)sin(\frac{n\pi}{a}z) \\ \frac{1}{i\omega\epsilon}(k^2 - (\frac{n\pi}{a})^2)\frac{n\pi}{a}(A^+ H^2_N(k_{\rho 2}\rho) + A^- H^1_N(k_{\rho 2}\rho))cos(N\phi)cos(\frac{n\pi}{a}z) \end{bmatrix}
$$

$$(2.7a)$$

$$
\begin{bmatrix} H_\rho \\ H_\phi \\ H_z \end{bmatrix} = \sum_{m=-M}^{M} \begin{bmatrix} \frac{-N}{\rho}(A^+ H^2_N(k_{\rho 2}\rho) + A^- H^1_N(k_{\rho 2}\rho))sin(N\phi)cos(\frac{n\pi}{a}z) \\ -ik_\rho(A^+ H'_{N^2}(k_{\rho 2}\rho) + A^- H'_{N^1}(k_{\rho 2}\rho))cos(N\phi)cos(\frac{n\pi}{a}z) \\ 0 \end{bmatrix}
$$

$$(2.7b)$$

And for the TE_z modes the D and H fields can be written as:

Region 1:

$$
\begin{bmatrix} D_\rho \\ D_\phi \\ D_z \end{bmatrix} = \sum_{m=-M}^{M} \begin{bmatrix} B_m \frac{N}{\rho} I_N(k_\rho\rho)cos(N\phi)e^{-ik_z^m z} \\ B_m k_\rho I_N(k_\rho\rho)sin(N\phi)e^{-ik_z^m z} \\ 0 \end{bmatrix}
$$

$$(2.8a)$$

$$
\begin{bmatrix} H_\rho \\ H_\phi \\ H_z \end{bmatrix} = \sum_{m=-M}^{M} \begin{bmatrix} -B_m ik_\rho k_z^m I'_N(k_\rho\rho)sin(N\phi)e^{-ik_z^m z} \\ B_m \frac{N}{\rho} ik_z^m I_N(k_\rho\rho)cos(N\phi)e^{-ik_z^m z} \\ B_m (k_z - k_z^{m2}) I_N(k_\rho\rho)sin(N\phi)e^{-ik_z^m z} \end{bmatrix}
$$

$$(2.8b)$$

Region 2:

$$
\begin{bmatrix} D_\rho \\ D_\phi \\ D_z \end{bmatrix} = \sum_{m=-M}^{M} \begin{bmatrix} \frac{N}{\rho}k_\rho 2(B^+ H_{N^2}(k_{\rho 2}\rho) + B^- H_{N^1}(k_{\rho 2}\rho))sin(N\phi)cos(\frac{n\pi}{a}z) \\ k_{\rho 2}(B^+ H'_{N^2}(k_{\rho 2}\rho) + B^- H'_{N^1}(k_{\rho 2}\rho))sin(N\phi)sin(\frac{n\pi}{a}z) \\ 0 \end{bmatrix}
$$

$$(2.9a)$$

$$
\begin{bmatrix} H_\rho \\ H_\phi \\ H_z \end{bmatrix} = \sum_{m=-M}^{M} \begin{bmatrix} \frac{n\pi}{a}k_{\rho 2}(B^+ H_N^2(k_{\rho 2}\rho) + B^- H_N^1(k_{\rho 2}\rho))sin(N\phi)cos(\frac{n\pi}{a}z) \\ -\frac{N}{\rho}\frac{n\pi}{a}(B^+ H'_{N^2}(k_{\rho 2}\rho) + B^- H'_{N^1}(k_{\rho 2}\rho))cos(N\phi)cos(\frac{n\pi}{a}z) \\ k_{\rho 2}(B^+ H'_{N^2}(k_{\rho 2}\rho) + B^- H'_{N^1}(k_{\rho 2}\rho))sin(N\phi)sin(\frac{n\pi}{a}z) \end{bmatrix}
$$

$$(2.9b)$$

Now that the full field expressions are derived, the boundary conditions for tangential fields at the interface of Regions 1 and 2 need to be satisfied. As $a << 1$ the only modes that can propagate in the grooves are the fundamental modes with $n = 0$ for TM_z and $n = 1$ for TE_z. Now we can implement the boundary conditions for D and H fields. Writing the boundary condition for D_z and H_z can be further transcribed as:

$$
\sum_{m=-M}^{m=M} -B_m(k_0^2 - k_z^{m2})I_N(k_\rho R_1)e^{-ik_z^m z} =
$$
$$
(k_0^2 - \frac{\pi}{a}^2)((B^+ H_N^2(k_{\rho_2}R_1) + B^- H_N^1(k_{\rho_2}R_1)sin(\frac{n\pi}{a}z)) \tag{2.10}
$$

And

$$
\sum_{m=-M}^{m=M} A_m(k_0^2 - k_z^{m2})I_N(k_\rho R_1)e^{-ik_z^m z} =
$$
$$
k_0^2((A^+ H_N^2(k_{\rho_2}R_1) + A^- H_N^1(k_{\rho_2}R_1) \tag{2.11}
$$

In addition, at $\rho = R_2$ the tangential electric field should vanish. Therefore we

have: $A^+H_N^2(k_{\rho_2}R_2) = A^-H_N^1(k_{\rho_2}R_2)$ and $B^+H_N^{2'}(k_{\rho_2}R_2) = B^-H_N^{1'}(k_{\rho_2}R_2)$. Then we only need to write out the boundary condition for the remaining two fields, H_ϕ and D_ϕ note that for TM_z mode $D_{\phi 1} = D_{\phi 2} = 0$. By solving the boundary condition and eliminating B^- and A^- the dispersion relation for the SSPP modes can be obtained as:

$$\sum_{m=-M}^{m=M} A_m(k_0^2 - k_z^{m2})I_N(k_\rho R_1)e^{-ik_z^m z} = k_0^2((A^+H_N^2(k_{\rho_2}R_1) + A^-H_N^1(k_{\rho_2}R_1) \quad (2.12a)$$

$$A_m = (\frac{-k_{\rho 2}}{k_\rho})\frac{H_N^1(k_{\rho 2}R_2)H_N^2(k_{\rho 2}R_1) - H_N^2(k_{\rho 2}R_2)H_N^1(k_{\rho 2}R_1)}{H_N^1(k_{\rho 2}R_2)H_N^{2'}(k_{\rho 2}R_1) - H_N^2(k_{\rho 2}R_2)H_N^{1'}(k_{\rho 2}R_1)}C_m^2 \quad (2.12b)$$

$$B_m = (\frac{k_{\rho 2}}{k_\rho})\frac{H_N^1(k_{\rho 2}R_2)H_N^{2'}(k_{\rho 2}R_1) - H_N^2(k_{\rho 2}R_2)H_N^{1'}(k_{\rho 2}R_1)}{H_N^1(k_{\rho 2}R_2)H_N^{2'}(k_{\rho 2}R_1) - H_N^2(k_{\rho 2}R_2)H_N^{1'}(k_{\rho 2}R_1)}C_m^2 \quad (2.12c)$$

$$A = H_N^1(k_{\rho 2}R_2)H_N^2(k_{\rho 2}R_1) - H_N^2(k_{\rho 2}R_2)H_N^1(k_{\rho 2}R_1) \quad (2.12d)$$

$$B = H_N^1(k_{\rho 2}R_2)H_N^{2'}(k_{\rho 2}R_1) - H_N^2(k_{\rho 2}R_2)H_N^{1'}(k_{\rho 2}R_1) \quad (2.12e)$$

By finding the eigenvalues of Equation 2.12a, the dispersion diagram for hybrid modes can be obtained. For special cases, if there is just TM_z modes inside the waveguide, Equation 2.12a reduces to:

$$\sum_{m=-M}^{m=M} (\frac{-k_{\rho 2}}{k_\rho})\frac{I_N'(k_\rho R_1)}{I_N(k_\rho R_1)}\frac{H_N^1(k_{\rho 2}R_2)H_N^2(k_{\rho 2}R_1) - H_N^2(k_{\rho 2}R_2)H_N^1(k_{\rho 2}R_1)}{H_N^1(k_{\rho 2}R_2)H_N^{2'}(k_{\rho 2}R_1) - H_N^2(k_{\rho 2}R_2)H_N^{1'}(k_{\rho 2}R_1)}\frac{C_m^2}{\frac{\pi}{2a}} = 1$$

$$(2.13)$$

For the TE_z modes, we have:

$$\sum_{m=-M}^{m=M} (\frac{k_\rho}{k_{\rho 2}})\frac{I_N(k_\rho R_1)}{I_N'(k_\rho R_1)}\frac{H_N^1(k_{\rho 2}R_2)H_N^{2'}(k_{\rho 2}R_1) - H_N^2(k_{\rho 2}R_2)H_N^{1'}(k_{\rho 2}R_1)}{H_N^1(k_{\rho 2}R_2)H_N^2(k_{\rho 2}R_1) - H_N^2(k_{\rho 2}R_2)H_N^1(k_{\rho 2}R_1)}\frac{C_m^2}{\frac{\pi}{2a}} = 1$$

$$(2.14)$$

where, the additional variables are defined as:

$$C_m = \sqrt{\frac{a}{d}} sinc(\frac{k_z^m a}{2\pi}) \tag{2.15a}$$

$$k_\rho^2 + k_z^{m2} = n_d^2 K_0^2 \tag{2.15b}$$

$$k_{\rho 2}^2 + \frac{n^2 \pi^2}{a} = n_d^2 K_0^2 \tag{2.15c}$$

Note that the dispersion equations in Equations (2.12a), (2.13), and (2.14) are not only a function of cylindrical waveguide geometries but also depend on the refractive index of the dielectric inside the SSPP.

It was mentioned before that $a << 1$, and the only modes that can propagate inside the grooves are the fundamental modes with $n = 0$ for TM_z and $n = 1$ for TE_z. Based on Equations (2.8a),(2.8), (2.9a), and (2.9b), there will be no TE_z modes inside grooves; it can exist just at very high frequency in which the wavelength is comparable to the width of the grooves. Fortunately, this case is not of our interest. Then, we can have TE_z in smooth parts of waveguide but inside the grooves there will be only TM_z modes. The dominant mode in the smooth part of cylindrical waveguide is TE_{11} and to satisfy the boundary conditions, the TM mode inside the grooves should be TM_{10}.

2.3 Numerical results and discussion

Now that we have developed a mathematical model for the corrugated cylindrical SSPP architectures, the dispersion diagram of such a structure can be obtained by numerically solving Equations (2.13) and (2.14).

Figure 2.2 for example, shows the dispersion diagram of the azimuthal mode with $N = 0$ for a structure with the dimensions of $R_1 = 120 \ \mu m, R_2 = 200 \ \mu m, d = 100 \ \mu m$
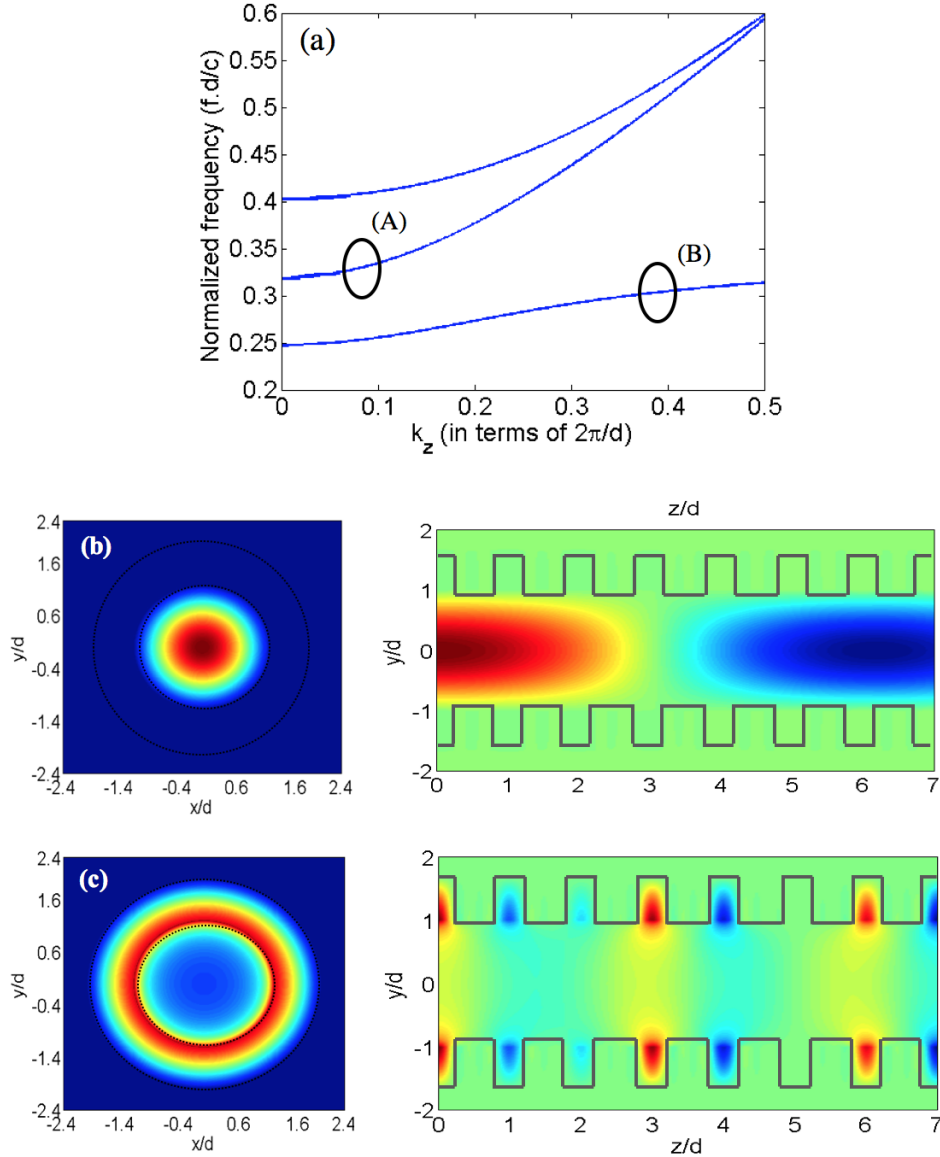
Figure 2.2: Dispersion diagram of cylindrical SSPP structure. (b, c) distribution in cross section of SSPP waveguide at two different frequencies. (d, e) Electric field magnitude along z-direction inside the waveguide.

and $a = 30\ \mu m$. As can be observed, around a normalized frequency of 0.31 ($1THz$) (point B) the SSPP waveguide can act as a slow wave structure. A transmission band gap exists as the structure reaches its resonance state. In Figure 2.2 (b) and (c) the field distributions are illustrated at two different frequencies, the cross section and along the z-direction inside the waveguide at corresponding frequencies. It can be seen that most of the energy is concentrated in the center region of the SSPP waveguide

when it is off resonance. The EM field confinement within the groove region is clearly demonstrated when the frequency is close to the band gap. In Figure 2.2(a) the behavior of the dispersion diagram of first mode is like the dispersion of surface plasmons along the dielectric metal interface. As a result, we can assume this mode as a SSPP mode with the normalized resonant frequencies of 0.314. The resonant frequency of SSPP waveguide is determined by the resonant frequency of grooves. The two parameters to tailor the resonant frequency of the grooves are width and height. In our case, the height is much larger than the width. Then, the resonance along the width occurs in smaller wavelengths compared to the resonance along the height. As our wavelength of interest is comparable to the height, by adjusting the height of the grooves we can control the resonant frequency. As it was mentioned prior, the dominant modes in resonator are TM modes. Thus the resonant frequency can be approximated by using the conventional formula for TM resonant frequency of ring resonators.

For the purpose of comparison, the transmission characteristics of the cylindrical SSPP waveguide are calculated using HFSS [58] and are included here in Figure 2.3. The dimensions of SSPP waveguide under investigation are $R_1 = 120 \ \mu m, R_2 = 200 \ \mu m, d = 100 \ \mu m$ and $a = 30 \ \mu m$. Based on Fig. 3 a band gap around $f = 0.95 \ THz$ is clearly observed, which is in agreement with the result we obtained by applying our analytical model in Figure 2.2.

In figure 2.4 the dispersion diagram for different azimuthal modes ($N = 1 \ 4$) is illustrated. Dimensions of the waveguide in this case remain the same as the structure studied in Figure 2.2. It can be observed that with higher order azimuthal mode, the dispersion curve becomes closer to the light line. As a result, the slow-wave propagation of the input signal in such mode will be observed at slightly higher frequency.

Figure 2.4 shows E_z intensity at certain frequency below the light line for $N = 4$
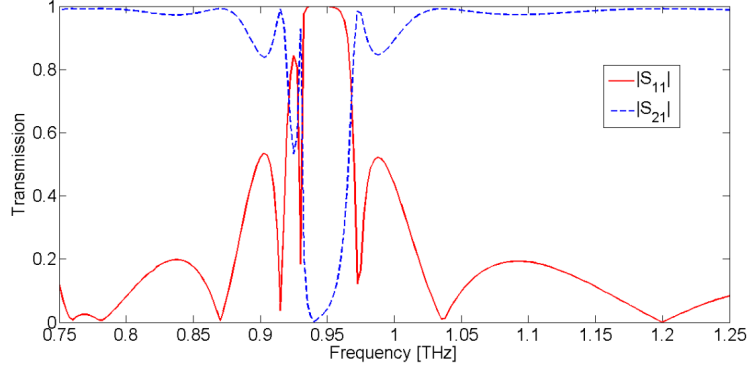
Figure 2.3: Transmission characteristic of cylindrical waveguide for $R_1 = 120 \ \mu m, R_2 = 200 \ \mu m, d = 100 \ \mu m$ and $a = 30 \ \mu m$
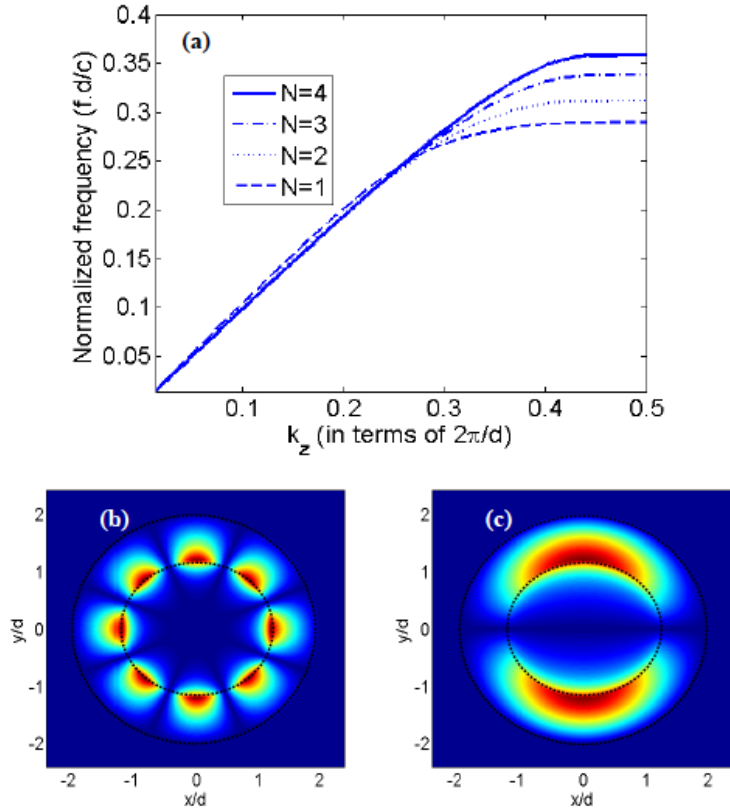
Figure 2.4: Dispersion diagram for different azimuthal modes. distribution in cross section of SSPP waveguide for (b) azimuthal mode N=4 and normalized frequency of 0.3537 (c) azimuthal mode $N = 4$ and normalized frequency of 0.3218.

and $N = 1$ which is obtained using our analytical modeling. It can be seen, that a great portion of the power is confined in the resonators. Figure 2.5, on the other

hand, shows the dispersion diagram for first azimuthal mode and different groove dimensions. Other waveguide dimensions in Figure 2.5 are kept as $R_1 = 120~\mu m$, $R_2 = 200~\mu m$, $d = 100~\mu m$ and $a = 30~\mu m$. It is seen in Figure 2.5 that larger groove size in general results in lowered dispersion curves. In addition, narrower passing band is also observed as the groove becomes larger. An intuitive explanation to this phenomenon is the more significant mismatch between the two waveguiding sections in this scenario, which makes it more susceptible to any frequency shift from the transmission maximum.
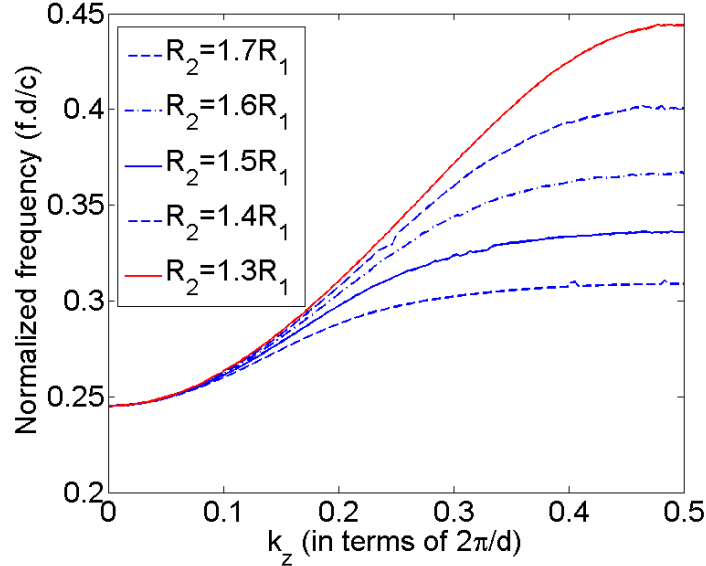
Figure 2.5: Dispersion diagram for first azimuthal mode with different groove height.

2.4   Polarization controller

In this section, by inserting the anisotropic dielectric material inside the SSPP waveguide, a polarization rotator is constructed. It has been discussed that the Equations (2.13) and (2.14) are function of refractive index. This means that by changing the refractive index inside the waveguide, the propagation constant can be tuned; if the refractive indices in the x and y direction are not equal, each electric

22

component in the x and y direction will experience a different propagation constant. As a result, if we expand the input polarization in terms of the x and y polarization state, it is possible to insert phase difference between these two components along the propagation path. This can lead to the polarization state change which is valid if the polarization state of the input wave can be determined. Figure 2.6 shows how electric field direction evolves while propagating.
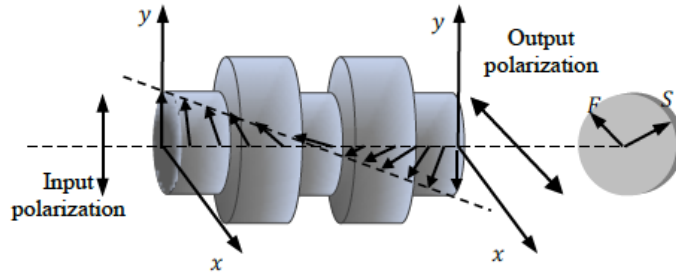
Figure 2.6: Schematic view of the rotation of electric field inside the waveguide.

Figure 2.7 shows the electric fields inside the circular waveguide. As can be seen, in the circular waveguide the electric fields at dominant mode are not particularly in a specific direction, but it is possible to assume that they are mostly in a certain direction (in this case in $y = -x$ direction).
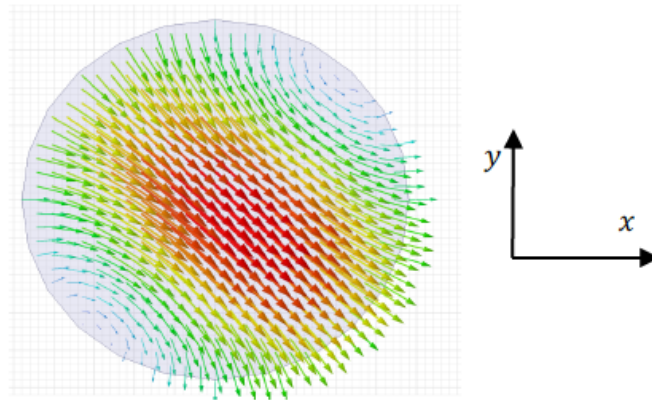
Figure 2.7: The polarization of electric field inside the circular waveguide.

Figure 2.8 shows the dispersion diagram of the SSPP waveguide for two different

23

sets of refractive indices: $(n_x, n_y, n_z) = (1.501, 1.501, 1.501)$ and $(1.501, 1.680, 1.501)$. The dimensions are $R_1 = 120\ \mu m, R_2 = 200\ \mu m, d = 100\ \mu m$ and $a = 20\ \mu m$. As can be seen, if the operation frequency is in the flat part of dispersion diagram, where the behavior of the dispersion diagram is like the dispersion of surface plasmons along the dielectric metal interface, the phase different between the x and y electric components compare to the conventional circular waveguide would be greater. Then the required waveguide length to evolve the polarization state of the input signal would be smaller.
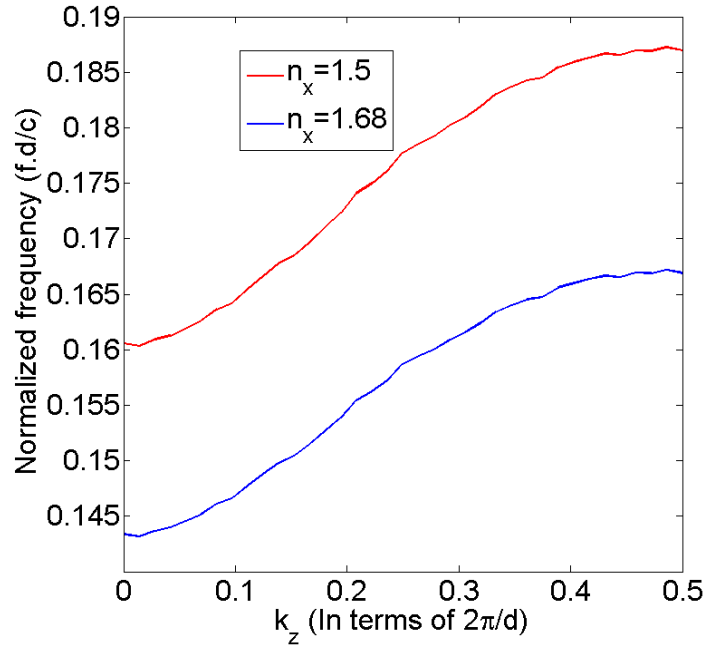
Figure 2.8: The dispersion diagram of the same SSPP for two different sets of refractive indices: $(n_x, n_y, n_z) = (1.501, 1.501, 1.501)$ and $(1.501, 1.680, 1.501)$.

Figure 2.9 shows the polarization of electric field inside the SSPP waveguide for $n_x = n_y = n_z = 1.501$ at $0.550THz$. As the dominant mode in the SSPP waveguide is for $N = 1$, then, if for example the input electric fields are in the x direction, the most part of the power will be along the E_x. Then n_x will be seen inside the waveguide. Therefore, to find the dispersion diagram for SSPP waveguide with anisotropic dielectric inside it, it is possible to use the Equation (2.13) in this case. To change the horizontal polarization to vertical state or vice versa, it is needed at first

to decompose the input wave into vertical and horizontal polarization, respectively. Then, by inserting 180 degree phase change between them, the polarization state will rotate.
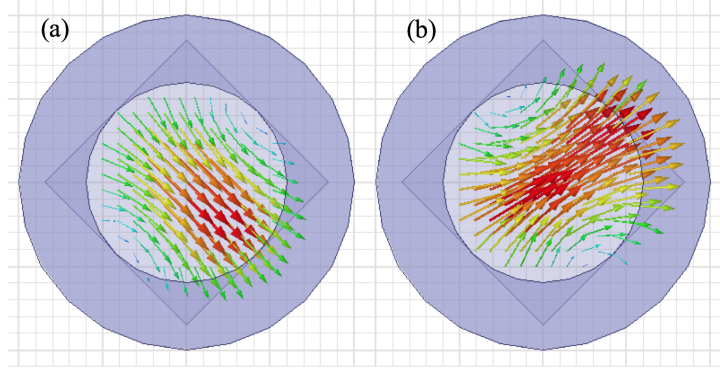
Figure 2.9: The polarization of electric field inside the SSPP waveguide for $(n_x, n_y, n_z) = (1.501, 1.501, 1.501)$.

To simulate this process in HFSS it is necessary at first to control the input polarization. To this goal, the excitation of SSPP is done by a rectangular waveguide. This will forcefully define the input polarization. To decompose the input polarization into two polarization states, it is just enough to rotate the rectangular waveguide in respect to the x or y axis. Figure 2.9 shows output polarization for the two set of refractive indices of Figure 2.8. The length of linear polarization rotator is about 5 periods. The length of the SSPP waveguide to rotate the polarization can be calculated using the following simple formula:

$$l = \frac{\pi}{\beta_2 - \beta_1} \tag{2.16}$$

In the above, β_2 and β_1 are propagation constants in two refraction indices. To change the horizontal polarization to circular or elliptical state, the 180 degrees of phase change between x and y elements of electric fields should be reduced to 90

degrees. Then in Equation (2.16) the length of the waveguide just need to be half of previous one. Figure 10 shows the dispersion diagram of SSPP waveguide. The dimensions are $R_1 = 120~\mu m, R_2 = 200~\mu m, d = 100~\mu m$ and $a = 20~\mu m$. The length of circular polarization rotator is about 3 periods.
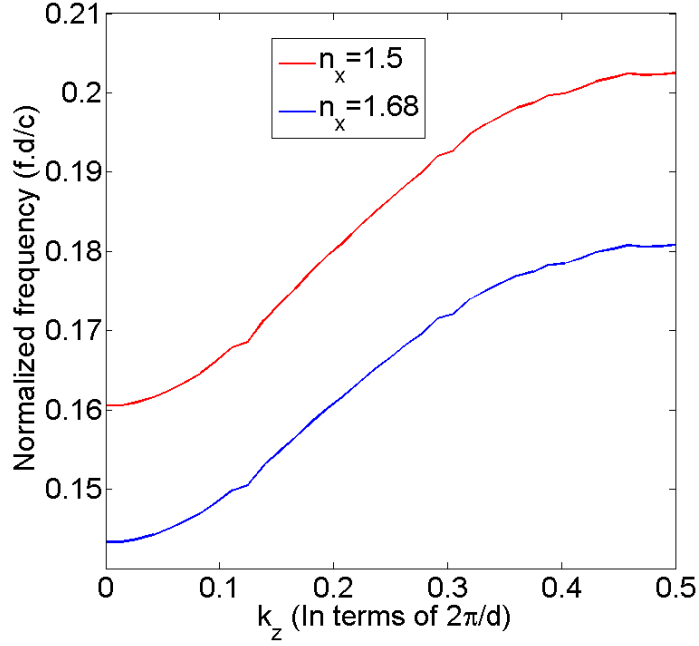
Figure 2.10: The dispersion diagram of SSPP for two different sets of refractive indices: $(n_x, n_y, n_z) = (1.501, 1.501, 1.501)$ and $(1.501, 1.680, 1.501)$.

Figure 2.11 shows output polarization for the SSPP waveguide with dispersion diagram shown in Figure 2.10. The electric fields are shown in for different time slots. As can be seen the output fields direction is rotating in time. It is worthy to note that if the calculated length was not the integer multiplicand of the periodicity, then the simulation result may be a little bit different from what was expected. In that case, some tuning is required to get the desired result.
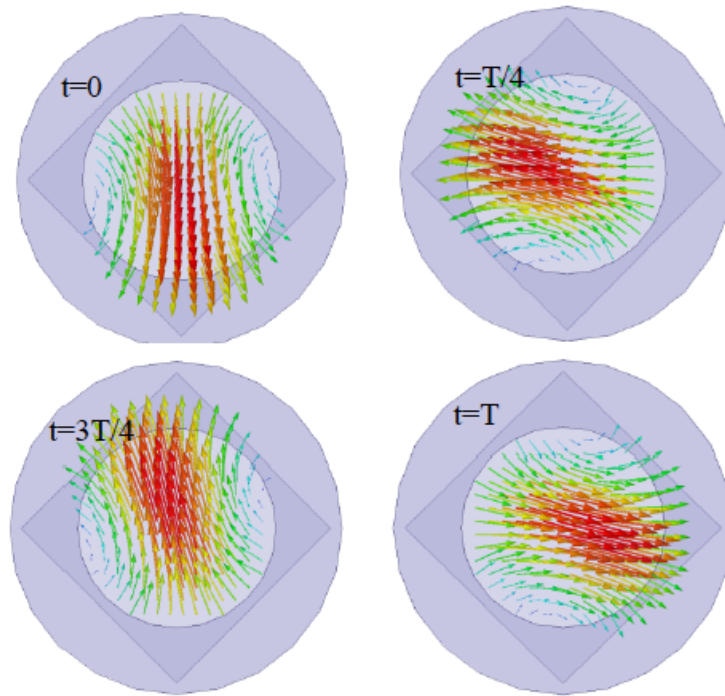
Figure 2.11: Rotation of electric field inside the SSPP waveguide for different times at $0.510THz$.

CHAPTER III

Terahertz Switch Based on Waveguide-Cavity-Waveguide Comprising Cylindrical Spoof Surface Plasmon Polariton (C-SSPP)

The THz generation and detection techniques have been available for years, but there have been few reports on commercial THz products until now [59]. One reason is due to the lack of components to do manipulations and operations on THz signals. In the area of designing controllable THz devices such as Boolean gates; metamaterials, liquid crystal (LC), or nonlinear metamaterials are potentially suitable, as they have low absorption in the THz range. But there are still some challenges that need to be resolved before those devices can be used in THz Boolean circuitry. For the LCs, distributed voltage needs to be applied along the LC to make it uniformly polarized. Also, the switching speed of LCs is significantly slow. The metamaterial structures are comparably big with respect to LC structure and they work in free space communications. Kerr materials need to be pumped by optical signals to tune their loss or refractive index. This requires mostly high power optical pumping. To overcome the mentioned problems about LCs and Kerr materials, semiconductors (Si, InSb) are used [60, 61, 62], then by free carrier injection through a p-i-n junction, the

transmittance, or coupling efficiency, of their proposed structures in THz frequencies can be controlled. Due to the large imaginary part of Si permittivity in THz range, such design can only be effectively used up to near-infrared frequencies. In this chapter, we propose a new THz switch comprising the (cylindrical spoof surface plasmon polariton) C-SSPP structure. We demonstrate that the C-SSPP has strong mode confinement, discrete transmission bands, and high quality factor in THz domain. The proposed switch works based on waveguide-cavity-waveguide (WCW) structure. The cavity is connected to identical corrugated cylindrical waveguides in both sides. The new structure can work as an active switch or modulator. Furthermore, the high quality factor cavity and small effective area enable the device to function at the small refractive index modulation $(\frac{\delta n_d}{n_d})$ induced by applying voltage to the metal electrode connections.

3.1   WCW structure and the Drude model

In this section, we investigate the waveguide-cavity-waveguide structure for THz switches and the mechanism to control the flow of electromagnetic fields inside the structure. The dielectric constant of a semiconductor can be described as a function of frequency using the Drude model [63, 64]

$$\epsilon(\omega) = \epsilon_\infty - \frac{\omega_p^2}{\omega(\omega + i\Gamma)} \tag{3.1}$$

in which

$$\omega_p = \sqrt{\frac{Ne^2}{m_e\epsilon_\infty\epsilon_0}} \tag{3.2a}$$

$$\epsilon_\infty = \epsilon_s \left(\frac{\omega_{TO}}{\omega_{LO}}\right)^2 \tag{3.2b}$$

29

To implement the optical phonon vibrations of crystal lattice in heteropolar semi-conductor at higher frequency, the Drude model needs some modifications. For the heteropolar semiconducturs, the split of transverse and longtitidinal phonon energies at zero momentum give rise to an extra term in the permittivity calculation formula. The modified Drude model can be described as [64]

$$\epsilon(\omega) = \epsilon_\infty (1 + \frac{\omega_{TO}{}^2 - \omega_{LO}{}^2}{\omega_{TO}{}^2 - \omega^2 - i\omega\gamma} - \frac{\omega_p^2}{\omega(\omega + i\omega\Gamma)}) \tag{3.3}$$

The variables in Equation (3.3) are explained in Table 3.1. Using Equation (3.3), the dielectric constant of GaAs is calculated versus frequency in Figure 3.1(a). The effect of phonon resonances can be observed by the sharp peak in the imaginary part of permittivity. Figure 3.1(b) shows the real and imaginary parts of the dielectric constant as a function of carrier density (N) in semiconductor at frequency of 10.5 THz.

ϵ_0	Vacuum Permittivity
ϵ_s	Static dielectric constant
e	Electron charge
ω_{LO}	Longitudinal optical phonon resonance
ω_{TO}	Transverse optical phonon resonance
Γ	Free carrier coherent decay factor
m_e	Electron effective mass
γ	Phonon damping constant
N	Free carrier density

Table 3.1: Variables in modified Drude dielectric constant model

Kramers-Kronig relationship dictates coupled evolution of the real and imaginary parts of the dielectric constant. Then a change in absorption must be accompanied by the shift in phase accumulation or real part. In Figure 3.1, it is shown that by increasing the carrier density, the real part decreases and the imaginary part increases. In other words, higher carrier density results in higher loss. In this paper, the carrier density for the doped region is set to be $N = 2 \times 10^{17}\ Cm^{-3}$ and the corresponding

permittivity is $16.69 + i4.67$. As can be seen in Figure 3.1(a), there is an abrupt change in the real part of permittivity around 8.0 THz. Our operational frequency is set around 10.5 THz where the real and imaginary part of permittivity shows milder change versus frequency. The calculated permittivity at $10.5\ THz$ is $8.01 + i0.05$. There are other materials that can be used as a substitution for GaAs, such as InSb or Si. However, GaAs is preferable because of its low intrinsic free carrier density and higher carrier mobility compared to other mentioned choices.
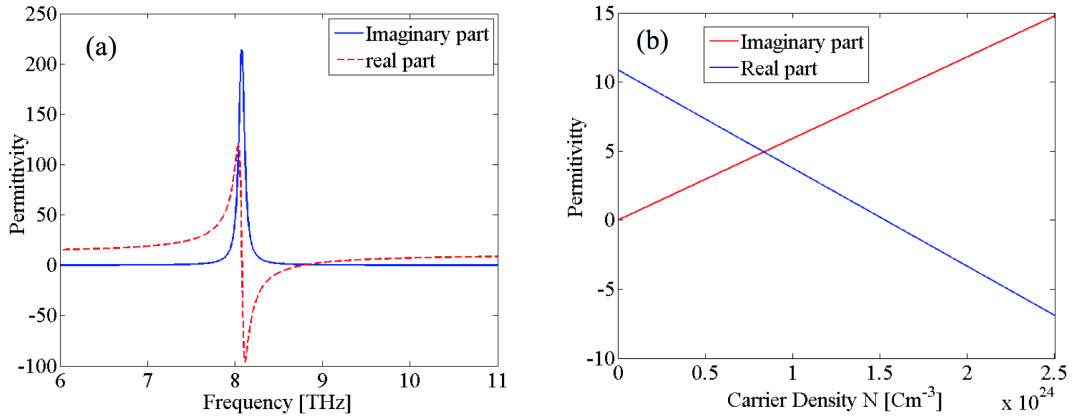
Figure 3.1: Real and imaginary part of GaAs permittivity as a function of frequency for free carrier density of $N = 2 \times 10^{17}\ Cm^{-3}$(b) Real and imaginary part of permittivity as a function of free carrier density at frequency of $10\ THz$.

Enhancement and depletion modes are known as a working mode based on injection and depletion of free carriers in the doped semiconductor. These two modes are being used in this section and the following section to describe the THz switch states. Now, we focus on the waveguide-cavity-waveguide (WCW) structure with potential application as THz switch or filter. Figure 3.2(a) shows the schematic view of our proposed WCW THz switch, consisting of two parts: cavity and waveguide. The waveguide can be assumed as equally-spaced cylindrical resonators, which are placed along the cylindrical waveguide. Figure 3.2(b) illustrates the wave propagation mechanism in the WCW structure. As shown, the structure can be regarded as equally

spaced resonator array. When the resonant frequencies of both parts are the same, the EM wave can couple from the waveguide to cavity and vice versa. Then to obtain the highest transmission in the switch it is essential that ω_W and ω_c coincide. In the next part, we use a mathematical model to describe the power transmission in the proposed structure, and then we investigate the parameters that are taking effect in the power transmission characteristic.
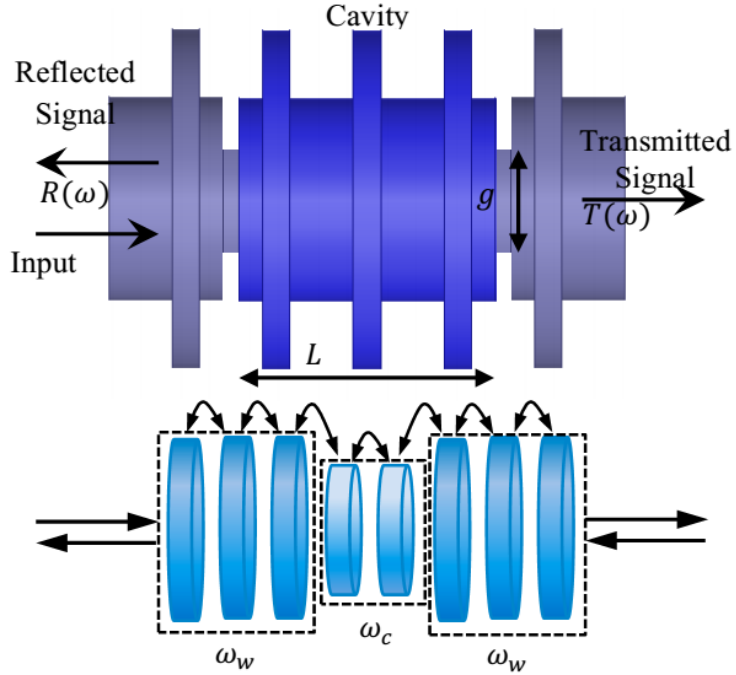
Figure 3.2: Schematic view of the THz waveguide-cavity-waveguide structure. (b) The THz waveguide and cavity can be assumed as equally spaced cylindrical resonators array. the coupling frequency for waveguide and cavity resonators are ω_W and ω_c respectively.

Using temporal coupled-wave analysis (TWCA), the transmission and the reflection of waveguide-cavity can be described as [65, 66]

$$T(\omega) = \frac{\Gamma_c^2}{(\omega - \omega_W)^2 + \Gamma_c^2} \tag{3.4a}$$

$$R(\omega) = \frac{(\omega - \omega_W)^2}{(\omega - \omega_W)^2 + \Gamma_c^2} \tag{3.4b}$$

And $Gamma_c$ can be described using:

$$\Gamma_c = \frac{\omega_c}{2Q} \tag{3.5}$$

In the Equations (3.4a) and (3.4b), the cavity decay rate (Γ_0) is assumed to be smaller than the cavity coupling ratio (Γ_c). This assumption is acceptable in our case as the loss is very small. The ω_c is the resonant frequency of the cavity that can be controlled by changing the grooves height or altering the refractive index inside the dielectric. The grooves height is predetermined and cannot be changed after design so the only option to tune the resonant frequency is changing the refractive index. In this design, when there is no stimuli and the operating frequency is far from cavitys resonant frequency compared to Γ_c , ($|\omega - \omega_c| >> \Gamma_c$), all the power reflects back and the switch is in the off-state. When the operation frequency is close to the cavitys resonant frequency ($|\omega - \omega_c| << \Gamma_c$), the transmission in Equation (3.4a) is approximately 1 and the switch is in the on-state. In order to introduce the parameters that can enhance the switching ratio we approximate Equation (3.5) as:

$$\Gamma_c = \frac{(1-R)V_g}{L_{cav}} \tag{3.6}$$

The Γ_c is described as a function of reflective coefficient R and V_g group velocity . Based on Equations (3.4a), (3.4b) and (3.5), to enhance the switching ratio we need to increase the reflective coefficient and decrease group velocity by employing slow waves. Then to achieve the high switching ratio, two main parameters of the cavity should be taken into account: the quality factor that is inversely proportional to cavity decay rate in Equation (3.6), and the effective volume V_{eff} that controls the cavitys photon intensity [67]. The proposed C-SSPP structure can support the slow waves that have

small group velocity. Additionally, the cavity can trap electromagnetic waves for a significant period of time, resulting in a high quality factor. Then based on what was discussed in the previous paragraph, this structure can have a high switching ratio. In our design, the cavity and waveguides portions are identical, but they are separated from the waveguide through inserting a circular iris between the waveguides and the cavity. If there is no iris between the cavity and waveguides, the structure acts like a band reject filter. However, when inserting the iris between the waveguide and cavity it acts as a band pass filter. By changing the iris radius, we can adjust the passing bandwidth. In other words, inserting the iris and changing its radius alter the effective volume and, as a result, quality factor and cavitys bandwidth change. The simulations show that by decreasing the iris radius the bandwidth is also reduced. It is noteworthy that the relative bandwidth in the switch with longer cavity lengths is bigger due to the higher loss.

3.2   Depletion mode performance

By tuning the waveguide-cavity coupling ratio the power transmission can be adjusted. Based on Equation (3.5), the Γ_c is a function of the cavity resonant frequency. Utilizing the depletion mode to change the dielectric refractive index inside the cavity, the resonant frequency can be altered. As the cavity quality factor is high, the small change in refractive index can change the resonance frequency such that the WCW switches from one state to another state.

Figure 3.3 shows the power transmission for two different refractive indices inside the cavity. In this plot, the GaAs refractive index is assumed to be constant over the entire cavity. The cavity length is set to be 3 periods to increase the interaction of electromagnetic waves with the refractive index inside the cavity. By changing the real part of permittivity from 8.05 to 8.1 the resonant frequency shifts from 10.72 THz to 10.78 THz. In principle, as permittivity increases, the resonant frequency of

34
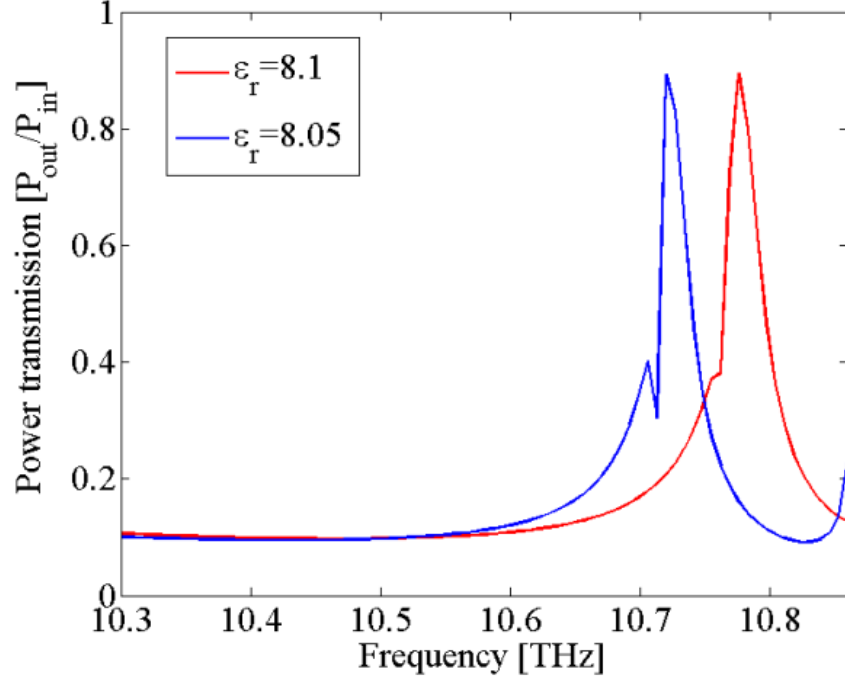
Figure 3.3: Power transmission versus frequency for different values of GaAs permittivity.

the cavity shifts to lower frequencies. Likewise, when the permittivity decreases the resonant frequency shifts to higher frequencies. Due to technological constraints, it is not practical to alter the refractive index value in the entire cavity. As mentioned earlier by setting the operating frequency near the grooves resonant frequency most of the electromagnetic (EM) power concentrates inside the grooves. Then by changing the refractive index in a portion of the grooves cavity, it is possible to control the flow of electromagnetic waves.

In the final design, the free carrier concentration of GaAs inside the grooves cavity is set to $N = 2 \times 10^{16}$ Cm^{-3} Since the doping concentration is higher than its intrinsic carrier density ($N = 2 \times 10^{6}$ Cm^{-3}), we can utilize the depletion mode in our structure. Where the metal electrode in the cylindrical resonator and the GaAs dielectric contact, a Schottky contact is formed. By applying a voltage to the electrodes the depletion zone below the metals will appear. The depletion thickness can be calculated using [64]

$$D_{depletion} = \sqrt{\frac{2\epsilon_s \epsilon_0 (V_{bi} + V)}{eN}} \qquad (3.7)$$

In which, V is the applied voltage to the patches and V_{bi} is the built-in voltage of semiconductor metal junction. Other variables are described in table. I. For the GaAs-metal junction the $V_{bi} = 0.75\ V$.
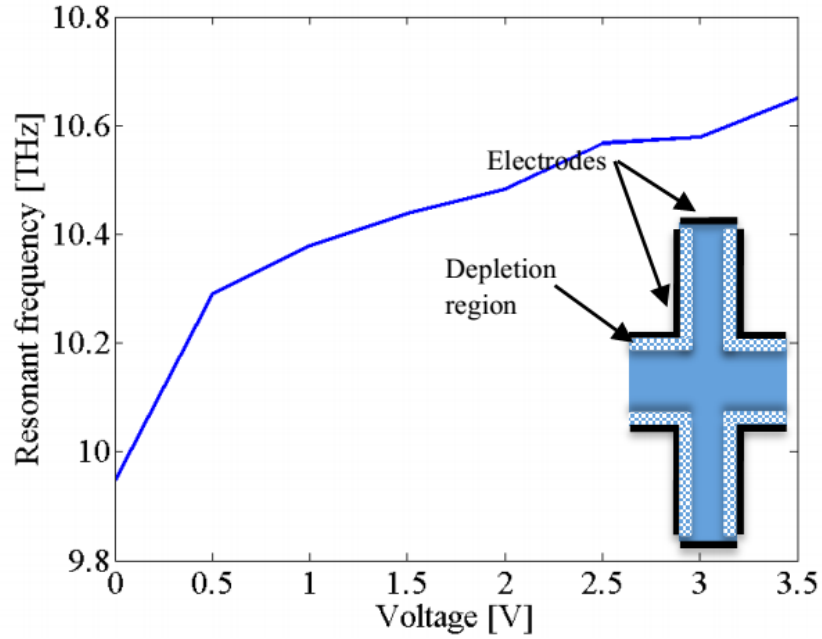
Figure 3.4: Resonant frequency of cavity versus the applying voltage across the metal contact. The figure in the inset shows how the electrodes are connected to the cavity.

By changing the voltage across the electrodes, the depletion depth will be formed and the effective permittivity of GaAs can be tuned. The switch state can alter from on to off and vice versa by controlling the depletion region in a layer of GaAs that is thin relative to the grooves width. Figure 3.4 shows the resonant frequency versus different voltages. The permittivity of the depletion region can be calculated setting $N = 0$ in Equation (3.3). This results in $\epsilon = 8.051 + i0.05$ which is close to the intrinsic value of permittivity with $N = 2 \times 10^6\ Cm^{-3}$. By increasing the voltage,

the depth of the depletion region increases, which leads to a decrease in the effective permittivity of the dielectric inside the cavity. As mentioned earlier, decrease in permittivity will shift the resonant frequency to higher. Figure 3.5 shows the power transmission for two different voltages across the metal contacts and electric field magnitude at two different frequencies when the voltage is set to be V=2 V. As depicted in Figure 3.5(b), when the operating frequency is at 10.58 THz the power transmission has its maximum value and the electric fields concentration is maximum inside the grooves. By increasing or decreasing the frequency from 10.58 THz the power transmission is reduced. Figure 3.5(c) shows the electric fields magnitude at 10.59 THz. As can be seen, the electric fields are weaker in the cavity.
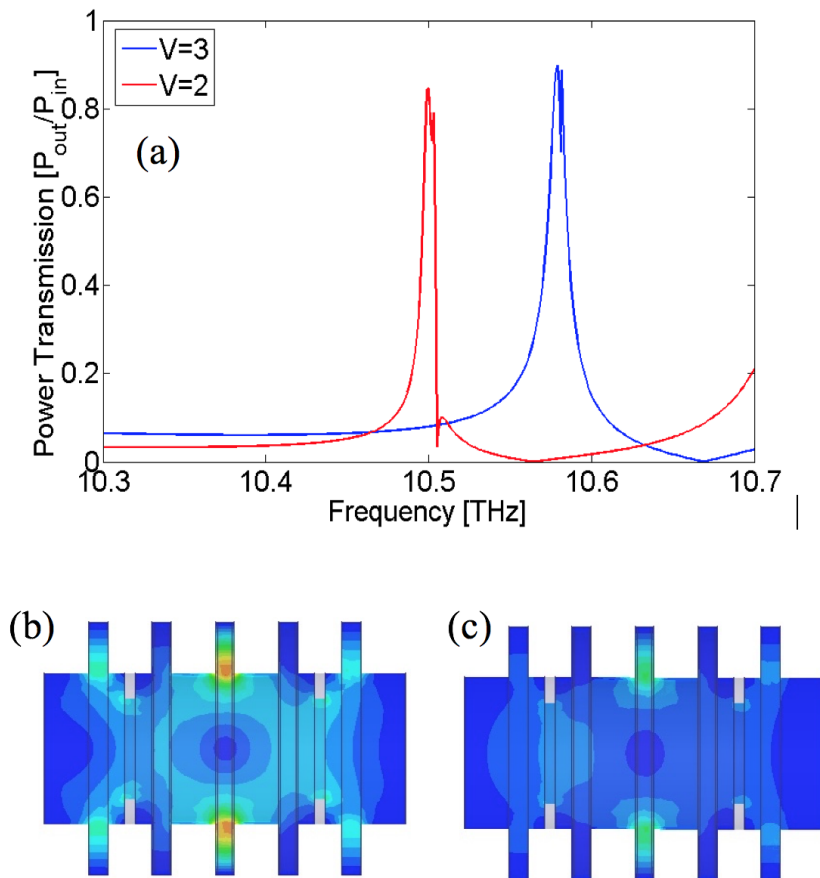
Figure 3.5: (a) Power transmission at two different voltages. (b) Electric field magnitude at 10.58 THz (c) Electric field magnitude at 10.59 THz.

CHAPTER IV

Analog to Digital Converter Using Single Sided Corrugated Waveguide

Exponential growth of information technology markets feeds the need for higher sample rate for the communication systems. This leads to ultra-high-speed analog-to-digital (ADC) converters as an incumbent part of communications systems. The ADCs based on the spatial detection have been widely used by numerous optical designers throughout the literature [68, 69, 2]. The key mechanism behind spatial detection is the deflection of output signal at different angles with changing analog input. In order to realize this functionality, spoofed surface plasmon polariton (SSPP) architecture is employed. Such structure features SSPP mode with a slow-wave nature and strong field confinement. These properties are not only critical to the THz signal transmission over distance, but are also the key for localized modulation of the THz signals with enhanced efficiency. We show that the phase constant of the 1D-SSPP is sensitive enough to the refractive index of the material inside the grooves. Then using the plasmonic behavior of the 1D-SSPP dispersion diagram and its sensitivity to the refractive index inside the grooves, we show that one can reach beam steering around 42 degrees in a short waveguide. Figure 4.1 shows the schematic view of the single sided SSPP structure. It consists of metallic corrugated layer covered by a layer of dielectric.
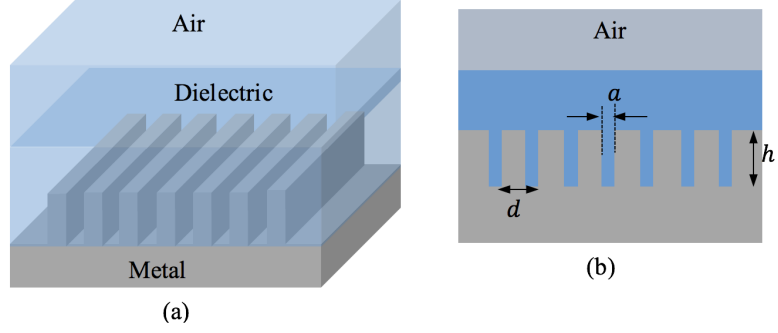
Figure 4.1: (a) Schematic view of the 1D SSPP (b) Cross section of the 1D waveguide.

The dispersion equation of an SSPP waveguide embedded into a dielectric with index can be written as [70]

$$PX(P,\beta)tan(Ph) = 1 \tag{4.1}$$

where in the 2D limit $P = \omega n/c$ and $X(P,\beta) = \sum_{m=-M}^{m=M} S_m^2/k^m$ with $S_m^2 = sinc(Q^m a/2)a/d$ and $k^m = \sqrt{(\beta + 2\pi m/d)^2 - P^2}$, where we have taken into account that outside of the grooves we have attenuated field. These expressions are valid in slightly more general case of structures with finite width , in which case we have $P^2 = (\omega n/c)^2 - (\pi/W)^2$, but we will stick to the 2D limit. We consider two limiting cases: near zero frequency, where the dispersion curve goes close to the light-line, and near the SSPP plasma frequency, where the curve is far from the light-line.

The first situation takes place when $\beta h << \pi/2$ and we can approximate $P \ \beta - \delta$. In this case it is sufficient to leave only $m = 0$ term in the expression for $X(P,\beta)$ and we obtain

$$P = \beta(1 - S^4 \frac{h^2 \beta^2}{2}) \tag{4.2}$$

39

In the opposite case, we take $P = P_p - \delta$, where $P_p = \pi/2h$ determines the plasma frequency (reached asymptotically in the limit $h/d \gg 1$. Then, we find

$$P = P_p(1 - \frac{X(P_p, \beta)}{h})$$ (4.3)

Here, retaining only the zeroth term is not that well justified, especially if β is too close to the boundary of the Brillouin zone β/d. If, nevertheless, we make this approximation, we obtain

$$P = P_p(1 - \frac{S^2}{\sqrt{h^2\beta^2 - (\pi/2)^2}})$$ (4.4)

We can use this equation for finding the variation of β when the refractive index of the dielectric changes, while frequency remains fixed,

$$\beta(n) \frac{S^2h - 1}{1 - \omega n/P_p c}$$ (4.5)

This approximation is valid, when $\beta(n) < \pi/d$. Figure 4.2 shows the dispersion diagram using Equation (4.5) for different dielectric refractive indices. As can be seen, by altering the refractive index of dielectric over the corrugated structure the phase constant changes.

Figure 4.3 illustrates the magnitude of electric field disturbution along the structure. The operating frequency is chosen to be near the cavity resonant frequency and the magnitude of E-field are ploted in the cross section of the structure. As can be seen we have high concentration of E-filed inside the grooves.

We have shown the single sided corrugated structure can support SSPP and has

40
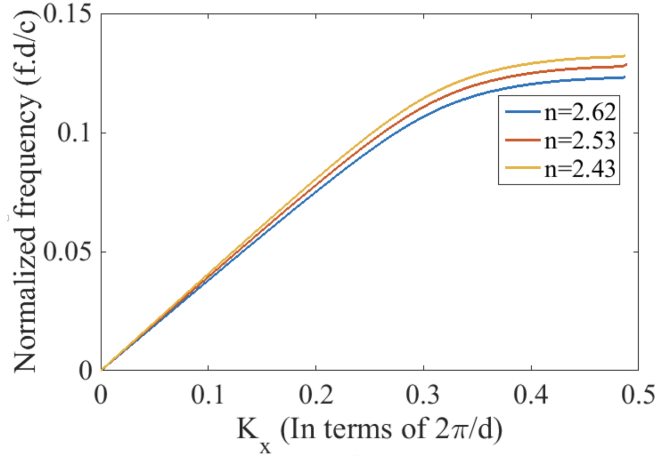
Figure 4.2: Dispersion diagram of the sample 1D SSPP waveguide. Dimensions are $d = 50 \ \mu m, h = 40 \ \mu m, a = 5 \ \mu m$
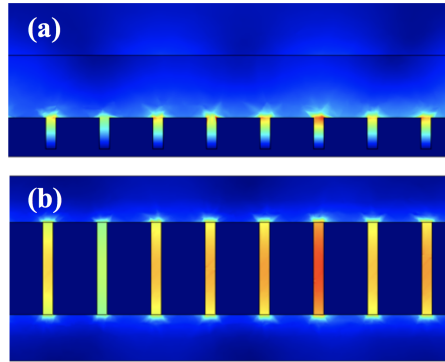
Figure 4.3: E-field disturbution along the structure at two different frequencies, (a) at 100 GHz (b) at 600 GHz.

strong field confinement inside the grooves. Figure 4.4 shows the schematic view of the proposed ADC. The ADC has two arms, grooves inside the arms are filled by doped semiconductor, by implementing Schottky affect we can tune the output pattern at the end stage of the two arms. In Figure 4.4, over the corrugated metallic surface is covered by the dielectric layer and over the dielectric is free space. It is also possible to cover the upper layer with a thin layer of metal. This will reduce the height of the structure. This will require revision of the Equation (4.5) to find the dispersion diagram.

The above structure has three stages, beam splitter, two corrugated arms and
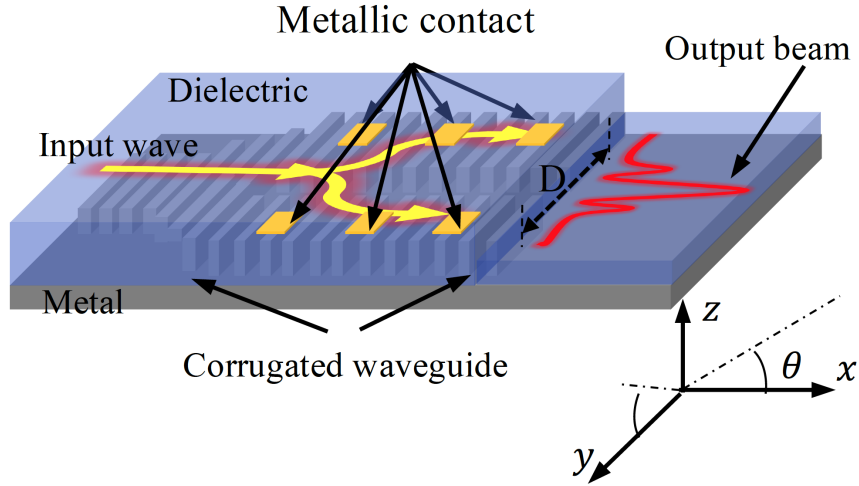
Figure 4.4: Schematic view of ADC using 1D corrugated SSPP waveguide.

detectors. As to make the simulations faster and easier in HFSS the beam splitter is eliminated but the two arms are excited with same phase and amplitude signal. Figure 4.5 shows the simulated structure in HFSS.
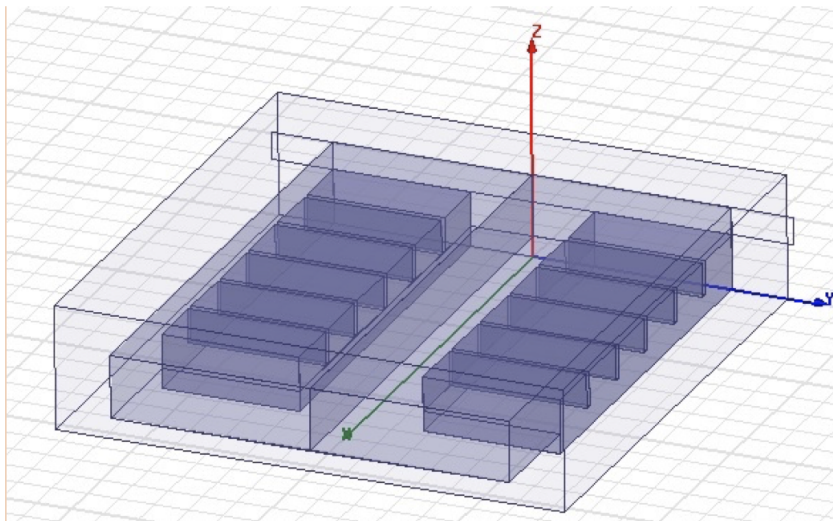
Figure 4.5: Schematic view of MZI in HFSS.

Each arm acts as an antenna, then in our structure we have antenna array with two elements. With the beam steering stage comprising a two-arm Mach-Zehnder Interferometer (MZI) structure, the main lobe of the far-field radiation pattern is rather broad. As mentioned before, the low quality factor of this spatial maximum

42

poses challenges to realizing higher bit resolution, for which reason the detector array operating at designated gain and saturation power needs to be adopted. In order to further boost the bit-depth of the ADC, we plan to experiment on different approaches. One approach, for example, is to incorporate more phase shifting arms into the beam steering stage, which will generate narrower radiation maxima. For the purpose of comparison, the structure has been simulated for two different values of refractive index. The radiation pattern has been shown in Figure 4.6. As can be seen the new structure has sharper radiation pattern compare to the previous design [71]. By changing the refractive index from 1 to 1.15 a deflection angle of around 15 degrees has been illustrated. The frequency of operation is set to be around 1.190 THz, which can be scaled to lower and higher frequencies.

The material to control the deflection angle of radiation pattern like the previous design is GaAs. The real value of refractive index at the operation frequency of 10 THz is 6.91. By using the depletion mode, we can reduce the refractive index and control the angle of radiation peak. Figure 4.7 shows the simulation result for two different values of refractive indices. As seen by changing the refractive index from 6.91 to 6 the deflection angle of around 30 degrees can be observed.

4.1 Calculating the radiation pattern of rectangular array waveguides

First we try to calculate the radiation pattern for our DC-SSPP structure, after that we will use the same method to calculate the radiation pattern for our new ADC.

We can assume each arm as a rectangular aperture that acting as an antenna. The dominant modes for this antenna is TE_{10} the fields in the far field can be calculated using [72]
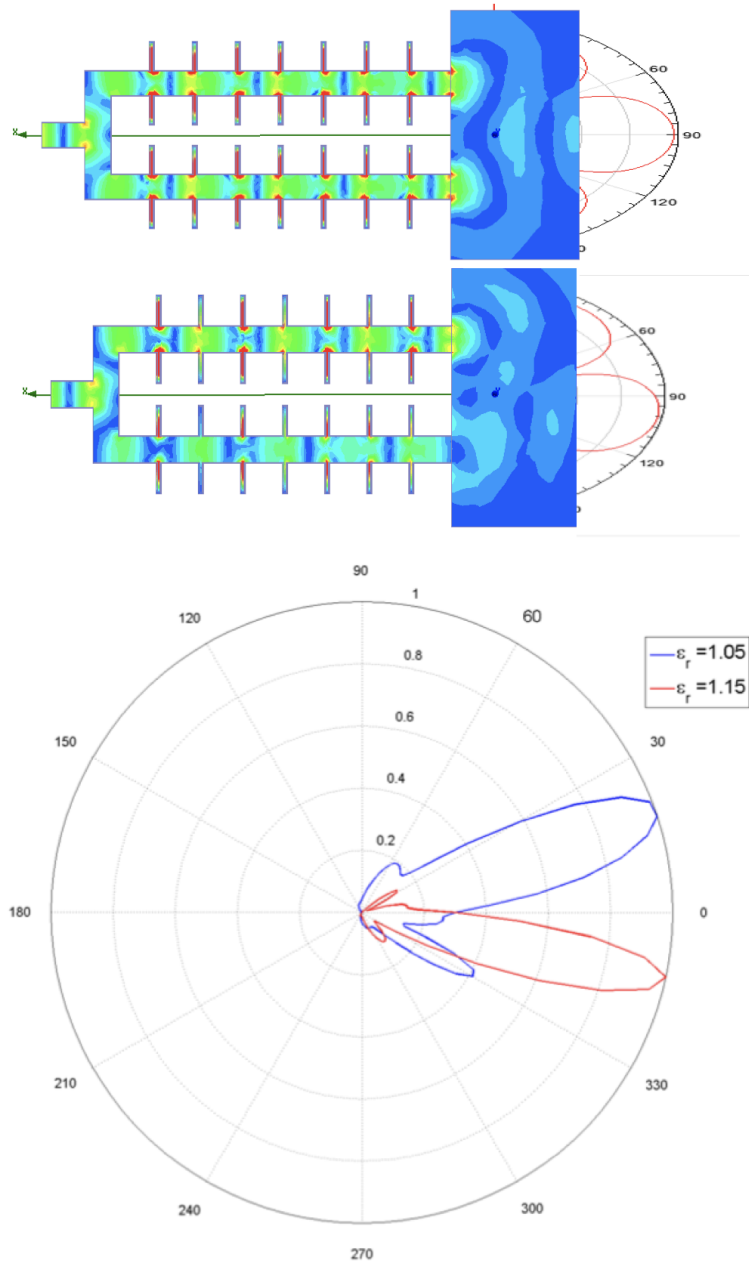
Figure 4.6: Radiation pattern (Power) for comparison with older design.

$$E_y = E_0 cos(\frac{\pi x}{z}) \tag{4.6a}$$

$$H_x = E_0 \frac{\epsilon}{\mu} cos(\frac{\pi x}{z}) \tag{4.6b}$$

$$E_\theta = ik\frac{e^{-ikr}}{2\pi r} A f_y(\theta, \phi) sin(\phi) \tag{4.6c}$$

$$E_\phi = ik\frac{e^{-ikr}}{2\pi r} B f_y(\theta, \phi) cos(\phi) \tag{4.6d}$$
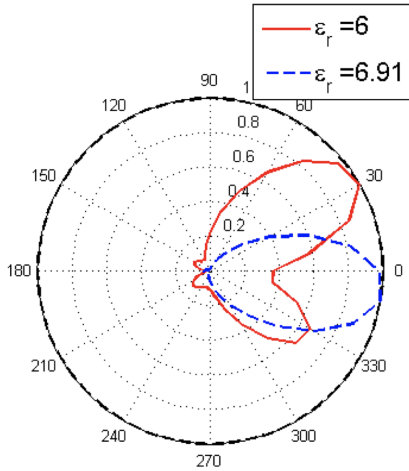
Figure 4.7: Radiation pattern (Electric field) for two different values of dielectric constant in one of the arm.
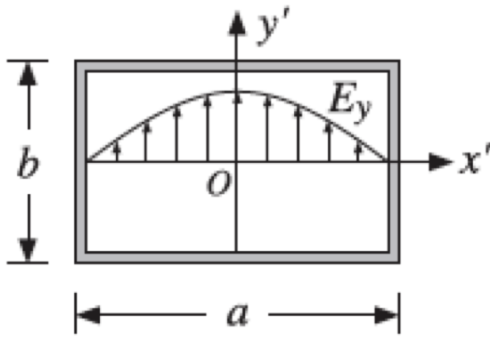
Figure 4.8: Electric field over waveguide aperture.

Where the $f_y(\theta, \phi)$ is the aperture Fourier transform of electric field:

$$f_y(\theta, \phi) = \int\limits_{-a/2}^{a/2} \int\limits_{-b/2}^{b/2} E(x', y') e^{ik_x x' + ik_y y'} dx' dy' \qquad (4.7)$$

Using the electric field for the lowest order modes in rectangular waveguide we

45

will have the far field fields as follows:

$$E_\theta = Asin(\phi)\frac{cos(X)}{X^2 - \frac{\pi}{2}^2}\frac{sinY}{Y} \tag{4.8a}$$

$$H_\phi = Asin(\theta)cos(\phi)\frac{cos(X)}{X^2 - \frac{\pi}{2}^2}\frac{sinY}{Y} \tag{4.8b}$$

$$X = \frac{ka}{2}sin(\theta)cos(\phi) \tag{4.8c}$$

$$Y = \frac{ka}{2}sin(\theta)sin(\phi) \tag{4.8d}$$

In which, A is a constant, a and b are dimensions of the aperture and k is the wavenumber. Those equations are for a single aperture antenna, but if we have more arms the final pattern can be found using linear array formula, the array factor is as follow:

$$AF = [\frac{sin(N\phi/2)}{sin(\phi/2)}] \approx Nsinc(N\phi/2), \ \phi = kdcos(\theta + \beta) \tag{4.9}$$

Where, d is the distance between arms and β is phase difference between each arm. Figure 4.9 shows the radiated fields in H-plane where $\phi = 0$. They show by increasing the number of arrays and also by increasing the waveguide dimensions we can achieve higher directivity. The higher directivity means the array factor will have a sharper peak at $\psi = 0$ and the ADCs bit resolution will increase. Increasing the arms make the design much complicated in the ADC. Then in our design we set the number of arms to 2 but we set the waveguide dimensions as big as possible.
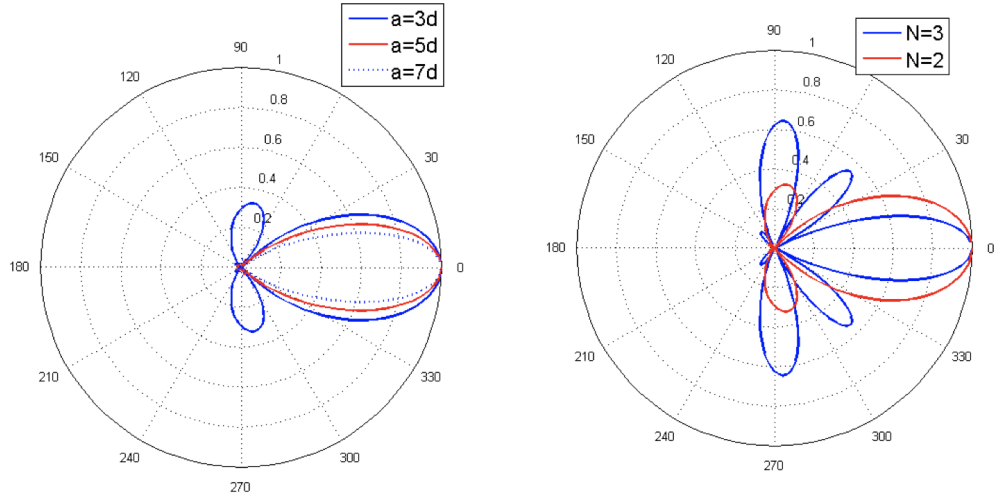
Figure 4.9: Radiation field for two and three arms (b) radiation field for different waveguide dimensions.

4.2 Radiation pattern for rectangular dielectric aperture antenna

For a dielectric slab waveguide with dimensions and in free space the electric field distribution can be approximated as:

$$
E_y = \begin{cases} cos(k_x x)cos(k_y y) & |y| < b, \ |x| < a \\ e^{-\alpha_y|y|}e^{-\alpha_x|x|} & otherwise \end{cases} \tag{4.10}
$$

where:

$$
k_{x,y} = \sqrt{(\omega\mu\epsilon)^2 - k_z^2} \tag{4.11a}
$$

$$
\alpha_{x,y} = \sqrt{k_z^2 - (\omega\mu\epsilon)^2} \tag{4.11b}
$$

Using the above equation, the Fourier transform of electric field for the aperture will

47

be derived as:

$$f_y(\theta, \phi) = \int\limits_{-\infty}^{\infty} \int\limits_{-\infty}^{\infty} E(x', y') e^{ik_x x' + ik_y y'} dx' dy'$$

$$= \int\limits_{-\infty}^{\infty} e^{ik_y y'} e^{-\alpha_y |y'|} cos(k_y y') dy' (\int\limits_{-\infty}^{-a} e^{\alpha_x x} e^{ik_x x'} dx' +$$

$$\int\limits_{-a}^{a} cos(k_x x') e^{k_x x'} dx' + \int\limits_{a}^{\infty} e^{-\alpha_x x'} e^{ik_x x'} dx') \qquad (4.12)$$

$$f_y(\theta, \phi) = (\frac{cos(X)}{X^2 - \frac{\pi^2}{2}} - 2e^{-\alpha_x x} \frac{\alpha_x cos(X) - k_x sin(X)}{k_x^2 + \alpha_x^2})$$

$$(\frac{cos(Y)}{Y^2 - \frac{\pi^2}{2}} - 2e^{-\alpha_y y} \frac{\alpha_y cos(Y) - k_y sin(Y)}{k_y^2 + \alpha_y^2}) \qquad (4.13)$$

In above equations if we design the structure in a way that the fields outside the slab damp quickly, we can make the final equation simpler by increasing the value of α_x and α_y to infinity. Then the final equation would be as follow:

$$E_\theta = ik \frac{e^{-ikr}}{2\pi r} (\frac{1 + cos(\theta)}{2} sin(\phi) \frac{cos(X)}{X^2 - \frac{\pi^2}{2}} \frac{cos(Y)}{Y^2 - \frac{\pi^2}{2}} \qquad (4.14a)$$

$$E_{total} = ik \frac{e^{-ikr}}{2\pi r} (\frac{1 + cos(\theta)}{2} sin(\phi) \frac{cos(X)}{X^2 - \frac{\pi^2}{2}} \frac{cos(Y)}{Y^2 - \frac{\pi^2}{2}}$$

$$2sinc(kdcos(\theta) + \beta) \qquad (4.14b)$$

Equation (4.14b) show it is possible to have a sharper peak by increasing the dimensions of waveguides. But dimensions are not the only factors that play a significant role in the beam width of MZI. To have the optimum dimensions for smaller beam width series of simulations have been done. Figure 4.10(a) shows the radiation pat-

48

tern for a single arm waveguide. Simulation shows the waveguide width does not have a significant effect on the beam width. Adding second arms to the structure and making a MZI structure we will have smaller beam width (see Figure 4.10(b)) and by increasing the waveguide width the beam width decreases. Figure 4.10(b) shows we have the smallest beam width at the frequency of 430 GHz with the waveguide width of 240 μm .
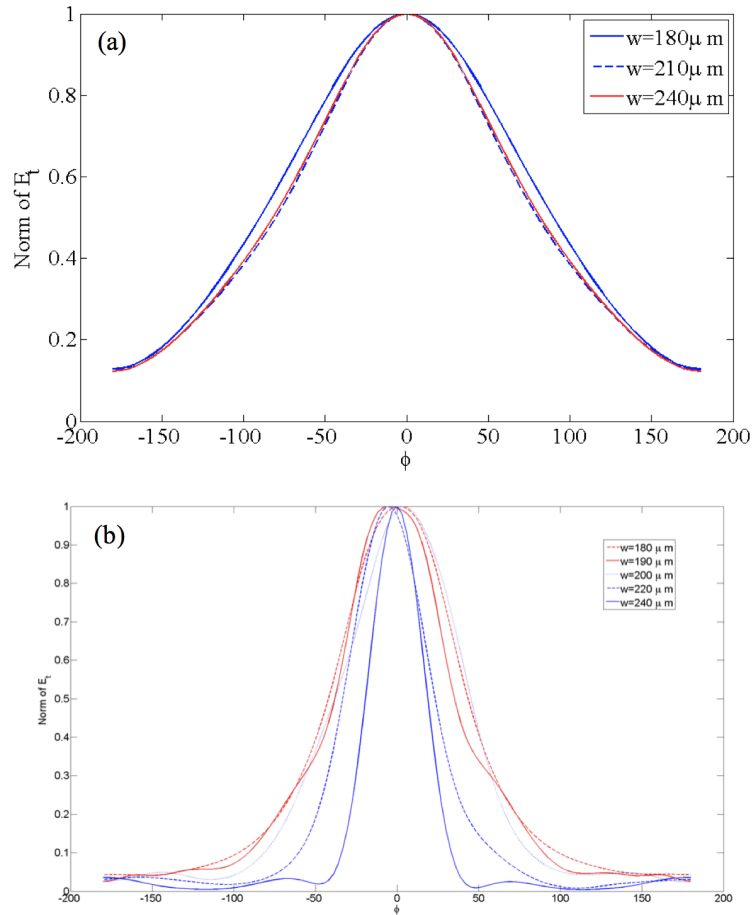
Figure 4.10: Radiation pattern for single arm with different waveguide width. (b) Radiation pattern for MZI structure with different waveguide width.

4.3 Phase difference calculation and circuit model

Using Equation (4.7), the phase difference between arms of length filled with dielectrics characterized by different refractive indices n_1 and n_2 can be found as

$$\Delta\phi(n_2, n_1) = (\beta(n_2) - \beta(n_1))l = S^2 \frac{l\omega}{hP_pc} \frac{n_2 - n_1}{(1 - \frac{\omega n_2}{P_pc})(1 - \frac{\omega n_1}{P_pc})} \tag{4.15}$$

We find the effective refractive index of the groove with depleted layers at the edges by regarding it as a three-layer waveguide and applying the transfer matrix approach. The electric field is presented within a layer as
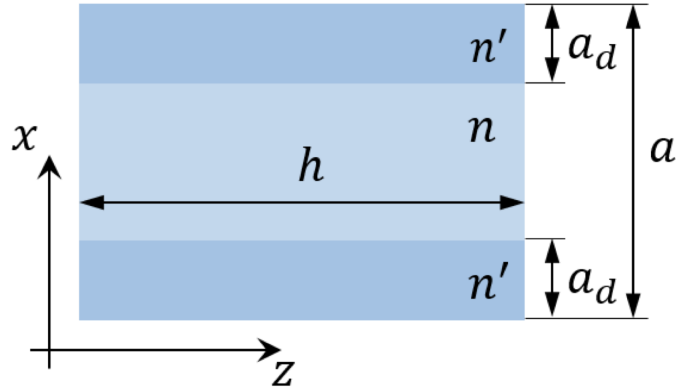
Figure 4.11: Cross section view of one groove, depletion layer has thickness of a_d and its refractive index is n'.

$$E_x(x, z) = pe^{ipz}(A^+(x)e^{iq(z)x} + A^-(x)e^{-iq(z)x}) \tag{4.16a}$$

$$E_z(x, z) = -q(x)e^{ipz}(A^+(x)e^{iq(z)x} - A^-(x)e^{-iq(z)x}) \tag{4.16b}$$

where $q(x) = \sqrt{P^2(x) - p^2}$ and $P(x)$ is given by the same expression as above $P(x) = \omega n(x)/c$. Since we consider homogeneous layers, it is sufficient to distinguish them by the refractive index and thus introduce $q(n) = \sqrt{\omega n/c^2 - p^2}$. The effective refractive

index can be defined as $p = \omega n_{eff}/c$, because it will define the variation of the field phase inside the groove, $\phi = ph$, which determines how close the frequency is to the plasma frequency.

Propagation across a layer is taken into account by the layer transfer matrix

$$E_x(x, z) = pe^{ipz}(A^+(x)e^{iq(z)x} + A^-(x)e^{-iq(z)x}) \tag{4.17a}$$

$$E_z(x, z) = -q(x)e^{ipz}(A^+(x)e^{iq(z)x} - A^-(x)e^{-iq(z)x}) \tag{4.17b}$$

where $\chi(n') = q(n')a_d$ and $\chi(n) = q(n)(a - 2a_d)$ inside the depleted and normal layers, respectively. The transfer from n' layer to n layer is described by the interface transfer matrix

$$E_x(x, z) = pe^{ipz}(A^+(x)e^{iq(z)x} + A^-(x)e^{-iq(z)x}) \tag{4.18a}$$

$$E_z(x, z) = -q(x)e^{ipz}(A^+(x)e^{iq(z)x} - A^-(x)e^{-iq(z)x}) \tag{4.18b}$$

where $t_1 = n'^2/n^2$ and $t_2 = q(n')/q(n)$. Thus, the total transfer matrix is

$$T_{tot} = T(n')T(n', n)T(n)T(n, n')T(n') \tag{4.19}$$

where $T(n', n) = T^{-1}(n, n')$. At the boundaries of the groove E_x must vanish and, hence, we must have where $|\pm x\rangle = (\sqrt{(1, \pm 1)^T})/\sqrt{2}$. In other words, the correct transfer matrix across the whole groove must map $|x\rangle$ into vector orthogonal to $|-x\rangle$. This yields the dispersion equation in the form $\langle x| T_{total} |x\rangle$. Performing vector calculations in this formula we obtain

$$D(\omega) = sin(2\chi(n') + \chi(n)) + 2\eta sin(\chi(n'))cos(\chi(n) + \chi(n')) - \eta^2 sin^2(\chi(n'))sin(\chi))$$

$$(4.20)$$

where $\eta = t_2/t_1 - 1$. We take into account that $\omega na/c << 1$ and hence $q(n)$ and $q(n')$ are small comparing to $1/a$. Thus both phases $\chi(n)$ and $\chi(n')$ are small and we can take the lowest non-vanishing approximation: $D \approx \chi(n) + 2\chi(n')t_2/t_1$. Now, the equation $D = 0$ is easy to solve

$$p^2 = \frac{\omega n}{c}^2 \frac{1}{1 - f(1 - n^2/n'^2)} \qquad (4.21)$$

where $f = 2a_d/a$. Thus, we find the effective refractive index

$$n_{eff} = \frac{nn'}{\sqrt{n'^2(1 - f) + fn^2}} \qquad (4.22)$$

In the depletion mode of operation of our ADC design, the phase change is induced by the variation of the depletion thickness in the groove regions. Based on Equation (3.7), the thickness of the space-charge region is a function of the applied voltage:

$$a_d = D_{depletion} = \sqrt{\frac{2\epsilon_s\epsilon_0(V_{bi} + V)}{eN}} \qquad (4.23)$$

There are two sources for the nonlinearity in our ADC design. One is the inverse cosine relation between angle maximum radiation and phase difference; the other is the nonlinearity of the Equation (4.23). The effect of first source is negligible for

small value of phase difference. To overcome the nonlinearity effect of second source, one way is changing the method that control the refractive index and finding some material that the relation between its refractive index and external stimuli is linear. The other way can be implementing the differential voltage, and applying voltage to both arms. The phase difference between MZI arms can be calculated as:

$$\Delta\phi_{V_1,V_2} = \frac{2\pi}{\lambda_0} \frac{n_i - n_d}{D_t otal} \sqrt{\frac{2\epsilon_s\epsilon_0}{eN}} (\sqrt{V_{bi} + V_2} - \sqrt{V_{bi} + V_1}) \qquad (4.24)$$

By inserting the voltage to both arms the nonlinearity between the input stimuli and output phase will reduce.
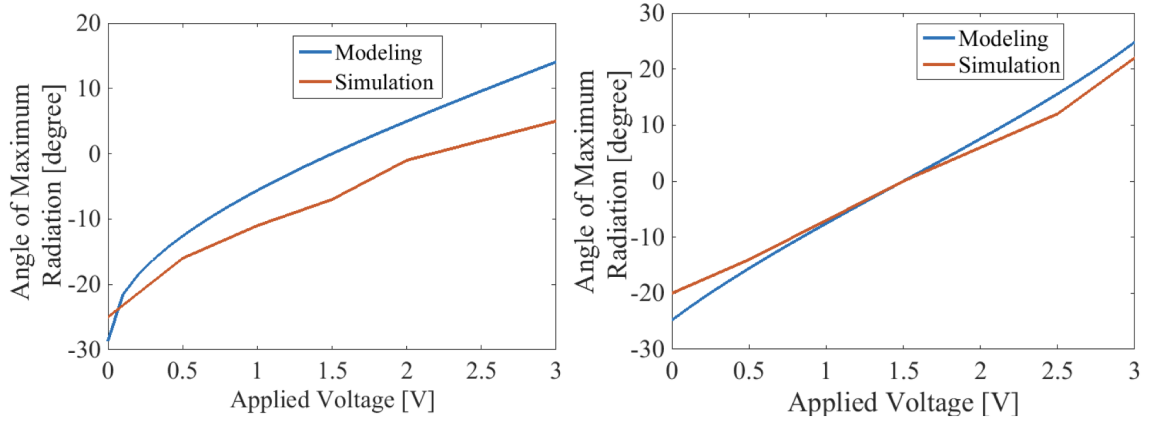
Figure 4.12: (a) Angle of maximum radiation versus input voltage in case of one arm excitation. (b) Angle of maximum radiation versus input voltage in differential mode

Using Taylor expansion and expanding the Equation (4.23) the phase difference can be found as:

$$\Delta\phi_{V_1,V_2} = \frac{2\pi}{\lambda_0}\sqrt{\frac{2\epsilon_s\epsilon_0}{eN}}l[a_1V_1 + b_1] \tag{4.25a}$$

$$a_1 = (-1 + \frac{V_m}{4} + \frac{V_{bi}}{2}) \tag{4.25b}$$

$$b_1 = (\frac{V_m}{2} - \frac{V_m^2}{8} - \frac{V_{bi}V_m}{4}) \tag{4.25c}$$

Where V_m is $V_1 + V_2$. As can be seen, the new equation shows linear relation between input voltage and the phase change. It is worth to notice, that the higher terms in Taylor expansion are omitted due the negligibility to first two terms. Figure 4.12(b) shows the angle of maximum radiation versus input voltage for two arms excitation. The dimensions for the design are as follows:$a = 0.65\ \mu m, W = 6.80\ \mu m, D = 15\ \mu m, d = 3.4\ \mu m, h = 2.2\ \mu m$. Figure 4.13(a) shows the normalized directivity for the ADC with differential excitation versus different applied voltages. As seen by swiping the voltage from 0 v to 3 v the maximum angle sweep of about 42 degrees is achievable. Figure 4.13(b) illustrates electric field distributions for three different applied voltages.
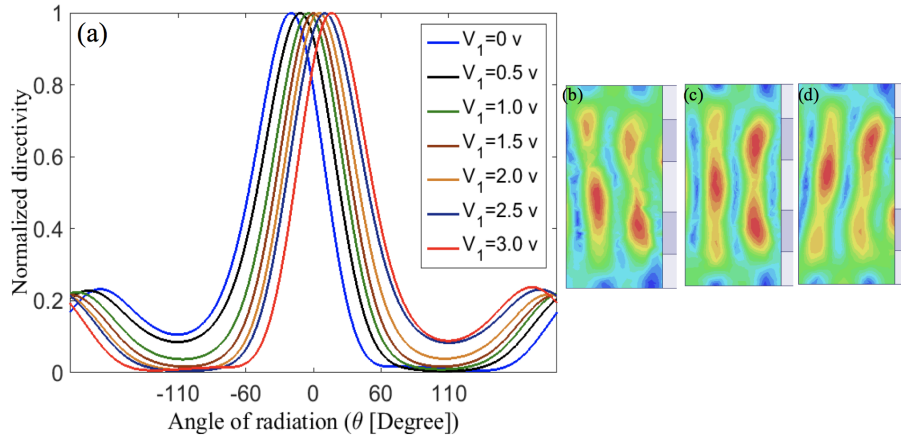
Figure 4.13: (a) Normalized directivity for different applied voltages. Electric field distribution at three different voltages (b) V=0 V. (c) V=1.5 V. (d) V=3 V.

The Schottky contact that formed by the metal electrode and the doped GaAs acts as the main contributor to a settling or delay time of the phase modulator. To find the final formula for bandwidth we start with the angle of maximum radiation versus time. For an end-fire array antenna the angle that maximum radiation occurs can be calculated using the following equation:

$$\theta_n = cos^{-1}(\frac{\lambda}{2\pi D}(-\Delta\phi_{V_1,V_2})) \qquad (4.26)$$

Substituting the phase difference from Equation (4.25a) in Equation (4.26) and inserting the transient time into the account the angle of maximum radiation versus time can be found as follows:

$$\theta_n = cos^{-1}(\frac{\lambda}{2\pi D}(a_1V_1 + b_1)(1 - e^{-t/T})) \qquad (4.27)$$

doing some algebraic manipulation, the upper limit for ADC BW can be found as follows:

$$BW < \frac{1}{2TLn(b+1)} \qquad (4.28)$$

As seen, for a fixed value of maximum applied voltage by increasing the number of bit the required sampling bandwidth reduces. To calculate this value for our designed ADC we need to find the settling time. The settling time can be combination of two different processes: carrier transition time and the RC time constant. For a very thin layer of dielectric in Schottky diode, when the induced electric field is strong, the transition time can be estimated using the simple formula: $\tau = d/V_{sat}$, where

is the carrier displacement. The thickness of depletion is around 200nm and the saturation drift velocity is $V_{sat} = 8 \times 10^8 \ m/s$ the transient time will be around 2.5 ps. By reducing the doped region thickness the settling time reduces. Unfortunately, it is not possible to reduce the doped region as in this case we need to reduces the maximum voltage and finally it reduces the sweep range of output pattern. The other factor is the delay time caused by RC value of the structure. Now we need to calculate the RC value of the 1D-SSPP waveguide. In this case one unit cell of the structure is investigated. Figure 4.14 shows the circuit model of a single period of the SS-SSPP waveguide. Z_l and Z_g represent the conventional waveguide impedance that can be easily calculated using conventional formula for slab and metallic waveguides. Y_{groove} represents the admittance of the grooves than can be calculate using following equation [73, 74, 75]

$$Y_{groove} = i\omega C_g + \frac{1}{i\omega L_g} + Y_g \frac{Z_{Schottkey} + iZ_g tan(\beta_g l_g)}{Z_g + iZ_{Schottkey} tan(\beta_g l_g)} \qquad (4.29)$$
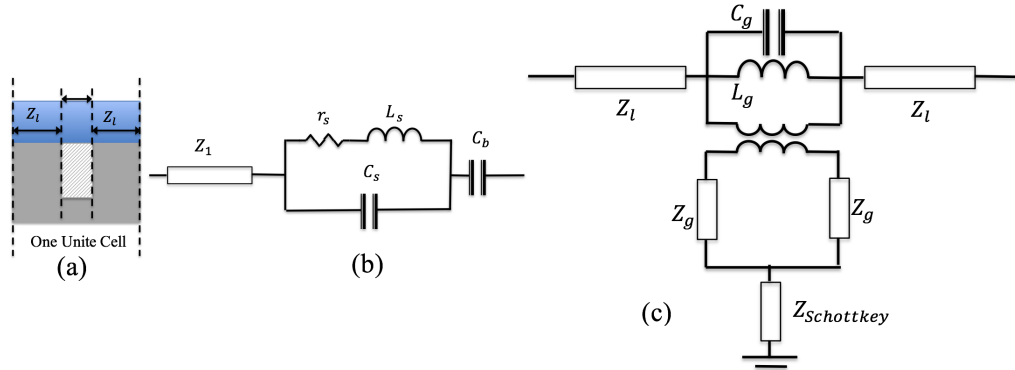
Figure 4.14: (a) Unit cell of 1D-SSPP waveguide. (b) Circuit model of Schottky diode. (c) Circuit model of single period of the waveguide.

Where Z_g is the characteristic impedance of the groove and l_g is groove length. Foe simplicity and as the value of C_g and L_g are smaller than the value of $Z_{Schottkey}$

56

they are neglected. And β_g is the propagation constant of EM wave inside the groove.

$$Z_g = Z_0 \frac{k_0}{\beta}, \ \beta_g = \sqrt{\omega^2 \mu \epsilon - (\frac{\pi}{W})^2} \tag{4.30}$$

Figure 4.14 (b) shows the circuit model of the Schottky diode. The values of circuit elements can be found using the following formulas [76, 77]

$$r_s = \frac{1}{4\sigma a}, \ L_s = r_s \frac{m_e \mu}{e}, \ C_s \frac{\epsilon_s \epsilon_0}{\mu_0} \tag{4.31a}$$

$$Z_1 = (\frac{Ln(b/a)}{2\pi}) \sqrt{[\frac{\sigma}{i\omega - (m_e\mu/e)\omega^2} + \frac{\epsilon_s \epsilon_0}{\mu_0}]} \tag{4.31b}$$

Where a and b are the dimensions of the contact, σ is the semiconductor DC conductivity. The C_b is the capacitance value of the Schottkey contact and can be found using the simple capacitance formula:

$$C_b = \epsilon_s \epsilon_0 \frac{A_{Contact}}{D_{Depletion}} \tag{4.32}$$

Where $A_{contact}$ is the surface area of Schottkey contact. Using the mentioned dimensions, the final value of RC is around 2.53 ps, including the transient time and using the Equation (4.28) the upper band for bandwidth is 47 GS/s.

CHAPTER V

Design, Analysis, and Simulation of Three Different Structure for THz Beam Splitting

One of the components which is the important building block of every optical setup and, therefore, is necessary in THz range is beam splitter. In general, beam splitters used in THz setup are polarizing metallic grids, dielectric films, or substrate-coated beam splitters [78, 79, 80]. Coated dielectric beam splitters, however, introduce significant loss, for example, if the dielectric is made of alkalihalide it shows high absorption at frequencies below 7 THz [78]. Metamaterial based beam splitters, in turn, are mostly working at specific polarization and are not suitable for wavelength smaller than the structures period. The main feature drastically distinguishing SSPP BS is their reduced dimensionality. As a result, there is always scattering into the state with reversed wave vector, i.e. backscattering. Moreover, one may expect that the ability to redistribute efficiently the incoming wave into the outgoing channels is related to the strong perturbation of the SSPP flow and thus should be accompanied by the strong backscattering. The importance of the intensity of backscattering depends on details of specific applications. For example, in setups employing the small number of beam splitters, backscattered signal can be completely ignored. We address this problem in more details in the next section in the context of prospective applications in homodyne detection schemes.
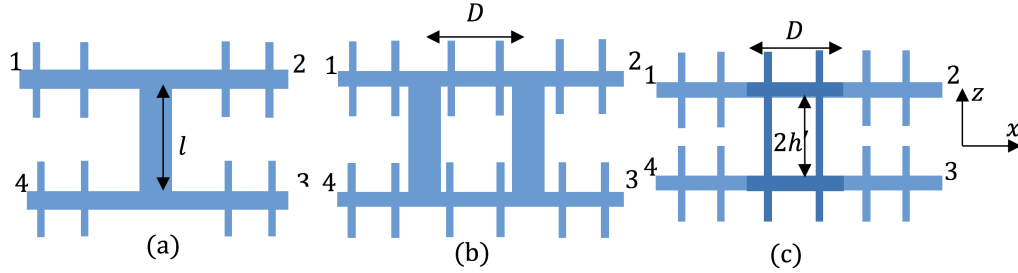
Figure 5.1: The schematic view of analyzed designs of beam splitters. In the contra- and co-propagating schemes the input ports are 1, 2 and 1, 4, respectively. (a) Two waveguides with the distance $l = 230$ μm between the arms are connected by the single connector. (b) The arms are connected by two connectors with the separation $D = 500$ μm between them. (c) The arms are coupled by means of the two-arm waveguide with common grooves, $h' = 100$ μm.

On the other hand, in large-scale setups backscattering may lead to significant reduction of the output signal, which may pose the challenging obstacle. This leads to the problem of rather finding an optimal design in terms of the trade-off between the splitting efficiency and the intensity of backscattering as is dictated by the specific application. We analyze three implementations of the SSPP BS shown in Figure 5.1, which illustrates different approaches to the problem of SSPP splitting.

5.1 SSPP mode in double corrugated waveguide

Transport of THz waves through the SSPP mode in double corrugated waveguide (see Figure 5.1) with subwavelength dimensions has been analyzed in details in the previous publications [57]. These results are directly applicable for the analysis of one- and two-connector beams splitters, but require a generalization in order to deal with the beam splitter design based on coupling through shared grooves. The generalization is based on applying the transfer matrix formalism for finding the spatial distribution of the electromagnetic field along the -direction. The closed form of the transfer matrices can be found, as will be elaborated below, keeping the lowest

frequency contributions, which is justified for the low frequency part of the spectrum.

As well as in [57], we consider $E_y = 0$. In this case instead of the full vectors of the electric and magnetic fields, it is sufficient to keep track of E_x, H_y, and if the waveguide contains layers with different dielectric functions, E_z components. Then, the SSPP dispersion law is recovered by enforcing the proper boundary conditions. Due to the periodicity in the -direction, in virtue of the Bloch theorem, it is sufficient to consider in details the field distribution within the single period. Inside the grooves E_z must vanish at the boundaries and thus we have:

$$E_x = s(y) \sum_{m>0} P_z^m cos(\frac{m\pi}{a}(z - x_L))(A^{m+}e^{iP_z^m z} + A^{m-}e^{-iP_z^m z}) \tag{5.1a}$$

$$E_z = -s(y) \sum_{m>0} \frac{m\pi}{a} sin(\frac{m\pi}{a}(z - x_L))(A^{m+}e^{iP_z^m z} - A^{m-}e^{-iP_z^m z}) \tag{5.1b}$$

$$H_y = s(y) \sum_{m>0} \frac{P_z^{m2}}{\omega} cos(\frac{m\pi}{a}(z - x_L))(A^{m+}e^{iP_z^m z} - A^{m-}e^{-iP_z^m z}) \tag{5.1c}$$

where m enumerates different modes, x_L is the x-coordinate of the left boundary of the groove, a is the width of the grooves, $s(y) = sin(\pi(y - y_F)/W)$ describes the confinement of the electromagnetic field in the -direction, $P_z^{m2} = \omega/c^2 + \pi/W^2 + m\pi/a^2$ and A^{m+} are A^{m-} the amplitudes of the waves propagating upward and downward, respectively, W is width of the waveguide, a is width of the grooves and c is speed of light. Inside the arm due to the Bloch theorem the components are given by

$$E_x = s(y) \sum_{m>0} Q_z^m e^{iq_m x}(B^{m+}e^{iP_z^m z} + B^{m-}e^{-iP_z^m z}) \tag{5.2a}$$

$$E_z = -s(y) \sum_{m>0} q_m e^{iq_m x}(B^{m+}e^{iP_z^m z} - B^{m-}e^{-iP_z^m z}) \tag{5.2b}$$

$$H_y = s(y) \sum_{m>0} \frac{P_z^{22}}{\omega} e^{iq_m x}(B^{m+}e^{iP_z^m z} - B^{m-}e^{-iP_z^m z}) \tag{5.2c}$$

where $q_m = \beta + 2\pi m/d$, β is the SSPP propagation constant, d is the period of the structure,$P_z = P_z^0$,and $Q_z^{m2} = P_z^2 - q_m^2$.

Let Z_B be the coordinate of the groove-arm interface. Enforcing the continuity ofE_x and H_y at the interface one can find the relation between amplitudes $A^{m\pm}$ and $B^{m\pm}$. The procedure is based on treating E_x in Equation (5.1a), and in Equation (5.2a) as Fourier expansions of functions, which should take the specific form at $Z = Z_B$. For example, limiting expansions in Equation (5.1a) and Equation (5.2a) to the same number of terms, one finds $B^{m+}e^{iP_z^m z} + B^{m-}e^{-iP_z^m z}$ from the condition that E_x in Equation (??) and (5.2a) vanishes in the region $x < x_L$ and $x > x_L + a$. Further, $(A^{m+}e^{iP_z^m z} - A^{m-}e^{-iP_z^m z})$ are found from the continuity of H_y . Solving the obtained system of equations with respect to $B^{m\pm}$ one obtains the transfer matrix, which maps the state of the electromagnetic field inside the groove into the state of the field inside the arm. From the formal point of view, the requirement of the number of terms in expansions Equations (5.1a) and (5.2a) being the same ensures that the dimensions of the spaces of the states of the electromagnetic field in the groove and in the arm are the same. This can be avoided in waveguides with the corrugation along one side only [81] or in highly symmetrical two-sided single arm waveguides [57] but is necessary in the general case.

In order to make main formulas less cumbersome, we will keep only terms with $l = 0$ and $m = 0$ in Equations (5.1a), (5.1b), (5.1c) and Equations (5.2a), (5.2b), (5.2c), which is justified for analysis of the low frequency part of the spectrum. Incorporating phase factors $e^{\pm iQ_z Z_B}$, where$Q_z = Q_z^0$, and $e^{\pm iP_z Z_B}$ into the amplitudes $A^\pm$ and $B^\pm$ we find implementing the procedure outlined above the relation between vectors $|A\rangle = (A^+, A^-)^T$ and $|B\rangle = (B^+, B^-)^T$ describing the electromagnetic field in the groove and in the arm, respectively, $|B\rangle = \hat{T}_{a,g} |A\rangle$, where the transfer matrix through the groove-arm interface is

$$\hat{T}_{a,g} = \frac{ie^{\beta x_c}}{2SQ_z} \begin{bmatrix} t_1 + t_2 & t_1 - t_2 \\ t_1 - t_2 & t_1 + t_2 \end{bmatrix} \tag{5.3}$$

Here $x_c = x_L + a/2$ is the x-coordinate of the center of the groove, $S = \sqrt{a/d}sinc(\beta a/2)$, $t_1 = S^2 P_z d$, $t_2 = Q_z a$. The transfer matrix for the transition from the arm to the groove is found by simple inversion $\hat{T}_{a,g} = \hat{T}_{a,g}^{-1}$. Since the phase factors were incorporated into the amplitudes, the phase difference between the amplitudes at opposite ends of an element (either groove or arm) is accounted for by introducing diagonal matrices $\hat{T}_{g,g} = diag(e^{iP_z h}, e^{-iP_z h})$ and $\hat{T}_{a,a} = diag(e^{2iQ_z t}, e^{-2iQ_z t})$ for the groove with height h and the arm with height 2t . The total transfer matrix $\hat{T}_{tot}$ connecting the state of the electromagnetic field at the upper and lower ends of the structure is found by taking the ordered product of the transfer matrices through individual elements. For example, for the single arm waveguide this is

$$\hat{T}_{SA} = \hat{T}_{gg}\hat{T}_{ga}\hat{T}_{aa}\hat{T}_{ag}\hat{T}_{gg} \tag{5.4}$$

while for the two arm waveguide with shared grooves we have

$$\hat{T}_{TA} = \hat{T}_{gg}\hat{T}_{ga}\hat{T}_{aa}\hat{T}_{ag'}\hat{T}_{g'g'}\hat{T}_{g'g'}\hat{T}_{g'a}\hat{T}_{aa}\hat{T}_{ag}\hat{T}_{gg} \tag{5.5}$$

The distribution of the field must satisfy certain boundary conditions at the ends of the structure. For the case of our main interest, when the structure is terminated by closed grooves, E_x must vanish at the ends. Thus, we have $A^+ + A^- = 0$ or in vector notations $\langle x||A\rangle$ or equivalently $\langle A| = c\,|-x\rangle$, where c is an arbitrary number, $|\pm x\rangle = (1, \pm 1)^T/\sqrt{2}$ and bra- and ket-vectors are related as usual through Hermitian

conjugation. Thus, in the case of our main interest, closed structures, the SSPP dispersion equations are

$$\langle x | \hat{T}_{tot} | A \rangle \tag{5.6}$$

Since the left hand side of this equation defines an analytic function of ω, for a given β, Equation (5.6) holds only for isolated frequencies $\omega = \omega_i(\beta)$, which thus define branches of the SSPP dispersion curve when β varies from $-\pi/d$ to π/d. Due to the mirror symmetry of the structures under consideration, the dispersion equation factorizes $D^e(\omega, \beta) D^o(\omega, \beta) = 0$ because the modes possess the definite transformation properties under reflections about the middle line. It is convenient to classify the modes according to the sign of charge on the horizontal boundaries, or, equivalently, according to the sign of E_z : the even and odd modes are characterized by even and odd functions $E_z(z)$. The even mode, therefore, has E_x vanishing at the middle line and thus the transfer matrix through half of the structure,$\hat{T}_{half}$, must map $|-x\rangle$ into $|-x\rangle$, which leads to

$$D^e(\omega, \beta) = \langle x | \hat{T}_{half} | -x \rangle \tag{5.7}$$

The similar argument for an odd mode yields

$$D^e(\omega, \beta) = \langle -x | \hat{T}_{half} | -x \rangle \tag{5.8}$$

For the single arm waveguide this leads to already known result
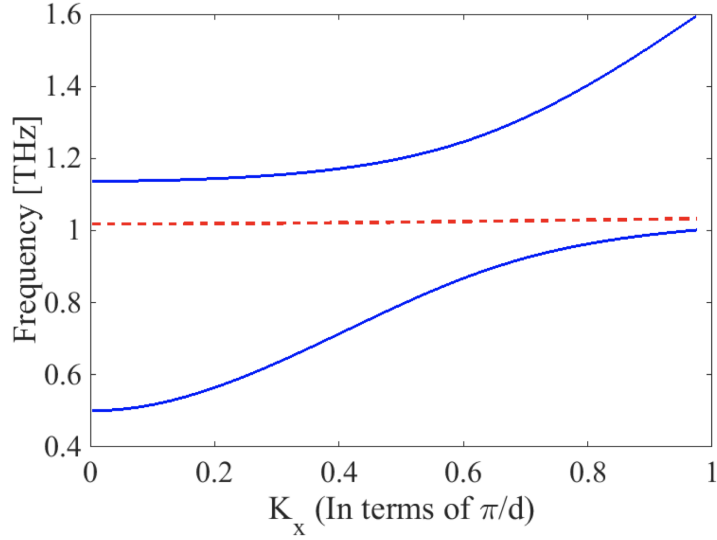
Figure 5.2: The lowest three bands of SSPP in the single arm waveguide. Solid lines show solutions of $D_{SA}^e(\omega, \beta)D = 0$ and correspond to the first and second symmetric modes. The dashed line depicts the first antisymmetric mode and is found from $D_{SA}^0(\omega, \beta)D = 0$.

$$D_{SA}^e(\omega, \beta) = 1 + \eta \frac{tan(P_z h)}{tan(Q_z t)'} \tag{5.9a}$$

$$D_{SA}^o(\omega, \beta) = 1 - \eta tan(P_z h)tan(Q_z t) \tag{5.9b}$$

where $\eta = S^2 \frac{P_z}{Q_z}$. First three branches determined by Equations (5.9a) and (5.9b) are shown in Figure 5.2.

The dispersion law of SSPP in the two-arm waveguide with shared grooves is derived in the same way. It should be noted that in this case $D_{TA}^e(\omega, \beta) = \langle x | \hat{T}_{half} | -x \rangle = 0$ has the form for the dispersion equation of the single arm waveguide with grooves, generally, of different heights h and h'. The non-zero difference between them breaks the symmetry of the effective single arm waveguide, which leads to the coupling between its even and odd modes. Thus, we have:

$$D_{TA}^e(\omega, \beta) = D_{SA}^e(\omega, \beta), \ \ D_{SA}^o - (1 - \eta^2)\frac{sin^2(\frac{1}{2}(h - h')P_z)}{cos^2(\frac{1}{2}(h + h')P_z)} \qquad (5.10)$$

which, in particular, shows the effect of the length of the shared grooves on the SSPP dispersion curves. The two-arm waveguide, however, does not have the convenient factorization property and has somewhat cumbersome form

$$D_{TA}^o(\omega, \beta) = cos(P_z(h + h'))$$
$$- tan(2Q_z t)[\eta cos(P_z h)sin(P_z h') + \eta^{-1}sin(P_z h)cos(P_z h')] \qquad (5.11)$$

The solutions of equations $D_{TA}^e(\omega, \beta)D = 0$ and $D_{TA}^o(\omega, \beta)D = 0$ are shown in Figure 5.3.
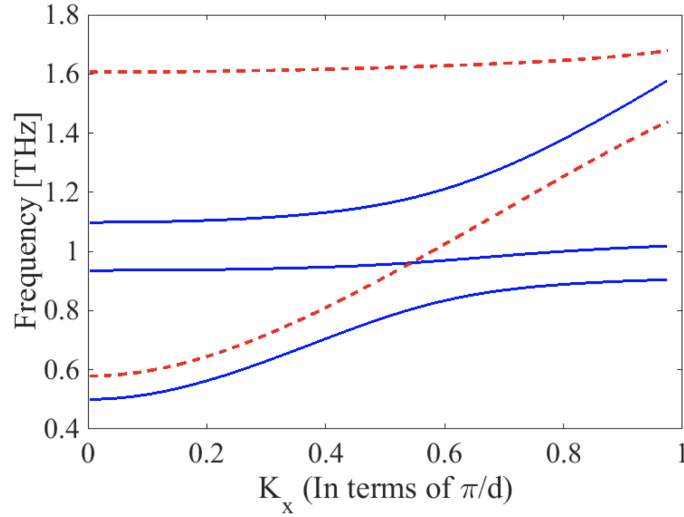
Figure 5.3: The SSPP dispersion law in the two-arm waveguide with shared grooves (the middle part of the structure shown in Figure 5.1 c). Solid and dashed lines show symmetric and ant-symmetric modes, respectively.

5.2   Beam splitter's performances

Obtained dispersion laws allow us to discuss the main features of the SSPP propagation through beam splitters. The easiest case is the implementation shown in Figure 5.1, which we will refer to as the single-connector beam splitter (SC). It can be regarded as consisting of two connected T-junctions. Thus, considering ports 1 and 2 as input ports and ports 3 and 4 as output, that is in the contra-propagating scheme, one can expect that due to the mirror symmetry with respect to the central vertical line the supplied input should be split equally between the output ports. In order to characterize quantitatively the transport properties, we introduce $|S(i,j)|^2$, the normalized output power at port j with the input at port i, so that $|S(i,1)|^2 + ... + |S(i,4)|^2 = 1$. In the contra-propagating setup, ports 1 and 2 (see Figure 5.1) are input ports and ports 3 and 4 are regarded as output. In the co-propagating scheme, the input is supplied at ports 1 and 4 and the output is collected at ports 2 and 3. The characteristic of special importance, as will be illustrated in the next section, is the splitting ratio, or balance. For a symmetric contra-propagating beam splitter, i.e. with input ports 1 and 2, the balance is fully characterized by the ratio $b(\omega) = |S(1,3)|^2/|S(1,4)|^2$, for the co-propagating beam splitter, when ports 1 and 4 are input, the splitting ratio is defined as $b(\omega) = |S(1,2)|^2/|S(1,3)|^2$. For both cases, when $b(\omega) = 1$ the beam splitter is balanced, otherwise it is unbalanced.

Figure 5.4 shows the frequency dependence of the parameters $|S(i,j)|^2$ for the simplest design with one connector. It is assumed here and in the following figures that the input signal is supplied at port 1. Due to the symmetry of the structure, the full set of parameters $|S(i,j)|^2$ is obtained by simple re-enumeration of the ports. For example, for the contra-propagating scheme the output signal with input at port 2 is found as $|S(2,3)|^2 = |S(1,4)|^2$ and $|S(2,4)|^2 = |S(1,3)|^2$, while the backscattered signal is found as $|S(2,2)|^2 = |S(1,1)|^2$ and $|S(2,1)|^2 = |S(1,2)|^2$. For the co-propagating scheme, the input is supplied at ports 1 and 4, hence, the output

signal is determined by $|S(1,2)|^2 = |S(4,3)|^2$ and $|S(1,3)|^2 = |S(4,2)|^2$ and the backscattered signal is found from $|S(1,1)|^2 = |S(4,4)|^2$ and $|S(1,4)|^2 = |S(4,1)|^2$.
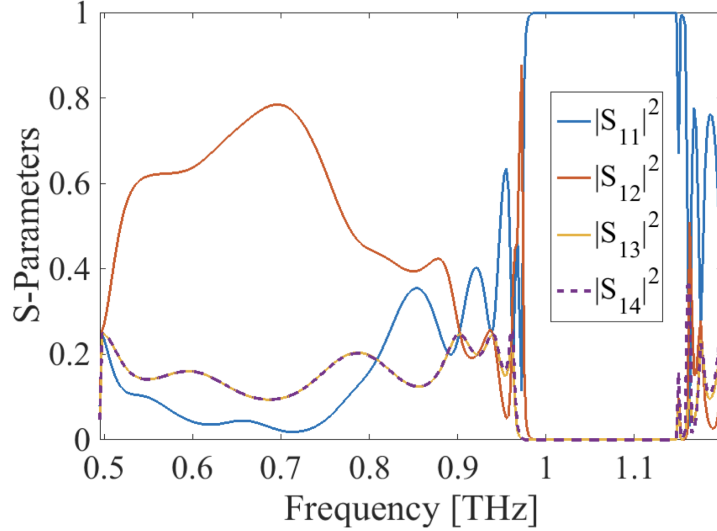
Figure 5.4: The frequency dependence of S-parameters of the single connector beam splitter.

The characteristic feature of Figure 5.4 is practically coinciding curves $|S(1,3)|^2$ and $|S(1,4)|^2$, which characterize the output signal in the contra-propagating scheme. This confirms the observation based on the symmetry of the structure made above. At the same time, it should be noticed that in the co-propagating scheme the equal splitting is reached when curves corresponding to $|S(1,2)|^2$ and $|S(1,3)|^2$ intersect, which occurs at isolated frequencies near the low-frequency edge of the SSPP waveguide. As has been discussed above, another important characteristic is the intensity of backscattering, which is defined in terms of the scattering intensities as $|S(1,1)|^2 + |S(1,2)|^2 = 1 - |S(1,3)|^2 - |S(1,4)|^2$. Figure 5.4 demonstrates that for the single-connector design connector the high intensity of the backscattered signal, $R(\omega) > 0.5$ is rather typical, which, as has been discussed above, may be a highly undesirable property. The numerical calculations were performed using HFSS simulation package, and the ports are terminated to the matched load, so that there is no reflection at the ports termination back into the structure.

The problem of significant backscattering can be approached utilizing more complex designs in two ways: with the help of destructive interference of backscattered waves or by reducing backscattering itself. The implementation of the first principle in the beam splitter with two connectors (TC) is shown in Figure 5.1.

In this case, the backscattered field at the input ports is the result of interference of waves scattered on different junctions. In order to get better understanding of the mechanism of reduction of backscattering we consider the propagation across the beam splitter approximating the propagation of the electromagnetic wave into the connector by the main component with the propagation constant $k = \sqrt{P^2 - (\pi/d_c)^2}$, d_c where is the width of the connector in the x-direction. Then the propagation of the SSPP can be described by the transfer matrices of the form $T^e = T^e_c T_W T^e_c$ and $T^o = T^o_c T_W T^o_c$, for the even and odd modes of the beam splitter, respectively. The scattering into the even and odd modes of the connector is described by the transfer matrices [32] respectively, and the propagation of the SSPP in the arm is described by

$$T^e_c = \begin{bmatrix} 1 & 0 \\ iZ_1^{-1}tan(kl/2) & 1 \end{bmatrix} \tag{5.12a}$$

$$T^o_c = \begin{bmatrix} 1 & 0 \\ -iZ_1^{-1}cot(kl/2) & 1 \end{bmatrix} \tag{5.12b}$$

$$T_W = \begin{bmatrix} cos(\beta D) & iZ_0 sin(\beta D) \\ -iZ_0 sin(\beta D) & cos(\beta(\beta D)) \end{bmatrix} \tag{5.12c}$$

Here D and l are the distances between the arms and connectors, respectively, $Z_1 = \omega/k$, $Z_0 = -\omega\beta/c^2 P^2$. Parameters $S(i,j)$ can be expressed in terms of the matrix elements of the transfer matrices T^e and T^o (see e.g. Secion 4 of [82]). Imposing the condition of minimal power at the input ports, i.e. minimal backscattering, we find

68
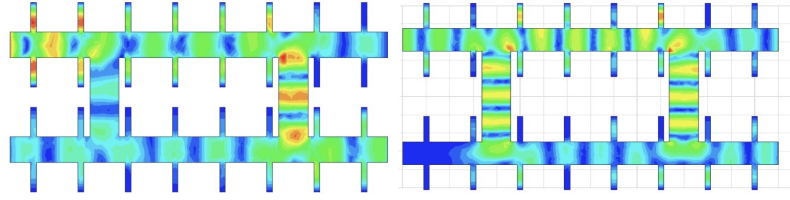
Figure 5.5: The significant reduction of the intensity of backscattering in the two-connector beam splitter with variation of the distance between the arms. The input is supplied at port 1 and backscattering is registered at port 4.

that the necessary condition is

$$tan(\frac{kl}{2} = 1) \tag{5.13}$$

Thus, one can achieve reduced backscattering in TC at given frequency by making the structure with specially chosen distance between the arms. In order to demonstrate this effect, we compare in Figure 5.5 the field distribution inside two structures with slightly different at the same frequency. The frequency dependence of the - parameters of the TC is shown in Figure 5.6. It should be noted that while backscattering in TC is significantly reduced comparing to SC, the simultaneous reach of balanced splitting and low backscattering requires careful adjusting the parameters of the structure and thus this design is more suitable for narrowband applications. More direct control over backscattering is achieved in the implementation of the SSPP beam splitter shown in Figure 5.1(c). The advantage of such constructed beam splitter is that the translational symmetry is broken in a less invasive way. Moreover, by careful choosing the characteristics of the waveguides, one can eliminate the variation of the SSPP propagation constant at the junction between the parts of the waveguide with disjoint arms and with arms sharing grooves thus reducing the backscattering in a stable (non-resonant) manner.
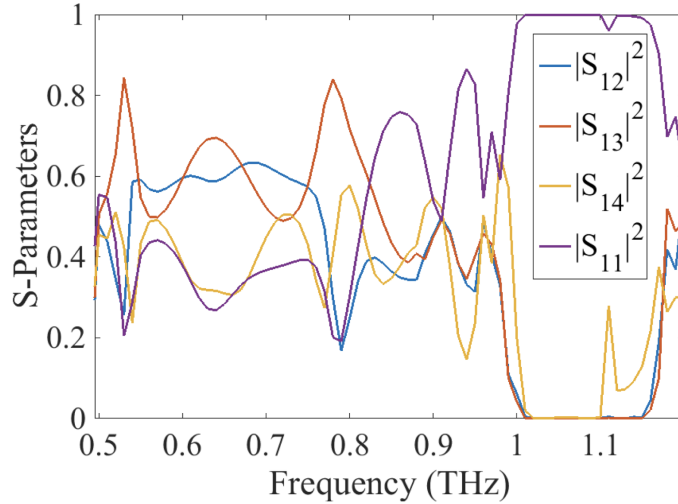
Figure 5.6: The frequency dependence of S-parameters of the two-connector beam splitter.

Indeed, as Equation (5.8) shows, the fundamental branch of a two-arm waveguide can be presented as a result of coupling between the even mode of the single-arm waveguide (i.e. its fundamental branch) and the lowest odd mode, with the coupling parameter proportional to the difference between heights of the shared and non-shared grooves. Thus, for frequencies not too close to the edge of the fundamental branch, where the coupling between the even and odd modes is significant, the lowest modes of the single- and two-arm waveguides differ only slightly.

Therefore, for a given frequency the mismatch between the propagation constants, and, hence, the impedance mismatch, between the parts of the beam splitter with disjoint arms and with arms sharing grooves is small. This observation is confirmed by the numerical simulations presented in Figure 5.7. It shows in particular that, as well as in the case of the beam splitter with two-connectors, the equal splitting ratio is reached at isolated frequencies. A drawback of this design, however, should be noted. The coupling between SSPP modes propagating in different arms is relatively weak. This results in the necessity of having long length of the beam splitter, when the effect of attenuation may become pronounced
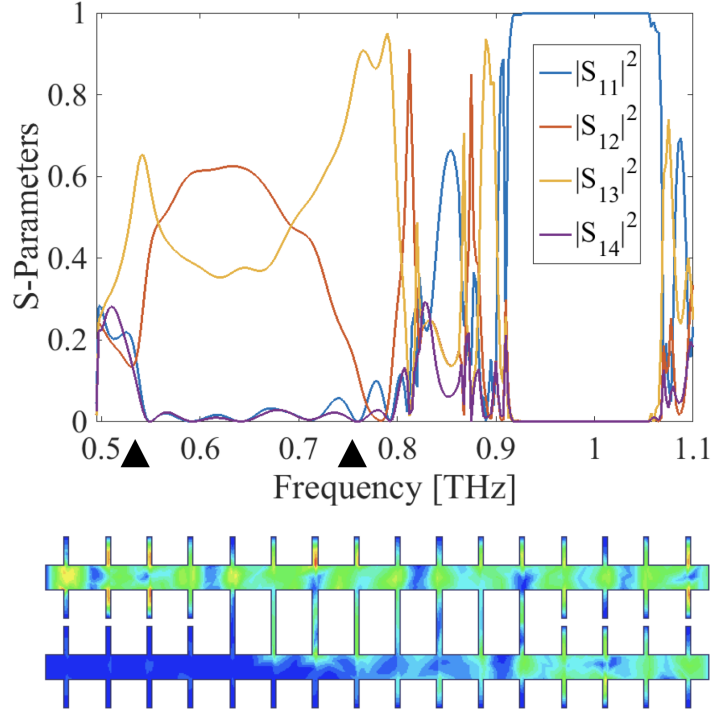
Figure 5.7: (Upper panel) S-parameters of the beam splitter based on coupling through shared grooves. The black markers indicate the frequency range with suppressed backscattering. (Lower panel) The field distribution inside the beam splitter demonstrating the reduced back scattering and the gradual formation of the split signal.

5.3 Four-terminal beam splitter with backscattering

One of the important applications of the beam splitter is in various quantum optical experiments, for instance, Hong-Ou-Mandel type of experiments and homodyne detection. The standard description of these experiments assumes that the distinction between the input and output ports is strict. At the same time, all designs considered in the previous section demonstrate backscattering for a generic frequency. As a result, the standard description of the beam splitter adopted in quantum optics is not directly applicable but requires a slight generalization to account that sending a pulse into either port produces, generally speaking, outgoing signals in all port. Thus, the relation between incoming and outgoing states is provided by 4×4 a scattering

matrix $\hat{S}$

$$\begin{bmatrix} b_1 \\ \vdots \\ b_4 \end{bmatrix} = \hat{S} \begin{bmatrix} a_1 \\ \vdots \\ a_4 \end{bmatrix} \tag{5.14}$$

where a_i is the operator corresponding to incoming SSPP in port i and b_i describe outgoing SSPP.

Out of the variety of possible applications of transformations of quantum states described by Equation (5.14), we pay the special attention to the implementation of the balanced homodyne detection scheme. Without the loss of generality, we can consider the case when the incoming SSPP states are supplied in ports 1 and 2 only, while only the outgoing states in ports 3 and 4 are detected.

In order to explicate such setup, we collect indices 1,2 into set in and indices 3,4 into set . Then Equation (5.14) can be rewritten in the block form

$$\begin{bmatrix} b_{in} \\ b_{out} \end{bmatrix} = \hat{S} \begin{bmatrix} a_{in} \\ a_{out} \end{bmatrix} \tag{5.15}$$

where the scattering matrix $\hat{S}$ is written as

$$\hat{S} = \begin{bmatrix} \hat{S}_{in,in} & \hat{S}_{in,out} \\ \hat{S}_{out,in} & \hat{S}_{out,out} \end{bmatrix} \tag{5.16}$$

and $\hat{S}_{i,j}$ are 2×2 matrices.

A general one-particle observable involving ports 3 and 4 can be represented as

operator

$$V_{out} = V_0 \ J_0(b^+_{out}, b_{out}) + V \ J_0(b^+_{out}, b_{out}) \tag{5.17}$$

where a scalar V_0 and a 3d unit vector V characterize measured quantity and

$$J_i(b^+, b) = \frac{1}{2} \sum_{m,n \in 3,4} b^+_m (\sigma_i)_{m,n} b_n \tag{5.18}$$

with and being the usual Pauli matrices.

It should be noted that the similar approach can be used for describing a general observable involving all four ports. In this case instead of the Pauli matrices one needs to employ the full family of generators of su(4) Lie algebra. This general case, however, is beyond the scope of the current consideration and will not be analyzed here. Equation (5.17) presents the observable in the basis of the outgoing states. Using Equation (5.17) and taking into account that we are only interested in the case when the input is supplied at ports 1 and 2, we find

$$V_{in} = V'_0 \ J_0(a^+_{out}, a_{out}) + V' \ J_0(a^+_{in}, a_{in}) J \tag{5.19}$$

where we have introduced the modified pair (V'_0, V) defined by the relation

$$\sum_i V'_i \sigma_i = \sum_i V_i (\hat{S}^+_{out,in} \sigma_i \hat{S}_{out,in}) \tag{5.20}$$

This relation can be alternatively written in terms of linear transformation $V'_i =$

73

$\sum_j R_{i,j} V_j$, where the matrix elements $R_{i,j}$ are found using the orthonormality relation $Tr(\sigma_i \sigma_j) = 2^{-1} \delta_{i,j}$. The application of this formalism for the homodyne detection is simplified by two circumstances. First, we require that the measured quantity must be a linear function of the operators corresponding to the unknown state (say, supplied at port 1). Thus, we require that $V'_0 = V'_z = 0$. Second, we take into consideration that only intensity is measured at the output ports, so that $V_x = V_y = 0$. Applying the orthonormality relation these conditions can be written as a system of homogeneous equations with respect to V_0 and V_z

$$Tr[\sigma_i \hat{S}_{out,in}(V_0 \sigma_0 + V_z \sigma_z)\hat{S}_{out,in}] = 0 \tag{5.21}$$

where $i = 0, z$. Writing out explicitly the matrices involved, one finds that this system has a nontrivial solution $V_0 = 0, V_z = 1$ only when $|S(3,1)|^2 |S(4,2)|^2 = |S(4,1)|^2 |S(3,2)|^2$. For the case of a design symmetric with respect to the middle line this implies that in order to be employed in the homodyne detection scheme the beam splitter must be balanced, so that $|S(3,1)|^2 = |S(4,2)|^2 = |S(4,1)|^2 = |S(3,2)|^2 = p$. Using these findings in Equation (5.20), we find

$$V'_x = p(cos(\phi_{3,1} - \phi_{3,2}) - cos(\phi_{4,1} - \phi_{4,2})) \tag{5.22a}$$

$$V'_y = p(sin(\phi_{3,1} - \phi_{3,2}) - sin(\phi_{4,1} - \phi_{4,2})) \tag{5.22b}$$

where $\phi_{i,j} = arg(S_{i,j})$ are phases of the respective scattering amplitudes. Equations Equations (5.22a) and (5.22b) show the important consequence of the symmetry of the beam splitter on the form of the observable operator in the basis of incoming states. In this case one has $\phi_{3,1} - \phi_{3,2} = \phi_{4,2} - \phi_{4,1}$ and, as a result, $V'_x = 0$ Thus the beam splitters with the symmetry with respect to the middle line allows one to measure only the p-quadrature. By breaking the mirror symmetry, for instance, by

means of filling the beam splitter partially by a dielectric material, as is considered in the next section, the phase parameter of the beam splitter can be varied. Such modification, however, leads in general to changing the splitting ratio and, as a result, the beam splitter becomes unbalanced. Thus, the variation of the phase parameter requires more complex control.

CHAPTER VI

Mechanical Pressure Exerted by SSPP

Surface plasmon polaritons (SPP), optically excited plasmon polariton at the interface of dielectric and metal, opened a broad way to miniaturized photonic circuits or designing subwavelength structure that can carry optical or electrical signal [1]. The SPPs have found their applications in many areas such as modulators, switches, sensors, etc. [2-5]. Recently, there have been many efforts to utilize the plasmon polaritons at frequencies in the THz range (0.3-10 THz). Unfortunately, elevated medium losses at lower frequencies make implementing of this technique highly impractical. It has been shown, however, that by engineering the metal or dielectric surface and implementing periodic patterns such as grooves or holes, one can reintroduce the concept of surface plasmon at lower frequencies. It has been demonstrated that these structures mimic the dispersion properties of surface plasmon polariton [6], and the respective propagation modes are dubbed spoof surface plasmon polariton (SSPP). In the sub-wavelength limit, when the characteristic spatial scales of the structure (e.g., period and the width of the grooves or holes) are smaller than the operating wavelength, the designed surface can be represented as an effective media with the dielectric function having the Drude form. SSPP structures have attracted a significant attention of researchers, from both theoretical and experimental perspectives, as they can offer localized field enhancement at the frequency range where

true plasmons do not exist. In the past decade, different structures with periodic perforation have been studied, including double sided corrugated structure, single sided corrugated waveguide, cylindrically corrugated waveguide, etc. [22-29]. Utilizing the SSPP modes, different components have been proposed, such as polarization controller [28], THz switch [29], analog to digital convertor (ADC) [30], and beam splitter [31]. Beside these applications of the optical and THz waves in plasmonic and SSPP waveguides, recently there has been significant interest in electromagnetic forces in dielectric and waveguide structures in order to utilize the electromagnetic (EM) force in optomechanical or micro electro mechanical MEMs devices. Pernice et al [83] studied the optical forces in parallel waveguides. Optical forces between metallic nano particle has been investigated in [84, 85]. Povinelli et al. [86] suggested that the optical force can be increased by optical resonances and it has been theoretically proven in [87]. The optical forces have been also investigated in a wide variety of structures such as photonic crystals and plasmonic waveguides, [88, 89], for different applications and situations, such as force on nano-particles, between two single-sided spoof plasmon waveguides, etc. [90, 91, 92, 93, 94, 95, 96, 97]. In the present paper, we apply the same concept of resonantly enhanced electromagnetic force to investigate the mechanical action of SSPP inside corrugated waveguides. This paper is organized as follows, in Section 1, we briefly review a theoretical description of SSPP in double sided corrugated waveguides and their dispersion diagram. In Section 2, the Maxwell stress tensor formalism is introduced and the force acting on a small dielectric particle inside the SSPP waveguide is evaluated. Section 3 discusses the force exerted by the SSPP field on a small particle and Section 4 analyzes the force distribution inside the SSPP waveguide and proposes a switching mechanism. Double sided corrugated waveguide While the results presented below have a wide range of applicability, for concreteness, we limit our attention to closed waveguides, which is especially relevant for potential microfluidic applications. More specifically, we con-

sider double corrugated waveguides, as shown in Figure 6.1. SSPP in such structures were analyzed in prvious section therefore, we only briefly outline the main points.
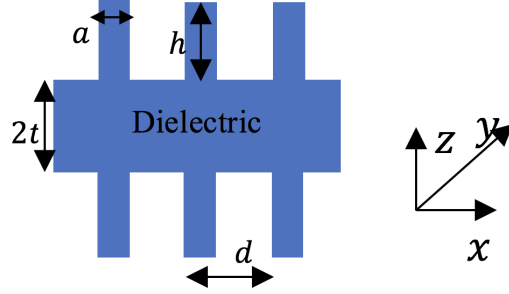
Figure 6.1: Cross section view of Doubly corrugated waveguide.

For simplicity, we only will keep the lower modes with l=0 and m=0 in Equation (??), thus obtaining the dispersion equations governing even and odd SSPP modes

$$D_{SA}^e(\omega, \beta) = 1 + \eta \frac{tan(P_z h)}{tan(Q_z t)'} \tag{6.1a}$$

$$D_{SA}^o(\omega, \beta) = 1 - \eta tan(P_z h) tan(Q_z t) \tag{6.1b}$$

First five branches determined by Equations (6.1a) and (6.1b) are shown in Figure 6.2 and compared with the transmission spectrum of the waveguide which is calculated using HFSS. Throughout this paper, the dimensions of the waveguide are fixed and set to be as follows: $d = 100 \ \mu m$, $h = 80 \ \mu m$, $a = 10 \ \mu m$, $W = 300 \ \mu m$, $t = 33.3 \ \mu m$.

6.1   Maxwell Stress Tensor

The force acting on a particle placed into the waveguide is found as the flux of the Maxwell stress tensor through the surface S encompassing the particle, $F = \int \hat{T}.dn$. If the medium inside the waveguide has the dielectric function $\epsilon = 1$, the stress tensor
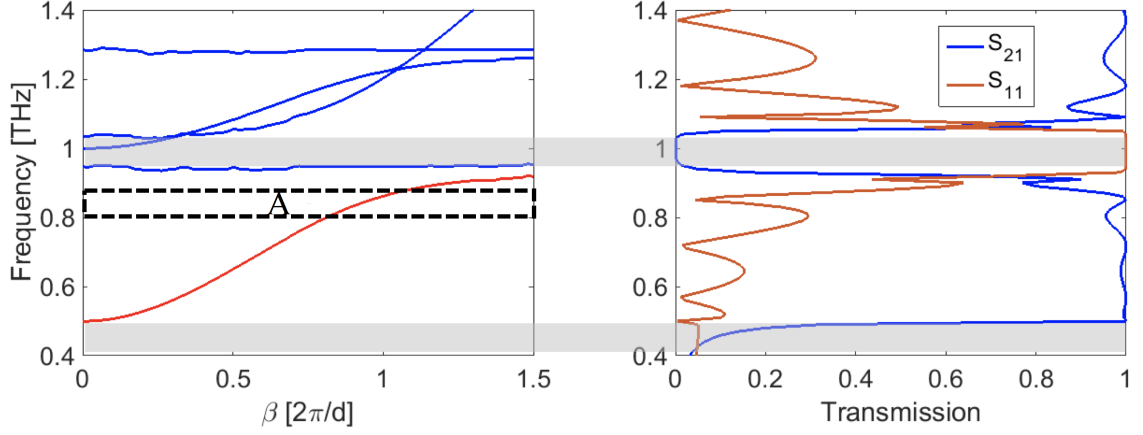
Figure 6.2: Dispersion diagram and scattering parameters of the double corrugated waveguide. Gray areas represent the band gaps. The dashed rectangular area represents the frequencies that we see SSPP modes.

can be written as [98]

$$\hat{T} = \epsilon_0 E \otimes E + \frac{1}{\mu_0} B \otimes B - \frac{1}{2}(\epsilon_0 E^2 + \frac{1}{\mu_0 B^2})\hat{I} \tag{6.2}$$

where

$\hat{I}$ is the unit tensor, $\otimes$ is the Cartesian product defined as $(a \otimes b)_{i,j} = a_i b_j$ and $E^2 = E.E$. Representing the electric and magnetic fields in the form

$$E(r,t) = E_0^*(r)e^{i\omega t} + E_0(r)e^{-i\omega t} \tag{6.3a}$$

$$E(r,t) = B_0^*(r)e^{i\omega t} + B_0(r)e^{-i\omega t} \tag{6.3b}$$

we obtain the Maxwell tensor as a sum of time independent and oscillating components.

$$\hat{T} = \hat{T}_s + \hat{T}_0^* e^{2i\omega t} + \hat{T}_0^* e^{-2i\omega t} \tag{6.4}$$

where

$$\hat{T}_s = 2Re[\epsilon_0 E \otimes E + \frac{1}{\mu_0}B \otimes B - \frac{1}{2}(\epsilon_0|E_0^2| + \frac{1}{\mu_0|B_0^2|})\hat{I}] \quad (6.5)$$

with $lvertE_0^2| = E_0^*E_0$, and

$$\hat{T}_0 = \epsilon_0 E_0 \otimes E_0 + \frac{1}{\mu_0}B_0 \otimes B_0 - \frac{1}{2}(\epsilon_0 E_0^2 + \frac{1}{\mu_0 B_0^2})\hat{I} \quad (6.6)$$

The time independent component $\hat{T}_s$ yields the stationary force $F = \int \hat{T}.dn$ characterizing the pressure exerted by the SSPP on the dielectric particle. The effect of the oscillating terms is usually neglected because they vanish after averaging over the period. It should be noted, however, that these terms alone result in oscillations of the center of mass of the specimen near the position drifting with the velocity $v_d = Im(F_0)/m\omega$, where is the mass of the specimen and $F_0 = \int \hat{T}_0.dn$. Depending on situation, the displacement due to the drift may play an important role and should be taken into consideration. Indeed, the flux of the Maxwell tensor through a surface encompassing a particle with radius is proportional to the area of the surface $\propto r^2$, while the mass of the particle is proportional to its volume, $\propto r^3$, leading to $v_d \propto 1/r$. As a result, the effect of drift may be important while dealing with small light particles in a liquid environment with low viscosity. Since we are interested in a mechanical action of a THz field, however, we use the fact that in high frequency fields, the effect of the drift is subsided and neglect it.

6.2 Dielectric particles inside the SSPP field

The total force acting on a small particle can be calculated using Equation (6.6), which includes two different kind of forces as gradient and scattering force [32]:

$$\vec{F_0} = \frac{\epsilon_r \epsilon_0}{2} Re[\alpha(E_0 . \bigtriangledown E_0^* + \alpha \frac{\delta}{\delta t}(E_0 \times B_0^*))] \tag{6.7}$$

where α is the polarizability. The gradient force is the part that is responsible for attraction or repulsion of the particle toward the high intensity field. Inserting the Maxwell equation $\bigtriangledown \times E = -\delta B/\delta t$ and using the vector calculus identity $\bigtriangledown(E.E^*) = 2Re[(E.\bigtriangledown)E^* + E \times (\bigtriangledown \times E^*)]$ the final form of the gradient force can be calculated as:

$$\vec{F_0} = \frac{\epsilon_r \epsilon_0}{2} Re(\alpha)(\bigtriangledown E_0 . E_0^*) \tag{6.8}$$

It should be noted that the electric field entering the expression for the Maxwell stress tensor is a solution of the full system of Maxwell equations including both the periodic corrugation of the waveguide and the inserted particle. If, however, the particle is small and its refractive index only slightly differs from that of surrounding medium, one can use Equation (6.7) with $E = E_{SSPP}$, where E_{SSPP} is the SSPP field in a corrugated waveguide free of introduced particles. Indeed, in this case, the electric field can be presented as a superposition of E_{SSPP} and the scattered field. The latter, in turn, in the lowest order of the perturbation theory is proportional to E_{SSPP} and the variation of the refractive index, which yields Equation (6.7) with E_{SSPP}. A direct manifestation of such approximation is a simple linear dependence of the force on the refractive index of the particle. We test this conclusion in Fig-

ure 6.3, which shows that the approximation E_{SSPP} is valid for a particle with the dimensions of 1 μm up to n=1.3 . We would like to stress, however, that as the size of the particle or its refractive index increase, the simplest approximation no longer provides a good description of the electromagnetic field. Strong scattering not only leads to a modification of an effective refractive index of the particle but may result in a complete reconstruction of the field of the propagating modes of the corrugated waveguide. As a simple illustration, we plot in Figure 6.3 the frequency dependence of the electromagnetic force acting on a large particle placed near the groove opening. It shows that the mechanical action of the electromagnetic field leads to repelling the particle away from the region of the high field concentration in a particle-free waveguide. In other words, it shows the behavior opposite to that for small particles. The physical origin of such behavior is as follows. A large particle effectively modifies the dielectric properties of the groove, thus making the groove different from the rest of the structure. This, in turn, may lead to formation of SSPP modes characteristic for heterogeneous structures, which can be drastically different from those of homogeneous waveguides [70].

In the present paper, we limit ourselves to an analysis of the case when the approximation of small particles is applicable and one can substitute $E = E_{SSPP}$ into Equation (6.7). In this case, one can extend the analysis based on Equations (6.1a), (6.1b), and (6.2) for a qualitative description of the spatial profile of the force field. In particular, one can see from the series representation of the field inside the arm that the characteristic pattern of the field distribution is a result of the superposition of higher order Bloch modes. While moving away from the interface toward the center of the arm, the contribution of higher Bloch modes can be expected to quickly attenuate owing to the m-dependence of $k_m = \sqrt{\left(\beta + 2\pi/d\right)^2 - \omega^2/c^2}$. While this conclusion is qualitatively correct for generic and spectral points, it is not sufficient for describing details of the spatial variation of the field. Indeed, at frequencies close
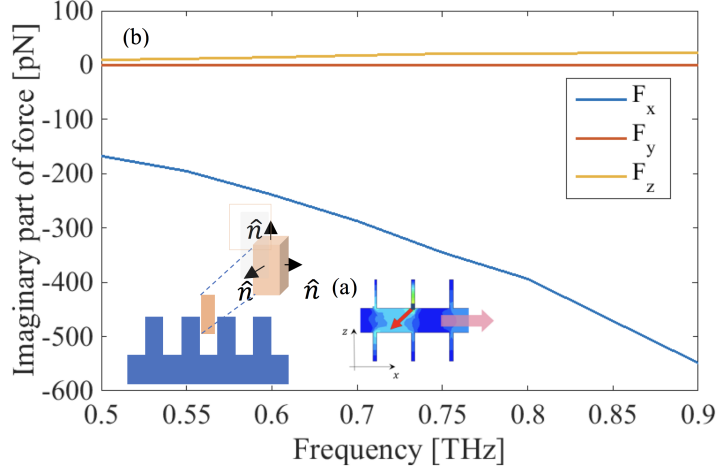
Figure 6.3: Pressure exerted by SSPP on a particle placed near the groove opening. (a) The field distribution in the waveguide in the presence of the particle. The red arrow indicates the general direction of the force; the bold pink arrow shows the direction of SSPP propagation. (b) The frequency dependence of the x, y, and z components of the force acting on the particle.

to band edges, where $\beta \approx= \pi/d$, one has $Q_0 \approx_{-1}$ and, thus, not too close to the groove/arm interface, the field distribution is a result of interference of m=0 and m=-1 Bloch modes.

We discuss the form of the field distribution for the case of a structure with wide arm. Then in a region, which is not too close to the groove/arm interface and to the center of the arm, we can retain only and Bloch modes and, additionally, neglect the contribution of , since due to the symmetry with respect to the plane passing through the center of the arm, one has . Using these simplifications, we obtain for

$$E_x^2 + E_z^2 = g^2 e^{-kz}(k^2 cos^2(\beta x) + \beta^2 sin^2(\beta x)) \tag{6.9}$$

where x is counted from the center of the groove opening, $k = k_0$ and g is a constant. Expanding k, we finally obtain

$$E_x^2 + E_z^2 = g^2 e^{-kz}/beta^2(1 - \frac{\omega^2}{\beta^2 c^2} cos^2(\beta x)) \tag{6.10}$$

which demonstrates the characteristic oscillations along the -axis with the magnitude determined by the deviation of the SSPP spectral point $(\omega, \beta(\omega))$ from the light line $\omega = \beta c$.
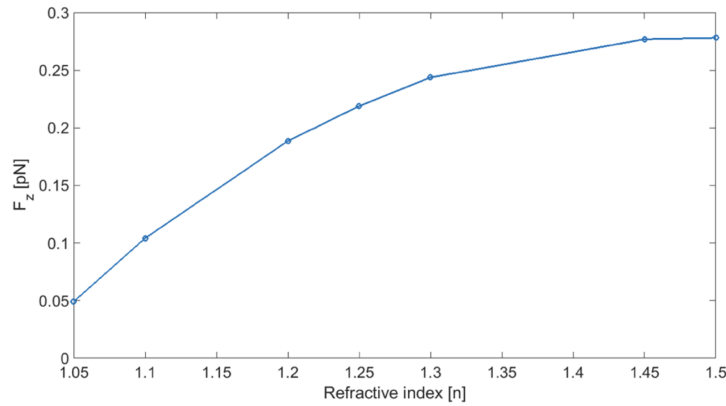
Figure 6.4: force in z-direction versus the refractive index for small cubic dielectric with dimensions 1 $\mu m \times 1$ $\mu m \times 1$ μm.

Figure 6.5 shows the magnitude of electric field inside the waveguide at the frequency of 0.87 THz (frequency lies in the region, where the waveguide support SSPP modes and we have high field concentration inside and at the opening of groove, this region is shown by letter A in Figure 6.2) in the presence of a small dielectric cube with dimensions of 1 $\mu m \times 1$ $\mu m \times 1$ μm and the refractive index 1.2.

6.3   Switching mechanism in SSPP waveguide

As mentioned earlier, when the operating frequency approaches the resonant frequency of the grooves, the field concentration inside the grooves increases, this means we can control the field concentration at regions close to the opening of the grooves and as a result alter the force inserting on a particle inside the SSPP waveguide.
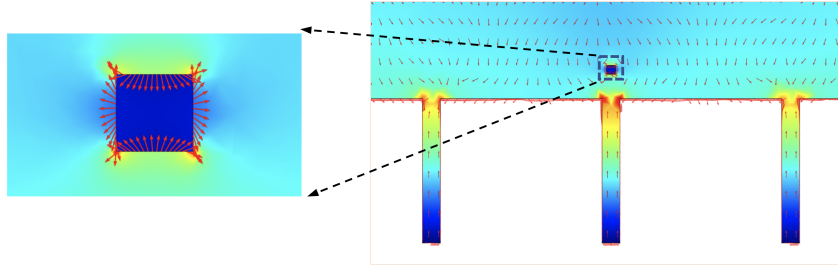
Figure 6.5: (a) Magnitude of electric field inside the SSPP waveguide in presence of the dielecric. (b) Normalized force disturbution inside the waveguide.

Figure 6.6 illustrates the force in x direction on a particle versus its position along x axis for two different frequencies. The particle position is depicted in Figure 6.6(d). When frequency changes from 0.93 THz (which is close to the resonant frequency of the grooves and lies in region A) to 0.75 THz (which is far from region A and the waveguide in it acts as a conventional rectangular waveguide) the field concentration at the opening of the grooves decreases and at the same time intensity of the field at the space between the groove increases (see Figure 6.6(b, c)), this change in field intensity results in changing the force direction which is shown in Figure 6.6(a).
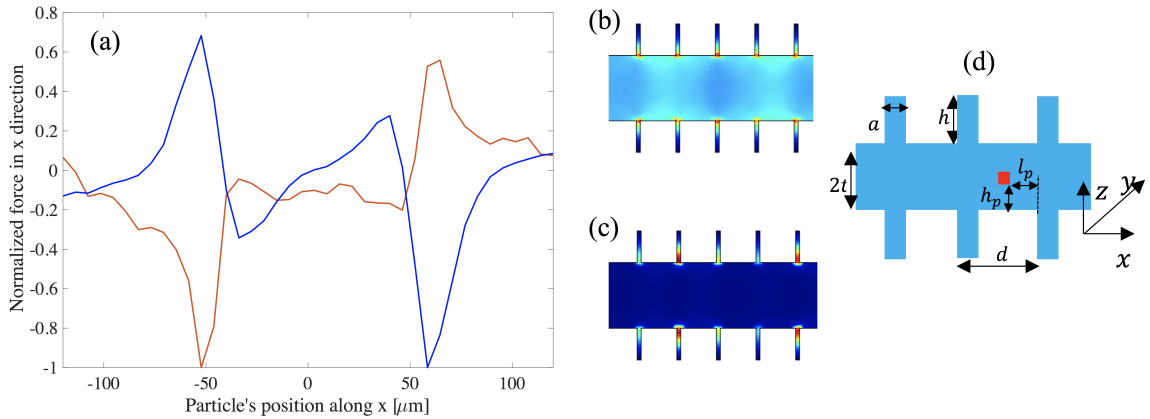
Figure 6.6: (a) Force on particle versus its position along x axis for two different frequencies, blue line for 0.93 THz and red line for 0.75 THz. (b, c) Magnitude of the electric field ($\sqrt{E_x^2 + E_y^2 + E_z^2}$) at 0.75 THz and 0.93 THz, respectively. (d) Particles position, $h_p = 12 \ \mu m$, $l_d = d/4$.

Figure 6.7 depicts the force on a particle which is placed inside the SSPP waveguide arm between the grooves opening. Operating frequency is set to 0.75 THz and the height of the groove is changed to alter the force exerted on the particle. Increasing the groove height decreases its resonant frequency which results in changing the field concentration at the opening of the grooves and the space between the groove.
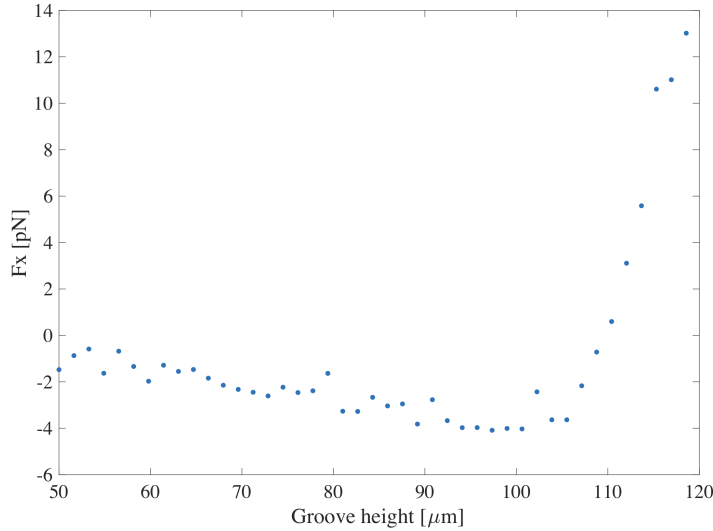
Figure 6.7: Force versus the groove height at 0.75 THz.

To changing the groove height, we can fill the groove with doped GaAs to form a Schottky contact [30], then by applying voltage across the Schottky contact, altering the depletion depth and tune the optical length of the groove. Using the results presented by Figures 6.6 and 6.7, we can propose a micro fluid pumping mechanism that can move particles inside the SSPP waveguide. Let the operating frequency be set to 0.75 THz, and the waveguide dimensions are the same as above. For a particle shown in Figure 6.8(a) by a red square, the force has a distribution shown in Figure 6.6(a) and, as the field concentration is higher between the grooves at this frequency (see Figure 6.6(b)), is directed along the -axis toward the middle of the space between the grooves. Thus, the particle is pushed into this region and takes the position as depicted in Figure 6.8(b). Now, if we increase the optical length of

the groove, this reduces the resonant frequency [see Figure 6.6 (a, c)]. As a result, the force changes sign and pushes the particle toward the opening of the grooves. When the particle reaches the opening of the groove (see Figure 6.8(c)), we restore the groove optical length to push the particle further forward.
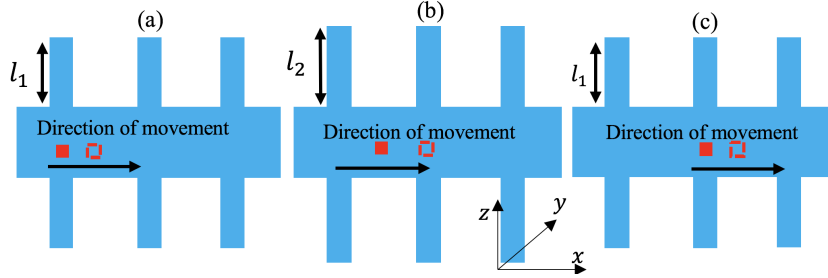
Figure 6.8: Movement of a particle inside the SSPP waveguide from (a) to (c). Solid red square represents the particle, dashed red square represents the particle destination. l_i represents the optical length of the groove ($l_1 > l_2$).

Electromagnetic force acting on a particle placed into a corrugated waveguide supporting spoof surface plasmon polaritons (SSPP) is calculated. For relatively small particles with small deviation of the value of the refractive index from environment, the force is found to be a linear function of refractive index thus indicating that the effect of the particle on SSPP can be neglected and the force can be regarded as exerted by SSPP. Since the force inside the waveguide is a function of the particle size and its refractive index, the mechanical action of SSPP can be used as a filter for fluid passing through the waveguide. Such action can separate the particles inside the fluid according to their volume and dielectric properties. A switching mechanism is proposed utilizing the variation of the force direction depending on the relation between the operating frequency and the SSPP resonance frequency, ω_p , due to interference of Bloch modes. In essence, at the middle line of the waveguide, the component of the force along the axis of the waveguide is directed away from the nearest groove, when the operating frequency is close to ω_p and toward the groove, when the operating frequency is sufficiently far from ω_p.

CHAPTER VII

High Sensitivity THz Sensor Based on Fano-Resonance Phenomenon in Metamaterial

The emerge of hidden threats such as explosives material or biological agents like anthrax have motivated researcher to delve deep into the field of sensors and their applications in detection of hazardous material. The explosives such as TNT, RDX, HMX and biochemical weapons decompose at atmospheric pressure, and as they absorb radiation in the specific electromagnetic spectrum like THz range [99], their traces in air can be used as signatures. The devices using this new technology can play a great role in improving the security measurements and providing accurate data base worldwide for sensitive gas tracing. Those data can provide sophisticated and accurate detection systems, which can challenge the growing threat in public transport, airports, and for industrial and medical applications. To identify and detect these dangerous materials, it is necessary to develop devices that can detect either the transmitted or reflected electromagnetic waves selectively. Another important application of THz wave is spectroscopy and bio-sensing. THz sensing and spectroscopy benefit from the fact that materials have unique fingerprint of spectral features in the band. THz sensors can offer high sensitivity and resolution, also because of small wavelength they can be fabricated on-chip scale [100]. With the development of terahertz time domain spectroscopy (THz-TDS) and portable terahertz

spectroscopic tool, THz sensing technology has shown great potential in highly sensitive and on-site detection/identification of minute amounts of microbial substances [101, 102, 103, 104, 105, 106, 107, 108, 109, 110, 111, 112, 113]. There are two important aspects in THz resonance sensing, one is to increase sensitivity of the sensor. Various high Q resonators, such as asymmetric split ring resonators (ASRRs) [114], $\Gamma-shaped$ resonator [115], are developed to achieve this goal. Another aspect is to reduce the amount of sample needed to characterize it. For example, a near field source is employed in [116] to focus the energy onto a tiny spot beyond the diffraction limit, which consequently reduces the amount of required sample [117]. The metamaterial biosensors play a key role in THz bio-sensing system, however, the current index of sensitivity, high Q resonance, absorption rate, interaction efficiency, readout signal and integration is still unable to meet the requirements. For non-magnetic materials, the analyte will change the whole equivalent dielectric constant by changing the capacitance of the metamaterial, finally leading to the change of the resonance frequency and amplitude. Obviously, adopting low dielectric constant, low loss and thin thickness of the metamaterial can improve the sensitivity of the sensor, and be beneficial to detecting minute perturbations in dielectric value and reducing the number of required samples molecules [116]. However, due to the weak energy storage characteristics of the monolayer metamaterial, increasing the subwavelength scale interaction between samples under investigation and terahertz wave for a sufficient sensitivity is the key scientific problems in the study of terahertz sensing. The most effective way to improve the light-matter interaction is utilizing the near filed enhancement of high Q factor resonance. There are two ways to improve the Q factor of metamaterial, first is by designing the artificial microstructure with sharp resonance peak, second is by enhancing the mutual coupling between the multilayer structures to improve the electromagnetic energy utilization ratio [118]. Beside the current advancements in the THz metamaterial sensors, the sensitivity is still limited by the weak interaction

between samples and the localized near field or the decayed resonant mode outside the cavity. While most of the terahertz sensors are based on transmission spectrum detection, the sensitivity can be greatly reduced in the case of interaction of THz wave with lossy microfluidic analyte through one-time transmission. Compared with the transmission structure, the reflective structure can provide twice interaction between the terahertz wave and the microfluidic analyte during incidence and reflection process, which is more favorable to the spatial overlap interaction.

7.1 The metamaterial absorber structures

Figure 7.1 illustrates the proposed structure for the THz sensing. It represents the device that can be used for sensing the liquid samples, they will pass through the fluid channel at the top of the sensing platform, and affects the THz resonances of the metamaterial structure and its absorption characteristics.
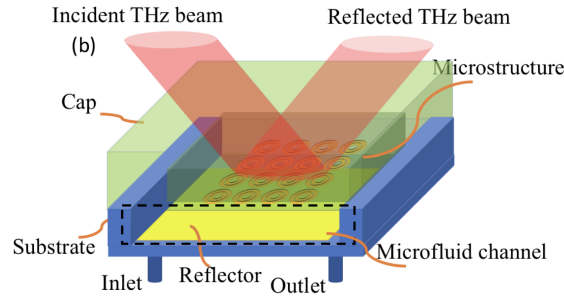
Figure 7.1: Schematic view of the proposed THz sensing platform.

The first structure that we have investigated is the metallic ring as shown in the Figure 7.2. In this design, the metamaterial absorber (MA) is composed of a periodic array of metallic rings and continuous metal film separated by dielectric substrate. The ring possesses high symmetry and can be easily fabricated. The two metallic layers strongly couple to the magnetic field of the incident wave, which exhibits a magnetic resonance. As a result, we can tune the geometric parameters of the MA to

acquire a desired magnetic resonance at the resonance frequency and achieve perfect absorption.

Figure 7.2: Schematic view of the metallic ring, dielectric refractive index is 2.1, dimensions are as $d = 100 \ \mu m, \ h = 1 \ \mu m, \ t = 6 \ \mu m, \ r = 45 \ \mu m$

In our simulation, metallic ring and metal film are made of lossy gold. The transmission is zero due to the shielding of the bottom metal film and the reflectance is the only factor determining the absorption hence the absorptivity is calculated by $A(\omega) = 1 - R(\omega) = 1 - |S(1,1)|^2$ To attain perfect absorption, we can only minimize the reflectance. Figure 7.3 illustrate the H_x and E_z, respectively. The cross product of these two represents the power flow in y-direction, there is the same situations for H_y and E_z, as the structure has symmetry respect to x and y. Then, the power flows inside the substrate, also as the E_z (see Figure 7.3) mostly exist underneath the ring, power flow happens under the ring and most of power loss happens there. If instead of the dielectric at the underneath of the ring, replacing the sample, we can have more electromagnetic fields and sample interaction and increasing the sensitivity.
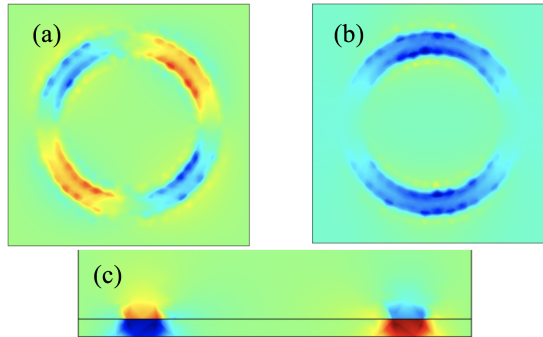
Figure 7.3: Magnitude of E_y at the top of the ring resonator, (b) Magnitude of H_x , (c) Magnitude of E_z.

Figure 7.4 depicts the absorption spectra of the ring metamaterial. The goal is to increase the sensitivity of the metamaterial sensor platform, and optimize the structure to get more information out of the sample. In order to achieve higher sensitivity, the sensor needs a sharp edge in responsive transmitted/reflective spectrum and a point of high concentration of electric field to detect small changes in the dielectric environment.
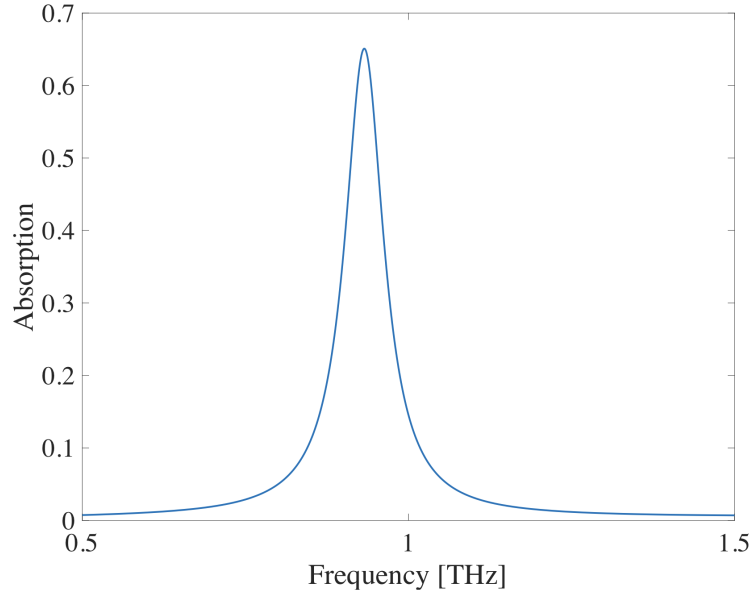
Figure 7.4: Absorption spectra of the metamaterial composed of periodic metallic ring.

The primary resonance modes of metamaterial usually have lower Q values, such as the dipole mode and LC resonance mode. The high Q resonance modes can be obtained by introducing the trapped modes or high order modes, which requires the metamaterial to support the sub-radiation modes. The sub-radiation modes usually exist in the form of dark modes, such as Fano, Quadrupole resonance and electromagnetically induced transparency (EIT) resonance [119] and [120, 121, 122, 114, 123, 124, 125, 126, 127, 128, 129], which can effectively improve the utilization of electromagnetic energy by suppressing the outward radiation filed. Resonance is an important subject in theoretical and experimental investigation of structures in physics. The

search for new effects related to wave interference and different kinds of resonances in various physical systems may be of interest. Interference of a localized wave with propagating states and resulting Fano resonances in atomic and solid-state structures have been attracting much attention recently [114, 123, 124]. In the next section, we investigate the double resonance structure with improved sensitivity. And then we improve it by introducing Fano resonance in our design.
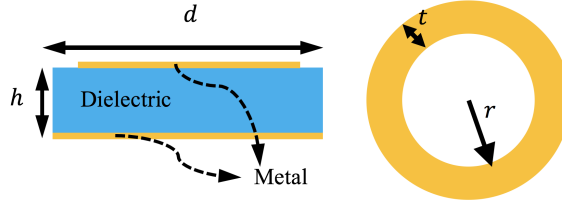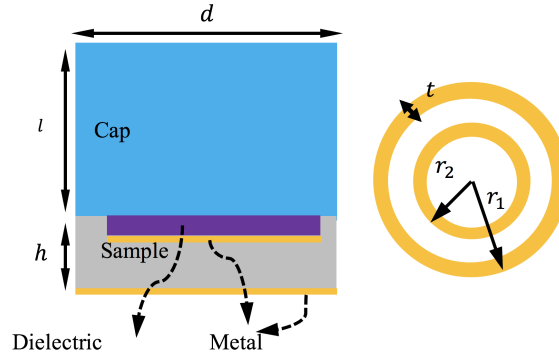

Figure 7.5: Schematic view of the metallic ring, dielectric refractive index is 2.1, dimensions are as $d = 100\ \mu m$, $h = 5\ \mu m$, $t = 6\ \mu m$, $r_1 = 45\ \mu m$, $r_1 = 45\ \mu m$.

To have double resonance feature two ring are put in each period. Terahertz multi resonant metamaterials with fractal-structure or super-cell resonators can match multiple resonance frequencies with characteristic frequencies of the analyte, providing more dielectric information of the analyte for higher sensitivity in miniaturized sensing device. Figure 7.5 illustrates the schematic view of the double resonance structure with improved sensitivity. Figure 7.6 depicts the surface current and field distributions for new structure that consists two set of ring inside each other. As seen, part of the electromagnetic energy is move to the space between the two rings, and in contrast the energy concentration in above and bottom of the ring decreases. This will result in more interaction between samples and electromagnetic fields. As the circumferences of the rings are different then their resonant frequencies are also different. To increase the sensitivity a thin layer of dielectric ring is added to the top of

the metamaterial, this will confine the electromagnetic fields concentration near the metallic rings.
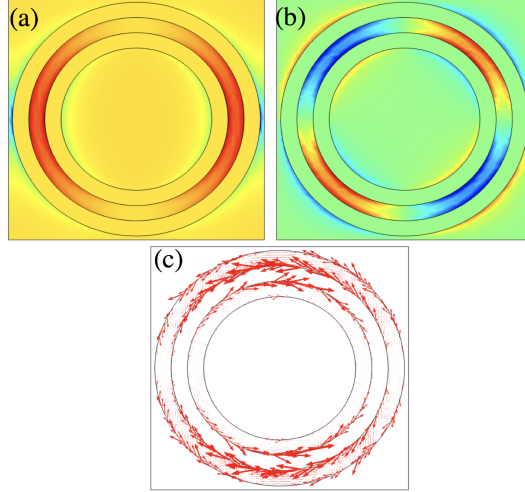
Figure 7.6: (a, b, c) E_x, E_y and surface current for double ring resonator, respectively.

Figure 7.7 shows the Absorption properties of the sensor for the three different materials with the refractive index of:$n_{Ethanol} = 1.6$, $n_{Glucose} = 2.1$, $n_{Air} = 1$. The absorption results show almost perfect absorption in the metamaterial sensor at the lower index values (under 2). In addition, the sharp resonant absorption demonstrates excellent signal to noise ratio (SNR). The sensitivity of the ring resonator for Mode A which has lower resonant frequency is 0.679 RIU^{-1} and for Mode B with higher resonant frequency is 0.727 RIU^{-1}.

7.2   Fano-Resonace based metamaterials

High-Q-factor metamaterial based on symmetric and asymmetric resonators can be traced to the excitation of the sub-radiation trapped mode. Fano-resonant meta-materials enable the strong localized EM field enhancement by bright-dark mode coupling, the asymmetric and spectrally steep line shape. By matching the spectral positions of the dark resonances with the vibrational fingerprints of the material

under investigation, quantitative characterization of weak induced perturbation in dielectric environment can be carried out. In recent years, THz Fano-resonant meta-surface bio-sensing has become a promising label-free detection technology due to its high-quality factor resonance and strong localized field absorption, interacting with analyte such as bimolecular with affinity binding, which makes a breakthrough of detection resolution limits [130]. In 2009, B. Lahiri et al. proposed an asymmetric circular split ring resonator (SRR) sensor, the enhanced plasmon resonance increases the sensitivity for different biological molecules [131]. Al-Naib et al. demonstrated a terahertz metamaterials sensor consists of SRR arrays with respect of different mutual rotation angle, revealed a high Q factor of 100 at the mergence of the sub-radiant even mode [132]. Other researchers also through utilizing high Q metamaterials, depicted high sensitivity THz sensors, their sensitivity can be as high as 7.75 x 103 nm/refractive index unit (RIU) [133].

Figure 7.8 shows the structure that supports the Fano resonance, to add Fano resonance the symmetry of the ring resonator is broken, (see Figure 7.8). Figure 7.9 represents the electric field distributions at the resonant frequency of the structure at the surface slightly at the top of the ASRR. As seen near the gap we have the highest power concentration.

The surface currents at the two resonances based on the transmission properties of Figure 7.10 are depicted in Figure 7.10. For the sharp asymmetric resonance at 0.7 THz which occurs for the first orientation, when incident electric field is perpendicular to the gap, we observe anti-parallel currents in the left and bright arcs. As the structure is weakly coupled to the free space these currents are very effective. This resonance mode is similar to the inductive capacitive (LC) resonance which can be considered in a single gap SRR. Both of these resonances lead to current configurations in which the magnetic dipole moment is perpendicular to the metamaterial plane of the array. These currents oscillate synchronously in all the ASRRs at this resonant
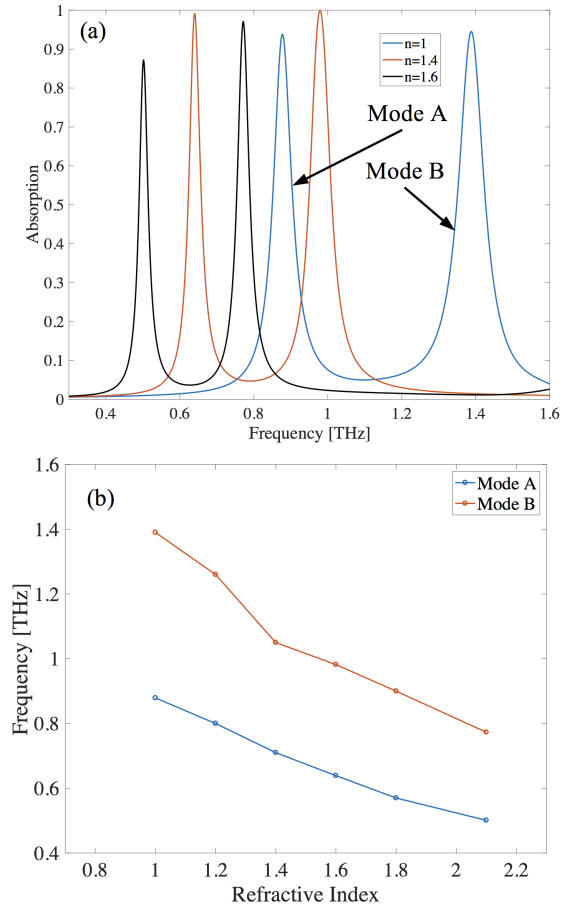
Figure 7.7: Absorption spectra for double ring resonator for three different samples.
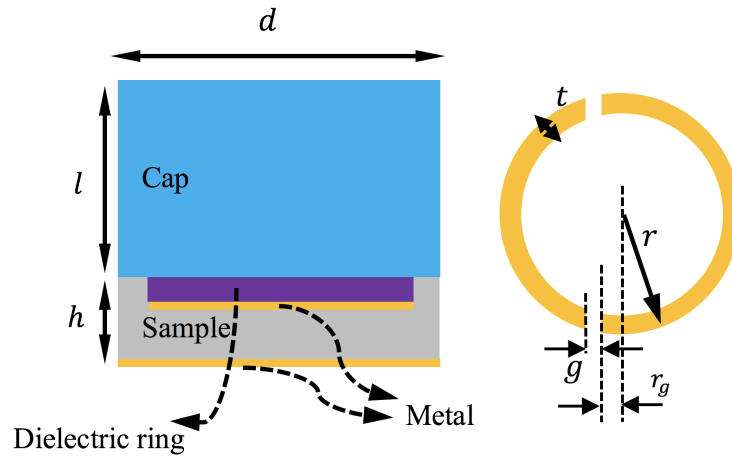
Figure 7.8: Schematic view of the metallic ring, dielectric refractive index is 2.1, dimensions are as $d = 100\ \mu m$, $h = 5\ \mu m$, $t = 6\ \mu m$, $r_1 = 45\ \mu m$, $r_1 = 45\ \mu m$, $g = 6\ \mu m$, $r_g = 4\ \mu m$

frequency. The second broad symmetric resonance at 0.9 THz is due to a dipole-like parallel current distribution as seen in the simulation.
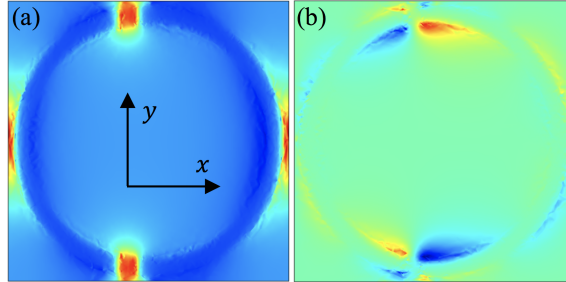
Figure 7.9: From left to right, E_x and E_y of the asymmetric ring resonator.

The high Q asymmetric Fano resonance in the ASRR arises from the structural asymmetry which results in an interference between a sharp discrete resonance and a much broader continuum-like spectrum of dipole resonance. This narrow resonance arises from a sub-radiant dark mode for which the radiation losses are completely suppressed due to the structures weak coupling to free space. Such dark modes are exploited to realize EIT-like effects in metamaterials which opens avenues for designing slow light devices with high group index. The resonance at 1.6 THz which is illustrated for the second orientation is due to dipole-like and is depicted in Figure 7.10.

As can be seen from Figure 7.11 the Fano resonance in our asymmetric metamaterial is sensitive to the polarization of the exciting field. This opens the route towards tunable devices which could base on the circular dichroism of terahertz waves mediated through a chiral arrangement of the planar metamaterial with respect to the incident terahertz field [134]. The effect of asymmetry on the Q factor of the Fano resonance is studied in [126]. It is demonstrated that the strength of the Fano resonance increases with increasing asymmetry parameter. The same is true for the width of the resonance. The sharpest resonance is observed for a small asymmetry. It should be stressed that such a high Q factor is almost an order of magnitude higher than that obtained in the regular LC resonance symmetric Lorentzian mode [135].
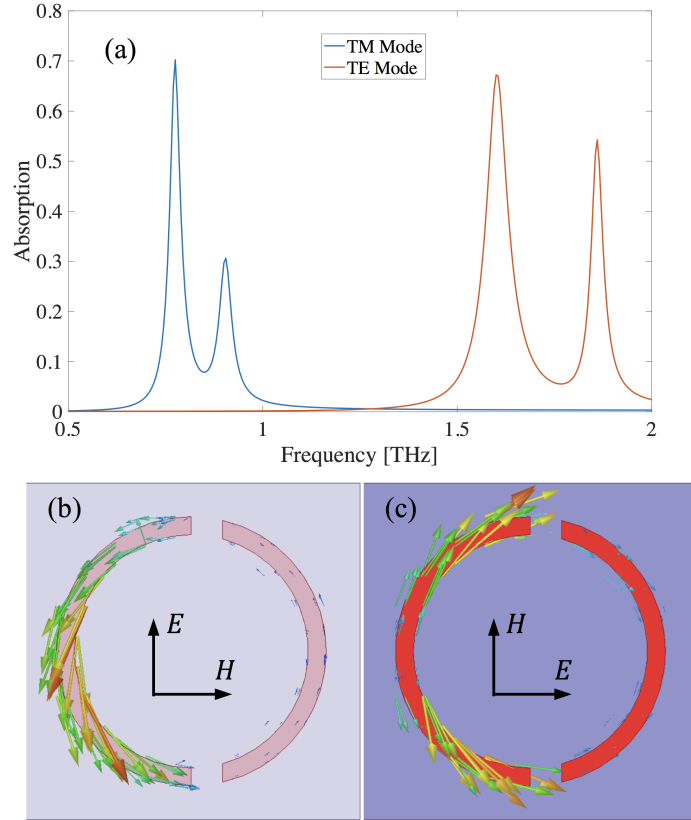
Figure 7.10: Absorption for two different polarizations. Surface current on split ring resonator for two different polarization TM and from left to right.

As asymmetry increases, the resonance broadens since the asymmetric split ring resonator (ASRR) metamaterial couples more efficiently to the free space. Figure 7.11 shows the absorption properties of the ASRR sensor for the three different materials with the refractive index of: . The sensitivity of the split ring resonator for Mode A with lower resonant frequency is $0.690 \ RIU^{-1}$ and for Mode B with higher resonant frequency is $0.758 \ RIU^{-1}$.

Figure 7.12 illustrates the current distributions for ASRR and double RR to have better understanding of their differences. The induced currents in the inner and outer rings oscillate in opposite phase, yielding an electromagnetically trapped mode. The induced currents in the split rings form a circulating current loop, yielding a subradiant mode. The E fields of trapped modes are focused either in the gaps of unit
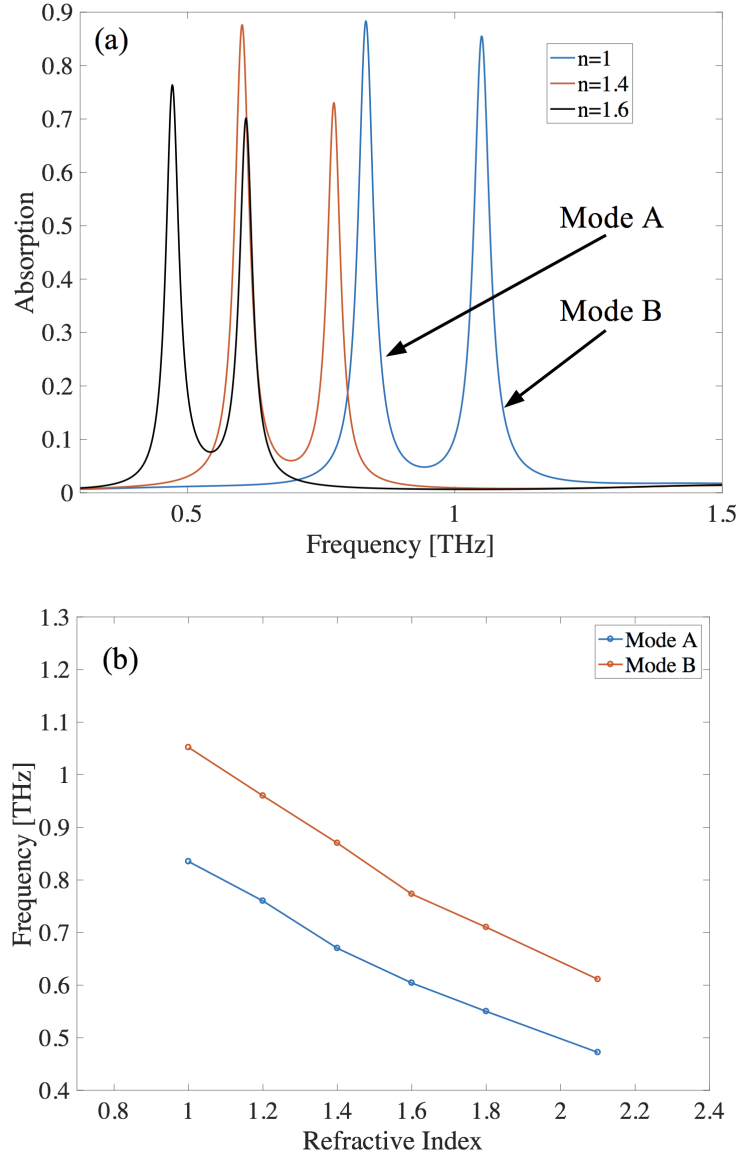
Figure 7.11: Absorption spectra for asymmetric ring resonator for three different samples.

cells or gaps between the paired rigs. Inspired by the condensed near field coupling, we innovatively present an interaction enhancing strategy of etching grooves underneath each meta-atom. Both the E fields of dipole-like modes and Fano-like modes are focused at the gaps of the split rings. These sub-radiant modes are beneficial to restrain outgoing radiation, thus improve the Q factor and sensitivity. The height of the dielectric is in subwavelength scale, resulting a transverse resonance. The current

loop forming by the on-top metamaterial and reflector ground excites the field along x direction. As a result, a strong electrically resonant component in the vertical direction is observed at the two ends of the dipole. Therefore, the calculated power flux is clearly along the y direction. The transverse resonance reduced the radiative damping rate of the resonant mode, a key factor to obtain complete absorption, which is controlled by adjusting the height of the substrate.
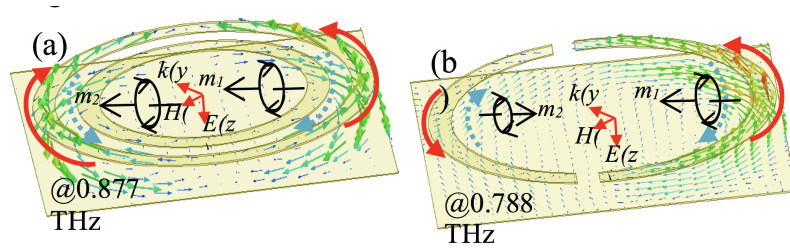
Figure 7.12: Absorption spectra for asymmetric ring resonator for three different samples.

The current state of art THz sensors are compared with the proposed sensors in Table 7.1. In recent years, a large overlap with greatly confined cavity resonance of the metamaterial perfect absorber (MPA), resulting in ultrahigh sensitivity detection, has aroused widespread concerns in the terahertz sensing research field. N. Liu et al. reported a near infrared plasmonic sensor based on narrowband perfect absorber, the detection sensitivity was 420nm/RIU [121]. In 2015, L. Cong et al. compared the sensitivity of terahertz MMs absorber and metamaterial with the same resonator, the results show that the figure of merit (FoM) was increased by an order of magnitude because the Fabry-Perot cavity significantly enhanced the EM field concentration in the absorber [122]. In 2016, X. Hu et al. presented a terahertz MPA integrated microfluidic sensor, a high sensitivity of 3.5 THz/RIU is predicted by the greatly enhanced light-matter [114]. In contrast, the multi-band sensitivity of our design sensor could be further improved by constructing stronger interaction cavity, which consists of Fano resonant meta-atoms on top cap and grooved microfluidic channel in

middle and ground reflector at bottom.

Frequency [THz]	Normalized Sensitivity $[RIU]^{-1}$	Ref	Technique
0.55	0.25	[136]	Waveguide resonance
1.5	0.17	[137]	Metal ring and graphene disk
0.5	0.08	[138]	Metamaterial
3.0	0.49	[139]	(MPA)
0.71	0.31	[140]	Mpa integrated microfluidic channel
0.77	0.73	Proposed	Trapped mode resonance
0.54	0.76	Proposed	Fan-resonance

Table 7.1: Comparison the sensitivity of the state of the art metamaterial sensors

CHAPTER VIII

Closing Remarks and Future Path

Compressing light on a subwavelength scale is one of the most promising areas of current photonics and electronics. However, it is not possible to confine the light radiated by nanometer size atoms or molecules to a lateral dimension smaller than wavelength of the light by using the conventional waveguiding methods. To overcome these challenges, plasmonics is an ideal candidate for two main reasons: first, plasmonics uses low dimensional surface waves such as 1-D and 2-D, thus miniaturizing the optical components for solving the integration limit and second, plasmonics devices provide strong light localization, thus allowing highly sensitive detection and signal transducer components. Thus, the emerging field of plasmonics strongly benefits the various areas such as near-field optics, quantum dots and optical processing.

In this dissertation, we have designed Single sided SSPP waveguide, THz switch, and THz ADC as one important building block of the THz circuitries, as already described in detail in Chapters III and IV. In that design, The SSPP structure acts as an effective interface through which the electronic input can be used as control signals, while the information is carried by the THz frequency. The Single sided SSPP structure enables THz signal propagation in slow-wave modes. These designer modes indicate the possibility of controlling the wave transmission via external stimuli. Similar ideas can be employed in the design of other THz circuitry components.

Most prominently, THz Boolean logic component designs are studied in this chapter and realized as the fundamental constituent of the future THz digital circuits. In the following we will discuss about future works regarding the fabrication of SSPP waveguides and utilizing the planar SSPP structure as a substitution to single sided SSPP waveguide.

8.1   Fabrication of SSPP components

We have developed the preliminary fabrication process technology for the SSPP structure at the Lurie Nanofabrication Facilities (LNF) of the University of Michigan. A schematic view example of the DC-SSPP components fabricated at LNF is shown in the Figure 8.1. The initial batches of the fabricated SSPP sensing structures were designed to have their input and output ports compatible with the WR-3 standard (0.431 mm by 0.863 mm). The features on such a design have dimensions as small as 180 μm. The fabrication process is a two-mask process and is described in the following.
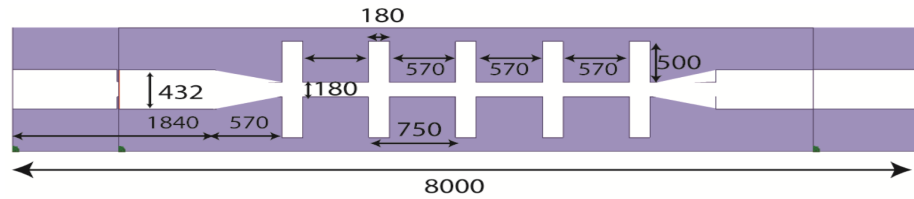
Figure 8.1: Transmission spectra of (a) unmodified DC-SSPP structure and (b) the DC-SSPP structure with narrowed waist.

The fabrication was carried out on a 4 inch Silicon wafer. The thickness of the device side is 431 μm and the back side is 250 μm thick. The Silicon dioxide layer in the middle is 0.5 μm thick, and 1 μm Silicon dioxide layers were prepared and polished on both sides of the wafer. First, the device sides of two bare polished SOI wafers were coated with a thin layer (3 μm) of photoresist. After coating, the photoresist layers were patterned and developed (Figure 8.2(a)). Then we etched the

1 μm Silicon dioxide on top of the wafers until the buried Silicon layer was exposed (Figure 8.2(b)).
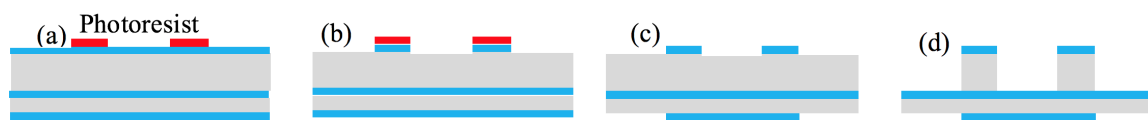
Figure 8.2: Coating with photoresist and patterning. (b) Etching Silicon dioxide. (c) Etching Silicon dioxide at back side. (d) Etching the Silicon layer.

To etch the Silicon dioxide layer, reactive-ion etching (RIE) technique was used. After that, the two wafers were stripped from the remaining photoresist using solvent or RF plasma stripper. Then, the back-sides of these two wafers were patterned using the backside mask and after developing, the 1 μm Silicon dioxide on bottom of the wafers was etched until the buried Silicon layer was exposed (Figure 8.2(c)). The next step was to etch the Silicon on the device side (Figure 8.2(d)). The deep reactive-ion etching (DRIE) technique was used in order to achieve precise dimensions. After completing wafer etching, we deposited Au on device side using physical vapor deposition (PVD). To avoid Silicon diffusion into Au which will result in a lossy alloy in THz frequencies, we deposited a thin layer $(0.5\mu m)$ of Silicon dioxide before the Au layer deposition took place (Figure 8.3(a)). Next, the two wafers were aligned and bonded together (Figure 8.3(b)).
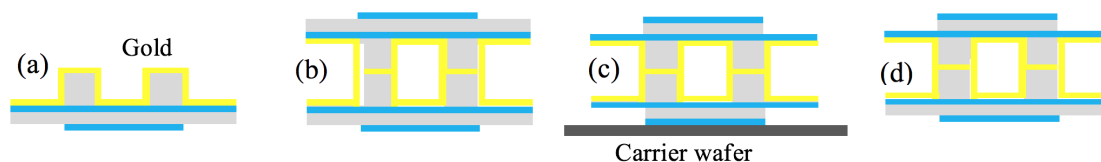
Figure 8.3: (a) Gold deposition. (b) Bonding. (c) Etching the Silicon at the top of wafer. (d) Mounting to carrier wafer and etching the remaining Silicon.

The final step was to etch the top and bottom of bonded wafers (Figure 8.3(c)).

At first one side was etched until buried Silicon dioxide layer. It was flipped and mounted to a carrier wafer and the other side was etched to the Silicon dioxide layer. The remaining Silicon dioxide layers were about $1\mu m$ thick. To separate the parts, we had put them in hot water ($80°C$). Then the crystal bonds were dissolved in water to allow the final components to float (Figure 8.3(d)).
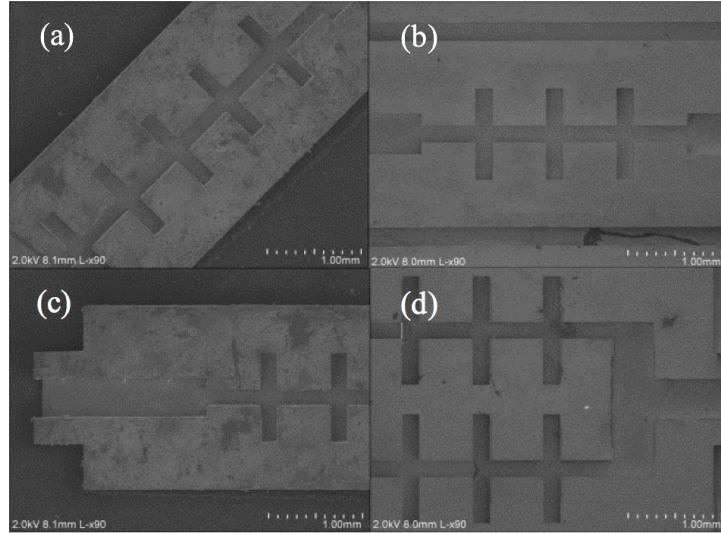
Figure 8.4: (a) SSPP waveguide with five corrugations. (b) SSPP waveguide with 3 corrugations. (c) SSPP waveguide and the WR3 feed point. (d) Mach-Zehnder interferometer.

The SEM images of the final SSPP components are shown at Figure 8.4 and Figure 8.5 show the final components.

An important finding from our preliminary work is that the metal deposition plays critical role in the fabrication flow. Lack of metal on the surface of the silicon waveguide will introduce serious loss in slow EM wave propagation inside DC-SSPP device. It will also break the boundary conditions under which the SSPP resonance would occur. The vertical walls of the grooves are the places where metal deposition is hardest to control. In the initial batches, gold evaporating technique was used for deposition with unsatisfactory evenness. We plan to replace it with gold sputtering technique in the following batches and the outcome will be evaluated. Bonding is

Figure 8.5: Fabricated SSPP components; in the left corner: halves of the SSPP components is shown to illustrate the grooves.

another critical step that we need to further optimize. There are two parameters (temperature, pressure) that can affect the bonding process. For example, increasing the pressure tends to crack the samples, while reducing the pressure results in many un-bonded or weak-bonded components. Such effects can be alleviated to some extent by increasing the gold thickness inside the waveguide, while thick gold deposition may result in unevenness on the bonded edges. We plan to adjust the gold thickness along with the temperature and pressure during the bonding. This may require several runs on different fabrication batches to find the optimized recipe of the three parameters.
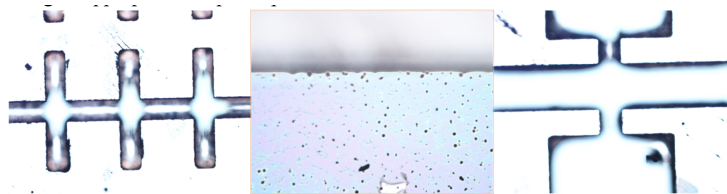
Figure 8.6: Photo of the samples during the DRIE etch.

Figure 8.6 shows that during the Silicon etching process, some small holes appear on the Silicon surface during the Silicon etching process. These holes result in uneven surface, and ultimately will generate loss in the THz transmission. To overcome the

challenges posed by dirts, we need to do more cleaning process before the DRIE process and doing plasma etch to completely cleaning the Silicon surface from any photoresist or organic compound that can prevent from Silicon etch. Figure 8.7 shows the SEM image of some components right after the DRIE. It shows unwanted Silicon on the wafer. To get rid of it, we can use DRIE for a longer time to etch them all the way, but increasing the etching time can result in undercut and even damage to the Oxide layer. To solve these problems, we need to work on DRIE recipe and Oxygen plasma etch. The other challenges we anticipate include the uneven etch of the Silicon. The recipe that is normally used for the DRIE, also etches the Silicon at high rate and etches the Silicon dioxide at very slow rate. But the etch rate may vary on the wafer and also it changes with the temperature. Our observation shows that the etch rate at the center of the wafer is higher than the corners, and at some places the Oxide layer etches completely causing damage to the samples. To decrease the etch rate of the silicon dioxide we should work on the DRIE recipe to increase its selectivity between Silicon and Silicon dioxide. Also, to reduce the heat effect on the wafer, we can divide the etch time and performing Silicon etch in several steps to let the wafer cool down.

8.2 Planar SSPP structures

The inception of spoof surface plasmon polariton (SSPP) metamaterial made it possible to manage light beyond diffraction limit at a designer specified frequency. Originally proposed and theorized as a 3D structure, about a decade later, a thin film planar version of the metamaterial supporting spoof plasmon, more amenable to fabrication, was demonstrated to inherit the similar dispersion property. Regrettably, all the demonstration in planar structure have not been accompanied with a comprehensive closed-form theory. We bridged the gap in the existing theory of spoof plasmon, and analyzed the prospect of exploiting this unconventional optical mode as
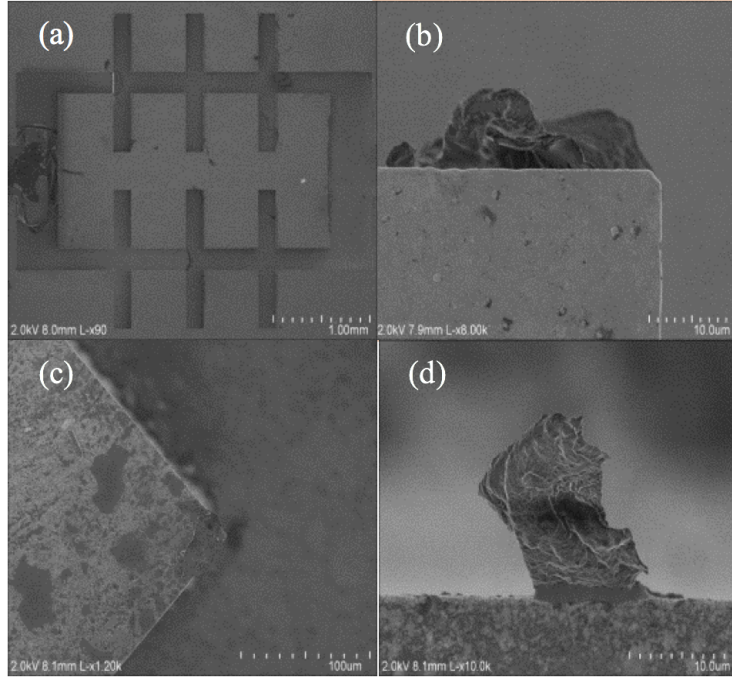
Figure 8.7: SEM image of damaged fabricated samples.

high speed intra-chip data transfer media. Through the simple yet powerful formalism built-up, we are the first to explain a number of important characteristics of spoof plasmon mode; such as, evanescent mode profile across the waveguide that explains the red-shift of band with reduction of waveguide's cross-section, and showed how these properties can be leveraged to design cross-talk suppressive data-transfer channels. In particular, the questions of acceleration of the bandwidth modulation rate of SSPP mode by external perturbation, choice of appropriate geometry to optimize the SSPP bandwidth density are addressed.

Despite Single sided SSPP deemed as a brilliant solution, the very large cross-sectional size (ideally infinite) of the metamaterial as originally proposed posed a tremendous challenge to fabricate the 3D SSPP structure and to mold it for engineering applications, in particular data processing and routing. The 3D structures possess considerably large thickness (ideally infinite), which makes it difficult to fabricate. On the contrary, a 2D SSPP structure with nominal thickness is not only
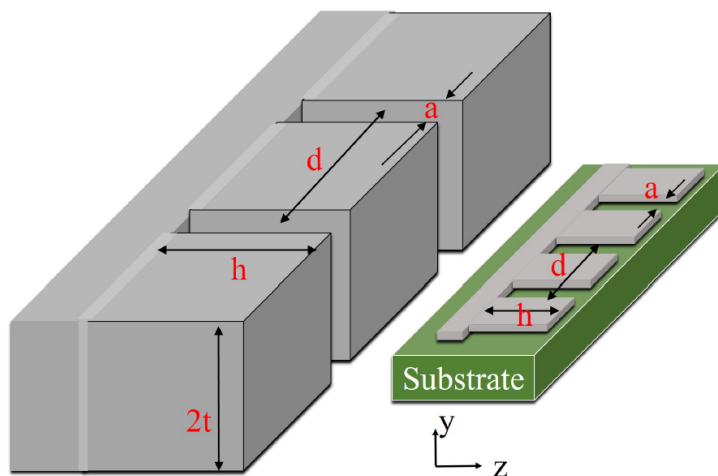
Figure 8.8: Schematics of a 3D SSPP structure standing alone and a 2D SSPP structure on substrate.

amiable to fabrication on a substrate, but also possess interesting properties that we can harness for efficient mode excitation, and bandwidth modulation.

BIBLIOGRAPHY

BIBLIOGRAPHY

[1] James Hardy and Joseph Shamir. Optics inspired logic architecture. *Opt. Express*, 15(1):150–165, Jan 2007.

[2] Anatol Khilo, Steven J Spector, Matthew E Grein, Amir H Nejadmalayeri, Charles W Holzwarth, Michelle Y Sander, Marcus S Dahlem, Michael Y Peng, Michael W Geis, Nicole A DiLello, et al. Photonic adc: overcoming the bottleneck of electronic jitter. *Optics Express*, 20(4):4454–4469, 2012.

[3] Henry Taylor. An optical analog-to-digital converter-design and analysis. *IEEE Journal of Quantum Electronics*, 15(4):210–216, 1979.

[4] Vilson R Almeida, Carlos A Barrios, Roberto R Panepucci, and Michal Lipson. All-optical control of light on silicon chip. *Nature*, 431(7012):1081, 2004.

[5] Qianfan Xu and Michal Lipson. All-optical logic based on silicon micro-ring resonators. *Optics express*, 15(3):924–929, 2007.

[6] Ch Fattinger and D Grischkowsky. Terahertz beams. *Applied Physics Letters*, 54(6):490–492, 1989.

[7] D Krökel, D Grischkowsky, and MB Ketchen. Subpicosecond electrical pulse generation using photoconductive switches with long carrier lifetimes. *Applied Physics Letters*, 54(11):1046–1047, 1989.

[8] Martin Van Exter, Ch Fattinger, and D Grischkowsky. High-brightness terahertz beams characterized with an ultrafast detector. *Applied Physics Letters*, 55(4):337–339, 1989.

[9] Michael Dyakonov and Michael Shur. Shallow water analogy for a ballistic field effect transistor: New mechanism of plasma wave generation by dc current. *Physical review letters*, 71(15):2465, 1993.

[10] Mikhail Dyakonov and Michael Shur. Detection, mixing, and frequency multiplication of terahertz radiation by two-dimensional electronic fluid. *IEEE transactions on electron devices*, 43(3):380–387, 1996.

[11] Wojciech Knap, Mikhail Dyakonov, Dominique Coquillat, Frederic Teppe, Nina Dyakonova, Jerzy Łusakowski, Krzysztof Karpierz, Maciej Sakowicz, Gintaras Valusis, Dalius Seliuta, et al. Field effect transistors for terahertz detection:

Physics and first imaging applications. *Journal of Infrared, Millimeter, and Terahertz Waves*, 30(12):1319–1337, 2009.

[12] Christian Jansen, Steffen Wietzke, Ole Peters, Maik Scheller, Nico Vieweg, Mohammed Salhi, Norman Krumbholz, Christian Jördens, Thomas Hochrein, and Martin Koch. Terahertz imaging: applications and perspectives. *Applied optics*, 49(19):E48–E57, 2010.

[13] P Uhd Jepsen, David G Cooke, and Martin Koch. Terahertz spectroscopy and imaging–modern techniques and applications. *Laser & Photonics Reviews*, 5(1):124–166, 2011.

[14] L Vicarelli, MS Vitiello, D Coquillat, A Lombardo, AC Ferrari, W Knap, M Polini, V Pellegrini, and A Tredicucci. Graphene field effect transistors as room-temperature terahertz detectors. *arXiv preprint arXiv:1203.3232*, 2012.

[15] Peter H Siegel. Terahertz technology in biology and medicine. *IEEE transactions on microwave theory and techniques*, 52(10):2438–2447, 2004.

[16] Masayoshi Tonouchi. Cutting-edge terahertz technology. *Nature photonics*, 1(2):97–105, 2007.

[17] Joseph Wang and Evgeny Katz. Digital biosensors with built-in logic for biomedical applications?biosensors based on a biocomputing concept. *Analytical and bioanalytical chemistry*, 398(4):1591–1603, 2010.

[18] Mike Kemp. Screening mail for powders using terahertz technology. In *SPIE Security+ Defence*, pages 81890J–81890J. International Society for Optics and Photonics, 2011.

[19] Yongmei Jia, Ruixue Duan, Fan Hong, Boya Wang, Nannan Liu, and Fan Xia. Electrochemical biocomputing: a new class of molecular-electronic logic devices. *Soft Matter*, 9(29):6571–6577, 2013.

[20] F Coppinger, AS Bhushan, and B Jalali. Photonic time stretch and its application to analog-to-digital conversion. *IEEE Transactions on microwave theory and techniques*, 47(7):1309–1314, 1999.

[21] Michael J Hayduk, Rebecca J Bussjager, and Mark A Getbehead. Photonic analog-to-digital conversion techniques using semiconductor saturable absorbers. In *Proc. SPIE*, volume 4042, pages 54–60, 2000.

[22] Henry Zmuda, Edward N Toughlian, Guifang Li, and Patrick LiKamWa. A photonic wideband analog-to-digital converter. In *Aerospace Conference, 2001, IEEE Proceedings.*, volume 3, pages 3–1461. IEEE, 2001.

[23] C Pala, L Thylen, M Mokhtari, and U Westergren. A high-speed electro-optical analog-to-digital converter principle. In *Circuits and Systems, 2001. ISCAS 2001. The 2001 IEEE International Symposium on*, volume 1, pages 432–435. IEEE, 2001.

[24] Yuanliang Zhang, Yao Zhang, and Baojun Li. Optical switches and logic gates based on self-collimated beams in two-dimensional photonic crystals. *Optics Express*, 15(15):9287–9292, 2007.

[25] Jing Xu, Xinliang Zhang, Yin Zhang, Jianji Dong, Deming Liu, and Dexiu Huang. Reconfigurable all-optical logic gates for multi-input differential phase-shift keying signals: design and experiments. *Journal of Lightwave Technology*, 27(23):5268–5275, 2009.

[26] Hong Wei, Zhuoxian Wang, Xiaorui Tian, Mikael Käll, and Hongxing Xu. Cascaded logic gates in nanophotonic plasmon networks. *Nature Communications*, 2:387, 2011.

[27] Yulan Fu, Xiaoyong Hu, Cuicui Lu, Song Yue, Hong Yang, and Qihuang Gong. All-optical logic gates based on nanoscale plasmonic slot waveguides. *Nano letters*, 12(11):5784–5790, 2012.

[28] Kanglin Wang and Daniel M Mittleman. Metal wires for terahertz wave guiding. *Nature*, 432(7015):376, 2004.

[29] Andrea G Markelz. Terahertz dielectric sensitivity to biomolecular structure and function. *IEEE Journal of Selected Topics in Quantum Electronics*, 14(1):180–190, 2008.

[30] Zhao Xu. *Terahertz (THz) Waveguiding Architecture Featuring Doubly-Corrugated Spoofed Surface Plasmon Polariton (DC-SSPP): Theory and Applications in Micro-Electronics and Sensing.* dissertation, University of Michigan, 2017.

[31] Christopher R Williams, Steven R Andrews, SA Maier, AI Fernández-Domínguez, L Martín-Moreno, and FJ García-Vidal. Highly confined guiding of terahertz surface plasmon polaritons on structured metal surfaces. *Nature Photonics*, 2(3):175–179, 2008.

[32] Mufei Gong, Tae-In Jeon, and D Grischkowsky. Thz surface wave collapse on coated metal surfaces. *Optics express*, 17(19):17088–17101, 2009.

[33] Tae-In Jeon and Da Grischkowsky. Thz zenneck surface wave (thz surface plasmon) propagation on a metal sheet. *Applied physics letters*, 88(6):061113, 2006.

[34] G Gallot, SP Jamison, RW McGowan, and D Grischkowsky. Terahertz waveguides. *JOSA B*, 17(5):851–863, 2000.

[35] Victoria Astley, Julianna Scheiman, Rajind Mendis, and Daniel M Mittleman. Bending and coupling losses in terahertz wire waveguides. *Optics letters*, 35(4):553–555, 2010.

[36] Fuzi Yang, JR Sambles, and GW Bradberry. Long-range surface modes supported by thin films. *Physical Review B*, 44(11):5855, 1991.

[37] SP Jamison, RW McGowan, and D Grischkowsky. Single-mode waveguide propagation and reshaping of sub-ps terahertz pulses in sapphire fibers. *Applied physics letters*, 76(15):1987–1989, 2000.

[38] FJ Garcia-Vidal, L Martin-Moreno, and JB Pendry. Surfaces with holes in them: new plasmonic metamaterials. *Journal of optics A: Pure and applied optics*, 7(2):S97, 2005.

[39] AI Fernandez-Dominguez, L Martin-Moreno, FJ Garcia-Vidal, Steven R Andrews, and SA Maier. Spoof surface plasmon polariton modes propagating along periodically corrugated wires. *IEEE Journal of Selected Topics in Quantum Electronics*, 14(6):1515–1521, 2008.

[40] Fuli Zhang, Qian Zhao, Lei Kang, Davy P Gaillot, Xiaopeng Zhao, Ji Zhou, and Didier Lippens. Magnetic control of negative permeability metamaterials based on liquid crystals. *Applied Physics Letters*, 92(19):193104, 2008.

[41] Zhen Gao, Xufeng Zhang, and Linfang Shen. Wedge mode of spoof surface plasmon polaritons at terahertz frequencies. *J. Appl. Phys.*, 108(11), 2010.

[42] Yong-qiang Liu, Ling-bao Kong, and Pu-kun Liu. Long-range spoof surface plasmons on the doubly corrugated metal surfaces. *Opt. Commun.*, 370:13–17, 2016.

[43] Liangliang Liu, Zhuo Li, Changqing Gu, Pingping Ning, Bingzheng Xu, Zhenyi Niu, and Yongjiu Zhao. Multi-channel composite spoof surface plasmon polaritons propagating along periodically corrugated metallic thin films. *J. Appl. Phys.*, 116(1), 2014.

[44] Yong Jin Zhou, Qian Xun Xiao, and Bao Jia Yang. Spoof localized surface plasmons on ultrathin textured MIM ring resonator with enhanced resonances. *Sci. Rep.*, 5(September):14819, 2015.

[45] Tao Jiang, Linfang Shen, Xufeng Zhang, and Li-Xin Ran. HIGH-ORDER MODES OF SPOOF SURFACE PLASMON POLARITONS ON PERIODICALLY CORRUGATED METAL SURFACES, 2009.

[46] A. I. Fernández-Dománguez, L. Martín-Moreno, F. J. García-Vidal, S. R. Andrews, and S. A. Maier. Spoof surface plasmon polariton modes propagating along periodically corrugated wires. *IEEE J. Sel. Top. Quantum Electron.*, 14(6):1515–1521, 2008.

[47] Xiaoyong Liu, Yijun Feng, Bo Zhu, Junming Zhao, and Tian Jiang. High-order modes of spoof surface plasmonic wave transmission on thin metal film structure. *Opt. Express*, 21(25):31155–31165, 2013.

[48] Binggang Xiao, Jing Chen, and Sheng Kong. Filters based on spoof surface plasmon polaritons composed of planar Mach?Zehnder interferometer. *J. Mod. Opt.*, 0340(March):1–4, 2016.

[49] Zhen Gao, Fei Gao, Youming Zhang, Xihang Shi, Zhaoju Yang, and Baile Zhang. Experimental demonstration of high-order magnetic localized spoof surface plasmons. *Appl. Phys. Lett.*, 107(4):1–5, 2015.

[50] Hao Chi Zhang, Tie Jun Cui, Qian Zhang, Yifeng Fan, and Xiaojian Fu. Breaking the Challenge of Signal Integrity Using Time-Domain Spoof Surface Plasmon Polaritons. *ACS Photonics*, 2(9):1333–1340, 2015.

[51] Hui Feng Ma, Xiaopeng Shen, Qiang Cheng, Wei Xiang Jiang, and Tie Jun Cui. Broadband and high-efficiency conversion from guided waves to spoof surface plasmon polaritons. *Laser Photonics Rev.*, 8(1):146–151, 2014.

[52] Xiaopeng Shen and Tie Jun Cui. Ultrathin plasmonic metamaterial for spoof localized surface plasmons. *Laser Photonics Rev.*, 8(1):137–145, 2014.

[53] Zhen Liao, Bai Cao Pan, Xiaopeng Shen, and Tie Jun Cui. Multiple Fano resonances in spoof localized surface plasmons. *Opt. Express*, 22(13):15710–7, 2014.

[54] Mikhail A. Kats, David Woolf, Romain Blanchard, Nanfang Yu, and Federico Capasso. Spoof plasmon analogue of metal-insulator-metal waveguides. *Opt. Express*, 19(16):14860, 2011.

[55] Kyungjun Song and Pinaki Mazumder. Active terahertz spoof surface plasmon polariton switch comprising the perfect conductor metamaterial. *IEEE Transactions on Electron Devices*, 56(11):2792–2799, 2009.

[56] Kyungjun Song and Pinaki Mazumder. Dynamic terahertz spoof surface plasmon–polariton switch based on resonance and absorption. *IEEE Transactions on electron devices*, 58(7):2172–2176, 2011.

[57] Zhao Xu, Kyungjun Song, and Pinaki Mazumder. Analysis of doubly corrugated spoof surface plasmon polariton (dc-sspp) structure with sub-wavelength transmission at thz frequencies. *IEEE Transactions on Terahertz Science and Technology*, 2(3):345–354, 2012.

[58] HFSS Ansoft. Ansys inc. *Pittsburg, PA*, 2013.

[59] Yinghao Yuan, Jian He, Jinsong Liu, and Jianquan Yao. Electrically controlled broadband thz switch based on liquid-crystal-filled multi-layer metallic grating structures. In *Journal of Physics: Conference Series*, volume 276, page 012228. IOP Publishing, 2011.

[60] Tarek A Ibrahim, W Cao, Y Kim, J Li, J Goldhar, P-T Ho, and Chi H Lee. Lightwave switching in semiconductor microring devices by free carrier injection. *Journal of lightwave technology*, 21(12):2997, 2003.

[61] Qianfan Xu, Bradley Schmidt, Sameer Pradhan, and Michal Lipson. Micrometre-scale silicon electro-optic modulator. *nature*, 435(7040):325, 2005.

[62] Qianfan Xu, Sasikanth Manipatruni, Brad Schmidt, Jagat Shakya, and Michal Lipson. 12.5 gbit/s carrier-injection-based silicon micro-ring silicon modulators. *Optics express*, 15(2):430–436, 2007.

[63] Sadao Adachi. *Optical properties of crystalline and amorphous semiconductors: Materials and fundamental principles.* Springer Science & Business Media, 2012.

[64] Michael Shur. *Introduction to electronic devices.* J. Wiley, 1996.

[65] Wonjoo Suh, Zheng Wang, and Shanhui Fan. Temporal coupled-mode theory and the presence of non-orthogonal modes in lossless multimode cavities. *IEEE Journal of Quantum Electronics*, 40(10):1511–1518, 2004.

[66] Shanhui Fan, Wonjoo Suh, and JD Joannopoulos. Temporal coupled-mode theory for the fano resonance in optical resonators. *JOSA A*, 20(3):569–572, 2003.

[67] Kerry J Vahala. Optical microcavities. *nature*, 424(6950):839, 2003.

[68] Mona Jarrahi, R Fabian W Pease, David AB Miller, and Thomas H Lee. Optical spatial quantization for higher performance analog-to-digital conversion. *IEEE Transactions on Microwave Theory and Techniques*, 56(9):2143–2150, 2008.

[69] Zhao Xu and Pinaki Mazumder. Terahertz beam steering with doped gaas phase modulator and a design of spatial-resolved high-speed terahertz analog-to-digital converter. *IEEE Transactions on Electron Devices*, 61(6):2195–2202, 2014.

[70] Mikhail Erementchouk, Soumitra Roy Joy, and Pinaki Mazumder. Electrodynamics of spoof plasmons in periodically corrugated waveguides. In *Proc. R. Soc. A*, volume 472, page 20160616. The Royal Society, 2016.

[71] RF Harrington. Time-harmonic electromagnetic fields/harrington rf–new-york, 2001.

[72] Warren L Stutzman and Gary A Thiele. *Antenna theory and design.* John Wiley & Sons, 2012.

[73] Islam A Eshrah, Ahmed A Kishk, Alexander B Yakovlev, and Allen W Glisson. Rectangular waveguide with dielectric-filled corrugations supporting backward waves. *IEEE transactions on microwave theory and techniques*, 53(11):3298–3304, 2005.

[74] R Rodríguez-Berral, Francisco Mesa, and Francisco Medina. Analytical model for tm scattering of 1-d narrow slit gratings loaded with dielectric slabs. In *Antennas and Propagation (EUCAP), 2012 6th European Conference on*, pages 3089–3093. IEEE, 2012.

[75] Rüdeger Köhler, Alessandro Tredicucci, Fabio Beltram, Harvey E Beere, Edmund H Linfield, A Giles Davies, David A Ritchie, Rita C Iotti, and Fausto Rossi. Terahertz semiconductor-heterostructure laser. *Nature*, 417(6885):156–159, 2002.

[76] Keith S Champlin and Gadi Eisenstein. Cutoff frequency of submillimeter schottky-barrier diodes. *IEEE Transactions on Microwave Theory and Techniques*, 26(1):31–34, 1978.

[77] A Van Der Ziel. Infrared detection and mixing in heavily doped schottky-barrier diodes. *Journal of Applied Physics*, 47(5):2059–2068, 1976.

[78] Christopher C Homes, G Lawrence Carr, Ricardo PSM Lobo, Joseph D LaVeigne, and David B Tanner. Silicon beam splitter for far-infrared and terahertz spectroscopy. *Applied optics*, 46(32):7884–7888, 2007.

[79] Christopher W Berry and Mona Jarrahi. Broadband terahertz polarizing beam splitter on a polymer substrate. *Journal of Infrared, Millimeter, and Terahertz Waves*, 33(2):127–130, 2012.

[80] Tiaoming Niu, Withawat Withayachumnankul, Aditi Upadhyay, Philipp Gutruf, Derek Abbott, Madhu Bhaskaran, Sharath Sriram, and Christophe Fumeaux. Terahertz reflectarray as a polarizing beam splitter. *Optics express*, 22(13):16148–16160, 2014.

[81] Brian D McVey, Mark A Basten, John H Booske, Jurianto Joe, and John E Scharer. Analysis of rectangular waveguide-gratings for amplifier applications. *IEEE Transactions on microwave theory and techniques*, 42(6):995–1003, 1994.

[82] David M Pozar. *Microwave engineering.* John Wiley & Sons, 2009.

[83] WHP Pernice, Mo Li, King Yan Fong, and Hong X Tang. Modeling of the optical force between propagating lightwaves in parallel 3d waveguides. *Optics express*, 17(18):16032–16037, 2009.

[84] Xudong Cui, Daniel Erni, and Christian Hafner. Optical forces on metallic nanoparticles induced by a photonic nanojet. *Opt. Express*, 16(18):13560–13568, Sep 2008.

[85] AJ Hallock, PL Redmond, and LE Brus. Optical forces between metallic particles. *Proceedings of the National Academy of Sciences of the United States of America*, 102(5):1280–1284, 2005.

[86] Michelle L Povinelli, Steven G Johnson, Marko Lončar, Mihai Ibanescu, Elizabeth J Smythe, Federico Capasso, and JD Joannopoulos. High-q enhancement of attractive and repulsive optical forces between coupled whispering-gallery-mode resonators. *Optics express*, 13(20):8286–8295, 2005.

[87] Michelle L Povinelli, Marko Lončar, Mihai Ibanescu, Elizabeth J Smythe, Steven G Johnson, Federico Capasso, and John D Joannopoulos. Evanescent-wave bonding between optical waveguides. *Optics letters*, 30(22):3042–3044, 2005.

[88] Xiaodong Yang, Yongmin Liu, Rupert F Oulton, Xiaobo Yin, and Xiang Zhang. Optical forces in hybrid plasmonic waveguides. *Nano Letters*, 11(2):321–328, 2011.

[89] MI Antonoyiannakis and JB Pendry. Electromagnetic forces in photonic crystals. *Physical Review B*, 60(4):2363, 1999.

[90] David Woolf, Mikhail A Kats, and Federico Capasso. Spoof surface plasmon waveguide forces. *Optics letters*, 39(3):517–520, 2014.

[91] Hideaki Taniyama, Masaya Notomi, Eiichi Kuramochi, Takayuki Yamamoto, Yutaka Yoshikawa, Yoshio Torii, and Takahiro Kuga. Strong radiation force induced in two-dimensional photonic crystal slab cavities. *Physical Review B*, 78(16):165129, 2008.

[92] TA Nieminen, H Rubinsztein-Dunlop, and NR Heckenberg. Calculation and optical measurement of laser trapping forces on non-spherical particles. *Journal of Quantitative Spectroscopy and Radiative Transfer*, 70(4):627–637, 2001.

[93] JR Arias-González and M Nieto-Vesperinas. Optical forces on small particles: attractive and repulsive nature and plasmon-resonance conditions. *JOSA A*, 20(7):1201–1209, 2003.

[94] Arthur Ashkin, James M Dziedzic, JE Bjorkholm, and Steven Chu. Observation of a single-beam gradient force optical trap for dielectric particles. *Optics letters*, 11(5):288–290, 1986.

[95] PC Chaumet and M Nieto-Vesperinas. Electromagnetic force on a metallic particle in the presence of a dielectric surface. *Physical Review B*, 62(16):11185, 2000.

[96] PC Chaumet and M Nieto-Vesperinas. Time-averaged total force on a dipolar sphere in an electromagnetic field. *Optics letters*, 25(15):1065–1067, 2000.

[97] Maria Dienerowitz, Michael Mazilu, and Kishan Dholakia. Optical manipulation of nanoparticles: a review. *Journal of Nanophotonics*, 2(1):021875–021875, 2008.

[98] John David Jackson. *Classical electrodynamics*. John Wiley & Sons, 2007.

[99] Jimmie C Oxley, James L Smith, Kajal Shinde, and Jesse Moran. Determination of the vapor density of triacetone triperoxide (tatp) using a gas chromatography headspace technique. *Propellants, Explosives, Pyrotechnics*, 30(2):127–130, 2005.

[100] Vaishali Rawat, Rohini Kitture, Dimple Kumari, Harsh Rajesh, Shaibal Banerjee, and SN Kale. Hazardous materials sensing: An electrical metamaterial approach. *Journal of Magnetism and Magnetic Materials*, 415:77–81, 2016.

[101] Federico Sebastiani, Stefan L. P. Wolf, Benjamin Born, Trung Quan Luong, Helmut Cölfen, Denis Gebauer, and Martina Havenith. Water Dynamics from THz Spectroscopy Reveal the Locus of a Liquid-Liquid Binodal Limit in Aqueous CaCO $_3$ Solutions. *Angew. Chemie Int. Ed.*, pages 490–495, 2016.

[102] Ruoyu Li, Carmine D'Agostino, James McGregor, Michael D. Mantle, J. Axel Zeitler, and Lynn F. Gladden. Mesoscopic structuring and dynamics of alcohol/water solutions probed by terahertz time-domain spectroscopy and pulsed field gradient nuclear magnetic resonance. *J. Phys. Chem. B*, 118(34):10156–10166, 2014.

[103] Uwe S. Pracht, Julian Simmendinger, Martin Dressel, Ryota Endo, Tatsuya Watashige, Yousuke Hanaoka, Masaaki Shimozawa, Takahito Terashima, Takasada Shibauchi, Yuji Matsuda, and Marc Scheffler. Charge carrier dynamics of the heavy-fermion metal CeCoIn5 probed by THz spectroscopy. *J. Magn. Magn. Mater.*, 400:31–35, 2016.

[104] W-J Jin, K Zhao, C Yang, C-H Xu, H Ni, and C-H Chen. Experimental measurements of water content in crude oil emulsions by terahertz time-domain spectroscopy. *Appl. Geophys.*, 10(4):506–409, 2013.

[105] a Tomasino, a Parisi, S Stivala, P Livreri, a C Cino, a C Busacca, M Peccianti, and R Morandotti. Wideband THz time domain spectroscopy based on optical rectification and electro-optic sampling. *Sci. Rep.*, 3:3116, 2013.

[106] Francesco D'Angelo, Zoltán Mics, Mischa Bonn, and Dmitry Turchinovich. Ultra-broadband THz time-domain spectroscopy of common polymers using THz air photonics. *Opt. Express*, 22(10):12475–12485, 2014.

[107] J. Tasseva, A. Taschin, P. Bartolini, J. Striova, R. Fontana, and R. Torre. Thin layered drawing media probed by THz time-domain spectroscopy. *R. Soc. Chem. 2017*, 142(Table 1):42–47, 2016.

[108] Masaya Nagai, Eiichi Matsubara, Masaaki Ashida, Jun Takayanagi, and Hideyuki Ohtake. THz time-domain spectroscopy beyond 4 THz using a sub-picosecond Yb-doped fiber laser system. *Int. Conf. Infrared, Millimeter, Terahertz Waves, IRMMW-THz*, pages 8–9, 2014.

[109] Chen Jiang, Kun Zhao, Li J. Zhao, Wu J. Jin, Yu P. Yang, and Shao H. Chen. Probing disaggregation of crude oil in a magnetic field with terahertz time-domain spectroscopy. *Energy and Fuels*, 28(1):483–487, 2014.

[110] Christian Weickhmann, Rolf Jakoby, Evan Constable, and R. A. Lewis. Time-domain spectroscopy of novel nematic liquid crystals in the terahertz range. *Int. Conf. Infrared, Millimeter, Terahertz Waves, IRMMW-THz*, pages 1–2, 2013.

[111] J. Orenstein and J. S. Dodge. Terahertz time-domain spectroscopy of transient metallic and superconducting states. *Phys. Rev. B - Condens. Matter Mater. Phys.*, 92(13):1–7, 2015.

[112] Francesco D'Angelo, Zoltán Mics, Mischa Bonn, and Dmitry Turchinovich. Ultra-broadband THz time-domain spectroscopy of common polymers using THz air photonics. *Opt. Express*, 22(10):12475–12485, 2014.

[113] Withawat Withayachumnankul and Mira Naftaly. Fundamentals of measurement in terahertz time-domain spectroscopy. *J. Infrared, Millimeter, Terahertz Waves*, 35(8):610–637, 2014.

[114] VA Fedotov, M Rose, SL Prosvirnin, N Papasimakis, and NI Zheludev. Sharp trapped-mode resonances in planar metamaterials with a broken structural symmetry. *Physical review letters*, 99(14):147401, 2007.

[115] Ming Huang, Jingjing Yang, Jun Sun, Jihong Shi, and Jinhui Peng. Modelling and analysis of ?-shaped double negative material-assisted microwave sensor. *Journal of Infrared, Millimeter, and Terahertz Waves*, 30(11):1131–1138, 2009.

[116] Withawat Withayachumnankul, Hungyen Lin, Kazunori Serita, Charan M Shah, Sharath Sriram, Madhu Bhaskaran, Masayoshi Tonouchi, Christophe Fumeaux, and Derek Abbott. Sub-diffraction thin-film sensing with planar terahertz metamaterials. *Optics express*, 20(3):3345–3352, 2012.

[117] Nan Zheng, Mahdi Aghadjani, Kyungjun Song, and Pinaki Mazumder. Metamaterial sensor platforms for terahertz dna sensing. In *Nanotechnology (IEEE-NANO), 2013 13th IEEE Conference on*, pages 315–320. IEEE, 2013.

[118] Tao Chen, Suyan Li, and Hui Sun. Metamaterials application in sensing. *Sensors*, 12(3):2742–2765, 2012.

[119] John F O?Hara, Withawat Withayachumnankul, and Ibraheem Al-Naib. A review on thin-film sensing with terahertz waves. *Journal of Infrared, Millimeter, and Terahertz Waves*, 33(3):245–291, 2012.

[120] Jonathan P Marangos. Electromagnetically induced transparency. *Journal of Modern Optics*, 45(3):471–503, 1998.

[121] Philippe Tassin, Lei Zhang, Th Koschny, EN Economou, and Costas M Souk-oulis. Low-loss metamaterials based on classical electromagnetically induced transparency. *Physical Review Letters*, 102(5):053901, 2009.

[122] Yadong Xu, Sucheng Li, Bo Hou, and Huanyang Chen. Fano resonances from gradient-index metamaterials. *Scientific reports*, 6, 2016.

[123] Song-Kum Song and Song-Jin Im. Mechanism of the fano resonance in a planar metamaterials: Analysis from the coupled two-oscillator model. *arXiv preprint arXiv:1605.00783*, 2016.

[124] Boris Luk'yanchuk, Nikolay I Zheludev, Stefan A Maier, Naomi J Halas, Peter Nordlander, Harald Giessen, and Chong Tow Chong. The fano resonance in plasmonic nanostructures and metamaterials. *Nature materials*, 9(9):707, 2010.

[125] Ranjan Singh, Ibraheem AI Al-Naib, Yuping Yang, Dibakar Roy Chowdhury, Wei Cao, Carsten Rockstuhl, Tsuneyuki Ozaki, Roberto Morandotti, and Weili Zhang. Observing metamaterial induced transparency in individual fano resonators with broken symmetry. *Applied Physics Letters*, 99(20):201107, 2011.

[126] Ranjan Singh, Ibraheem AI Al-Naib, Martin Koch, and Weili Zhang. Sharp fano resonances in thz metamaterials. *Optics express*, 19(7):6312–6319, 2011.

[127] SL Prosvirnin, VA Fedotov, S Zouhdi, and NI Zheludev. Trapped-mode reso-nances in isotropic planar metamaterials. *Advanced Research Workshop: Meta-materials for Secure Information and Communication Technologies*, 2008.

[128] Na Liu, Thomas Weiss, Martin Mesch, Lutz Langguth, Ulrike Eigenthaler, Michael Hirscher, Carsten Sonnichsen, and Harald Giessen. Planar metamate-rial analogue of electromagnetically induced transparency for plasmonic sensing. *Nano letters*, 10(4):1103–1107, 2009.

[129] N Papasimakis, YH Fu, VA Fedotov, SL Prosvirnin, DP Tsai, and NI Zheludev. Metamaterial with polarization and direction insensitive resonant transmission response mimicking electromagnetically induced transparency. *Applied Physics Letters*, 94(21):211902, 2009.

[130] Shaojie Ma, Shiyi Xiao, and Lei Zhou. Resonant modes in metal/insulator/metal metamaterials: An analytical study on near-field couplings. *Physical Review B*, 93(4):045305, 2016.

[131] Basudev Lahiri, Ali Z Khokhar, M Richard, Scott G McMeekin, and Nigel P Johnson. Asymmetric split ring resonators for optical sensing of organic mate-rials. *Optics express*, 17(2):1107–1115, 2009.

[132] Ibraheem Al-Naib, Yuping Yang, Marc M Dignam, Weili Zhang, and Ranjan Singh. Ultra-high q even eigenmode resonance in terahertz metamaterials. *Ap-plied Physics Letters*, 106(1):011102, 2015.

[133] Alexander B Khanikaev, Chihhui Wu, and Gennady Shvets. Fano-resonant metamaterials and their applications. *Nanophotonics*, 2(4):247–264, 2013.

[134] Ranjan Singh, Eric Plum, Weili Zhang, and Nikolay I Zheludev. Highly tunable optical activity in planar achiral terahertz metamaterials. *Optics express*, 18(13):13425–13430, 2010.

[135] Ranjan Singh, Evgenya Smirnova, Antoinette J Taylor, John F O?Hara, and Weili Zhang. Optically thin terahertz metamaterials. *Optics Express*, 16(9):6537–6543, 2008.

[136] Lin Chen, Chunmei Gao, Jiaming Xu, Xiaofei Zang, Bin Cai, and Yiming Zhu. Observation of electromagnetically induced transparency-like transmission in terahertz asymmetric waveguide-cavities systems. *Optics letters*, 38(9):1379–1381, 2013.

[137] Yuping Zhang, Tongtong Li, Beibei Zeng, Huiyun Zhang, Huanhuan Lv, Xiaoyan Huang, Weili Zhang, and Abul K Azad. A graphene based tunable terahertz sensor with double fano resonances. *Nanoscale*, 7(29):12682–12688, 2015.

[138] Ranjan Singh, Wei Cao, Ibraheem Al-Naib, Longqing Cong, Withawat Withayachumnankul, and Weili Zhang. Ultrasensitive terahertz sensing with high-q fano resonances in metasurfaces. *Applied Physics Letters*, 105(17):171101, 2014.

[139] Ben-Xin Wang, Xiang Zhai, Gui-Zhen Wang, Wei-Qing Huang, and Ling-Ling Wang. A novel dual-band terahertz metamaterial absorber for a sensor application. *Journal of Applied Physics*, 117(1):014504, 2015.

[140] Xin Hu, Gaiqi Xu, Long Wen, Huacun Wang, Yuncheng Zhao, Yaxin Zhang, David RS Cumming, and Qin Chen. Metamaterial absorber integrated microfluidic terahertz sensors. *Laser & Photonics Reviews*, 10(6):962–969, 2016.